Short-time Oxidation of Fe-Mn Alloys

Anjana Suresh

Materials Science and Engineering (MSE)

TU Delft

Short_Time Oxidation of Fe-Mn Alloys

Master's Thesis Report

by

Anjana Suresh

to obtain the degree of
Master of Science in Materials Science and Engineering
at the
Delft University of Technology,
to be defended publicly on July 21, 2021.

Student number:	4617940	
Project duration:	January 3, 2021 – July 21, 2021	
Thesis committee:	Dr. Amarante Böttger,	TU Delft, Supervisor
	Ir. Soroush Aghaeian,	TU Delft , Daily Supervisor
	Dr. Yaiza Gonzalez-Garcia,	TU Delft

This thesis is confidential and cannot be made public until July 21, 2023.

TU Delft

Acknowledgements

Working on my Master's thesis has been in equal parts challenging and exciting, with the highs and lows emphasised by the pandemic that has gripped the world for the better part of the past 1.5 years. I would not have made it through without the support of all the people mentioned in this section.

Firstly, I would like to thank my supervisor Dr. Amarante Böttger for the opportunity to work on this topic, for her expert guidance and for advice on overcoming obstacles in my research. I also want to thank my daily supervisor Soroush Aghaeian for his valuable insights and guidance, and for being supportive and encouraging during these challenging times. Thanks also to Hans Brouwer and Ruud Hendrikx for their assistance with the experiments as well as for taking the time to clarify all my doubts. Thanks to Sander Van Asperen and Katja Jarc for providing me with the required training. I also want to thank Dr.Yaiza Gonzalez-Garcia for being part of my thesis committee and Dr. Jilt Sietsma for his support as a mentor in my mentor group.

Secondly, I would like to thank my parents and my brother, without whose constant support and unconditional love none of this would have been possible. Even though they had their own set of challenges back home in India, their encouragement was unwavering.

Thirdly, I want to thank my dear friends who were my family away from family. My heartfelt thanks to Ashwathi and Radesh who welcomed me into their home and their lives with open hearts. Thanks to Revathy, Amrita and Sanika who were never far away despite being thousands of kilometres away. Thanks to Vineet, Siddharth, Vignesh and Srinivasan as well as Kamalesh for helping me out at crucial moments. Also thanks to my former housemates Shreyas, Kavya, Satish and Enrico for helping me endure the several different lockdowns - it was not easy.

Finally, I want to thank the students of MSE and TU Delft over several years ranging from 2016-2020 for all the friendly conversations and group work, some of whom are Narasimhan, Tijin, Jonathan, Surya, Sarika and Lakshmi. I am also grateful to the members of my FoodSwap group who saved me in their own small way several times. Thanks to Nupur Lalvani and the members of Blue Circle Diabetes Foundation for showing me that living with Type 1 Diabetes is not an insurmountable challenge. A quiet thanks also to the members of the online communities on Reddit such as r/study, r/productivity, r/GradSchool among others, they have helped me more than they will ever know.

Anjana Suresh
Delft, July 2021

Abstract

The global production of steel in a year is in the range of several millions of tonnes due to its essential function in industries such as automotive, manufacturing, and construction among others. However, a major challenge faced by the steel industry in the development of new steel grades is the inability to predict surface behaviour, such as the concentration profiles of alloying elements like manganese. This is due to the inability to predict the oxidation behaviour during the processing of steel. In order to solve this challenge, experimental data regarding oxidation on a short timescale is required which is not yet well-addressed in literature. Some of this data required will be generated in this research project via the experimental investigation of the oxidation of Fe-Mn binary alloys at high temperature. In this project, the oxidation experiments are performed on Fe-Mn alloys having a manganese composition ranging from 0.5-7% Mn in temperatures ranging from 1000-1150 °C and oxygen partial pressures ranging from 0.1-0.3 atm. The oxidation behaviour is studied using thermogravimetric analysis and the oxide layer is then characterised using X-ray diffraction. The in-situ evolution of oxide structure is observed using high-temperature X-ray diffraction, and finally the rate determining mechanism for the oxidation of Fe-Mn alloys at high temperature is identified.

Contents

List of Figures

List of Tables

1

Background information

One of the challenges faced by the steel industry regarding the development of new steel grades is the prediction of the oxide phases formed during the through-process of steel, such as that of hot-rolling process. The inability to predict the surface behaviour such as the concentration profiles of the alloying elements like manganese, due to the oxide formation leads to costly industrial trials for testing these steels. Thus, it is useful to develop a generic growth model for oxide growth at high temperature, in order to better simulate the surface behaviour of the steels in pilot processing. However, in order to develop this model, there is a requirement for experimental data especially regarding oxidation for a short timescale, which is not well addressed in literature at the time of the start of this project. Therefore, this data will be generated via an experimental investigation of the external oxides formed on the binary alloys such as Fe-Mn (which is the specific case under investigation) under high temperature on a short timescale. Thus, the following sections will provide an in-depth study of the knowledge requirement before undertaking the project.

1.1. Basic Concepts of High Temperature Oxidation

Steel is produced all over the world in large quantities (in the range of several millions of tons) annually due to its essential functions in the automotive, manufacturing, and other industries [47]. However, the processing and forming of steels into required shapes involves reheating, which further implies subjecting the material to high temperatures for longer overall processing times in oxidising atmospheres. This leads to the formation of oxide scales, which will then necessitate removal of these scales as well as lead to loss of material through oxide formation.

The spontaneity of a reaction i.e. the likelihood of oxide formation depends on the thermodynamics of the reaction. The second law of thermodynamics gives the equation [48]:

$$G' = H' - TS' \tag{1.1}$$

where G' = Gibb's free energy
H' = Enthalpy
S' = Entropy

For a chemical reaction given by:

$$aA + bB = cC + dD \tag{1.2}$$

The Gibb's free energy change (ΔG') can be given by:

$$\Delta G' = \Delta G^{\circ} + RTln\frac{a_C^c a_D^d}{a_A^a a_B^b} \tag{1.3}$$

where a_i = the thermodynamic activity of the species i.

The activities can also be expressed in terms of partial pressure as:

$$a_i = \frac{p_i}{p_i^\circ} \tag{1.4}$$

For a reaction given by $xM + \frac{y}{2}O_2 \rightarrow M_xO_y$, **dissociation pressure of the oxide** can be given by [5]:

$$p_{O_2}^{M/M_xO_y} = \exp\frac{\Delta G^\circ}{RT} \tag{1.5}$$

The values of $p_{O_2}^{M/M_xO_y}$ for different metal oxides can be obtained from the **Ellingham diagram** (such as the one shown in Figure 1.2), which is a plot of the ΔG° with respect to the temperature but has an attached nomograph for obtaining the oxygen partial pressures. In the case of metal oxidation, the activities of the metal and the specific oxide formed needs to be considered:

$$p_{O_2}^{eq} = \frac{a_{M_xO_y}}{a_M}\exp\frac{\Delta G^\circ}{RT} = \frac{a_{M_xO_y}}{a_M}p_{O_2}^{M/M_xO_y} \tag{1.6}$$

For any particular steel or alloy of Fe, the oxidation behaviour depends on the composition of the material, the temperature of the material and the oxygen partial pressure of the atmosphere. The following are the important steps in the oxidation process [47]:

1. Transport of oxygen to the scale-gas interface via mass transfer in the gas phase.
2. Incorporation of oxygen into the oxide scale (i.e. the interfacial reduction reaction, e.g.: $\frac{1}{2}O_2 + 2e \rightarrow O^{-2}$)
3. Diffusion of reacting metal ions from the inner alloy to the alloy-scale interface.
4. Incorporation of metal into the oxide scale (i.e. the interfacial oxidation reaction, e.g.: $M \rightarrow M^{2+} + 2e$)
5. Transport of metal and/or oxygen through the scale.

The evaluation of oxidation kinetics is done by understanding the **kinetic rate law** that governs the growth of the oxide layer and is followed during oxidation. The rate law followed is usually experimentally determined with the use of experimental techniques such as Thermogravimetric Analysis (TGA) [6] and the assumptions from theories such as Wagner's theory (see below) can usually be used to deduce the mechanisms of oxidation. However, depending on the conditions of oxidation, the growth of the oxide layer can follow different models as given below [17]:

- **Linear Oxidation Reaction** occurs when the rate limiting mechanism for the oxidation of the metal is controlled by the processes occurring at the phase boundary - such as the surface reactions or the gas transport of O_2 to the phase boundary. These processes usually control the rate of reaction in the beginning of the oxidation when the metal surface is not yet covered by a layer of oxide. However, it can also occur when the oxide formed is volatile (thus leaving the metal surface unprotected), when the oxide layer has spalled off or if the oxide formed is relatively porous. The equation is thus:

  $$X = k_l t \tag{1.7}$$

  where X = thickness (mass) of the oxide formed
  t = time of oxidation
  k_l = linear rate constant

  If the linear regime of oxidation continues during an oxidation experiment, there is a high chance of loss of the sample material, as the oxidation does not slow down.

- **Logarithmic and inverse logarithmic rates** generally describe low temperature oxidation for the formation of a thin film of oxide (in the scale of nanometres). The transport processes through the film are the rate controlling mechanism and the electric field across the thin film is the driving force for this kind of oxidation kinetics. The logarithmic equation is:

  $$X = k_e log(at + 1) \tag{1.8}$$

where k_e and a are constants and the inverse logarithmic rate is given by:

$$\frac{1}{X} = b - k_i log t \tag{1.9}$$

where k_i and b are constants.

- **Parabolic kinetics** is observed when the rate-controlling step for the oxidation reaction is the diffusion of the ions through the layer of oxide formed on the metal surface, and the driving force is the chemical potential gradient across this oxide layer. The rate of oxidation is a function of the thickness and slows down as the thickness increases. The equation for parabolic kinetics is given by:

$$X^2 = k't \tag{1.10}$$

where X = thickness of oxide layer
t = time of oxidation
k' = parabolic rate constant

- **Cubic rate equation** is sometimes observed when the oxidation times are extended i.e. t > 10000 hrs, and when a combination of different oxidation mechanisms are involved. It is given by:

$$X^3 = k_c t \tag{1.11}$$

The relationship between the rate of mass gain and the time of oxidation is graphically shown in Figure 1.1.

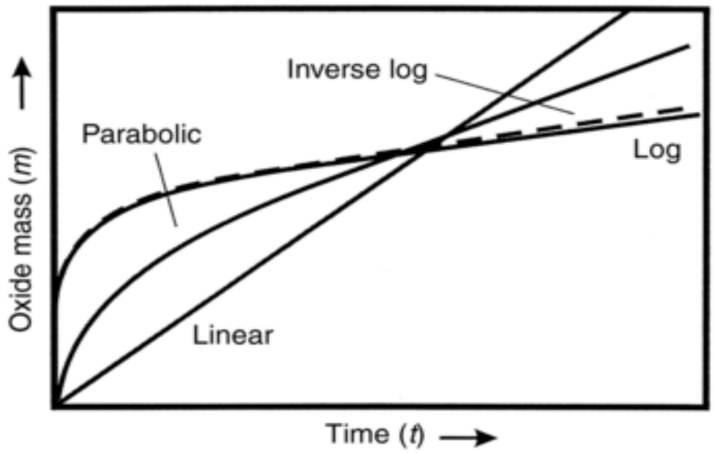

Figure 1.1: Different kinds of oxidation kinetics. [17]

When the diffusion of ions through the oxide layer is the rate-controlling mechanism of the high temperature oxidation of metals, the mechanism can be described by the model given by **Wagner's theory of oxidation**. Wagner's theory of oxidation states the following assumptions [7]:

1. The oxide layer is a compact, perfectly adherent scale.
2. Migration of ions or electrons across the scale is the rate-controlling process.
3. Local thermodynamic equilibrium is established at both the metal–scale and scale–gas interfaces.
4. The oxide scale shows only small deviations from stoichiometry and, hence, the ionic fluxes are independent of position within the scale.
5. Thermodynamic equilibrium is established locally throughout the scale.
6. The scale is thick compared with the distances over which space charge effects (electrical double layer) occur.

7. Oxygen solubility in the metal may be neglected.

Wagner's theory describes the parabolic rate of oxidation as given by the expression in Equation (1.10).

On using the assumptions of the Wagner's theory and deriving the expression for the theoretical calculation of the rate constant from the Fick's law of diffusion (for the case where the metal cations are more mobile) [5], the equation for the rate constant arrived at is:

$$k' = \frac{1}{RT}\int_{\mu''_M}^{\mu'_M} D_M d\mu_M \; cm^2 \; s^{-1} \tag{1.12}$$

where D_M = the diffusion coefficient of the metal cations through the oxide scale
μ_M = chemical potential of the metal cation
μ'_M = chemical potential of the metal at the metal-oxide interface
μ''_M = chemical potential of the metal at the oxide-gas interface

It is often difficult to predict the rate constant theoretically with a high degree of accuracy, as the values of the diffusion constants as a function of chemical potential are needed for this calculation and they are not always available in literature [5].

Depending on the reactivity of the constituent metals of an alloy, the oxidation of the alloy can occur internally or externally. Consider the example of an alloy A-B, as explained in [28], where A is the less reactive metal and B is the more reactive metal i.e. B requires lower O_2 partial pressure for oxidation. If oxygen diffuses through the metal A lattice to form B-oxide, then **internal oxidation** occurs. If on the other hand, B atoms diffuse to the alloy surface to form oxide, then the occurrence is known as **external oxidation**. The activity of oxygen at the metal-oxide interface is controlled by the local equilibrium between the oxide and metal. The maximum solubility of oxygen in the binary A-B alloy is then determined by the equilibrium between alloy and less stable oxide at metal-oxide interface.

Often a **transition from internal to external oxide** layer formation can occur during the oxidation process when a critical volume fraction of internal oxide f_v^* is attained, under which the penetration of oxygen ions is so restricted that it leads to the formation of external B-oxide [21]. Here, $f_v^* = f^*\rho$, where f^* is the critical mole fraction of oxide and ρ is the is the ratio between the molar volume of B-oxide and that of the alloy. The authors in [21] have assumed parabolic kinetics of the form $\xi^2 = 4\gamma^2 D_O t$ where ξ is the position of the internal oxidation front from the alloy-gas interface, γ is a dimensionless parameter related to the parabolic rate constant for internal oxidation and D_O the diffusion coefficient for oxygen in the alloy). On further equating the fluxes of oxygen and B (from Fick's Law) at the internal oxidation front for the formation of B-oxide (BO_ν), the following general equation has been arrived at:

$$\frac{N_O^S}{\nu N_B^0} = \frac{G(\gamma)}{F(\gamma\varphi^{\frac{1}{2}})} \tag{1.13}$$

where N_O^S = mole fraction of O dissolved in the alloy in equilibrium with the partial pressure of oxygen prevailing in the gas
N_B^0 = mole fraction of B in the bulk alloy
$F(r) = \pi^{\frac{1}{2}} r exp(r^2) erfc(r)$
$G(r) = \pi^{\frac{1}{2}} r exp(r^2) erf(r)$
$\varphi = D_O/D_B$
D_B = Diffusion coefficient of B in alloy

The equation (1.13) is further simplified to obtain the equation for the critical value of the mole fraction of B in the alloy (N_B^{0*}) required for the transition from internal to external oxide, and is given by:

$$N_B^{0*} = \frac{1}{\rho} f_v^* F(\gamma\varphi^{\frac{1}{2}}) \tag{1.14}$$

The above equation has been derived for the case of internal oxidation of B in the absence of the formation of AO oxide, but the equation is also applicable for the case of internal oxidation of B in the presence of existing external oxide. There will however be a change in the concentration profiles of the

oxygen and the B ions as the rate constant of the external scale formation has also been considered in the derivation of the general law for the same:

$$\frac{N_O^S}{\nu N_B^0} = \frac{erf(\gamma) - erf(u)}{erf(\gamma)} \frac{G(\gamma)}{F(\gamma\varphi^{\frac{1}{2}})} \tag{1.15}$$

where u = $[K_c/(2D_O)]^{\frac{1}{2}}$
K_C = Parabolic rate constant for external scale

The authors in [21] have concluded that the formation of an outer scale reduces the degree of enrichment, and therefore the concentration profile, of the less noble component in the internally oxidized region in comparison with the case when no outer oxide exists. It is also concluded that in the presence of an external oxide, the attainment of the critical volume fraction required for the internal oxide to transition to external oxide is more difficult. As a result, the critical concentration for the internal oxide to transition becomes higher, and increases with increase in the value of the parabolic constant for external oxidation.

1.2. Oxidation Condition

This project deals with an oxidation process that occurs during the finishing processes of steel such as the hot-rolling process in steel manufacture. The hot-rolling process involves reduction of the thickness of a material through the application of compressive forces, and is usually done at the end of a process flow as part of the finishing processes a material undergoes [19]. Hot rolling is a controlled rolling process of thermomechanical processing that involves heating a metal above its recrystallization temperature so that it becomes malleable or formable, and after forming process it is allowed to cool to room temperature. The oxidation process thus occurs at the high temperatures of above 950 °C and in air, conditions which promote the formation of an oxide scale [33]. Thus, an oxidation condition comprising a temperature range of around 950-1200 °C and p_{O_2} in the range of 0.1-0.3 atm is of interest in this project. An oxidising atmosphere for high temperature oxidation is considered to be an atmosphere at which the oxygen partial pressure is above the minimum required for the set temperature (e.g. 1000 °C) for the formation of a specific oxide. This can be calculated thermodynamically or can be approximated from the Ellingham diagram in fig. 1.2.

Further on via thermodynamics, i.e. by calculating the free energy of oxide formation for Fe at different temperatures and by extension the p_{O_2}, it is proven that at the temperatures at which the thermomechanical processing of steel is performed, scale formation is favoured [47]. Since steel can be considered to majorly consist of Fe, one of the oxidation reactions that can occur is the formation of wüstite (FeO):

$$Fe + \frac{1}{2}O_2 = FeO, \qquad \Delta G^\circ = -259600 + 62.55T\frac{J}{mole} \tag{1.16}$$

As can be observed from the Ellingham diagram in fig. 1.2, the partial pressure required for the formation of FeO is in the range of $\approx 10^{-14}$ atm at 1000 °C, which is far below the partial pressure of O_2 generally present in the atmosphere. This is also true for the formation of all the iron oxides (described in section 1.3.1) in the temperature range of 700-1250 °C [49]. As a result it is necessary to study the kinetics of oxidation and the rate of oxidation experimentally in order to evaluate the loss of material due to the scaling process.

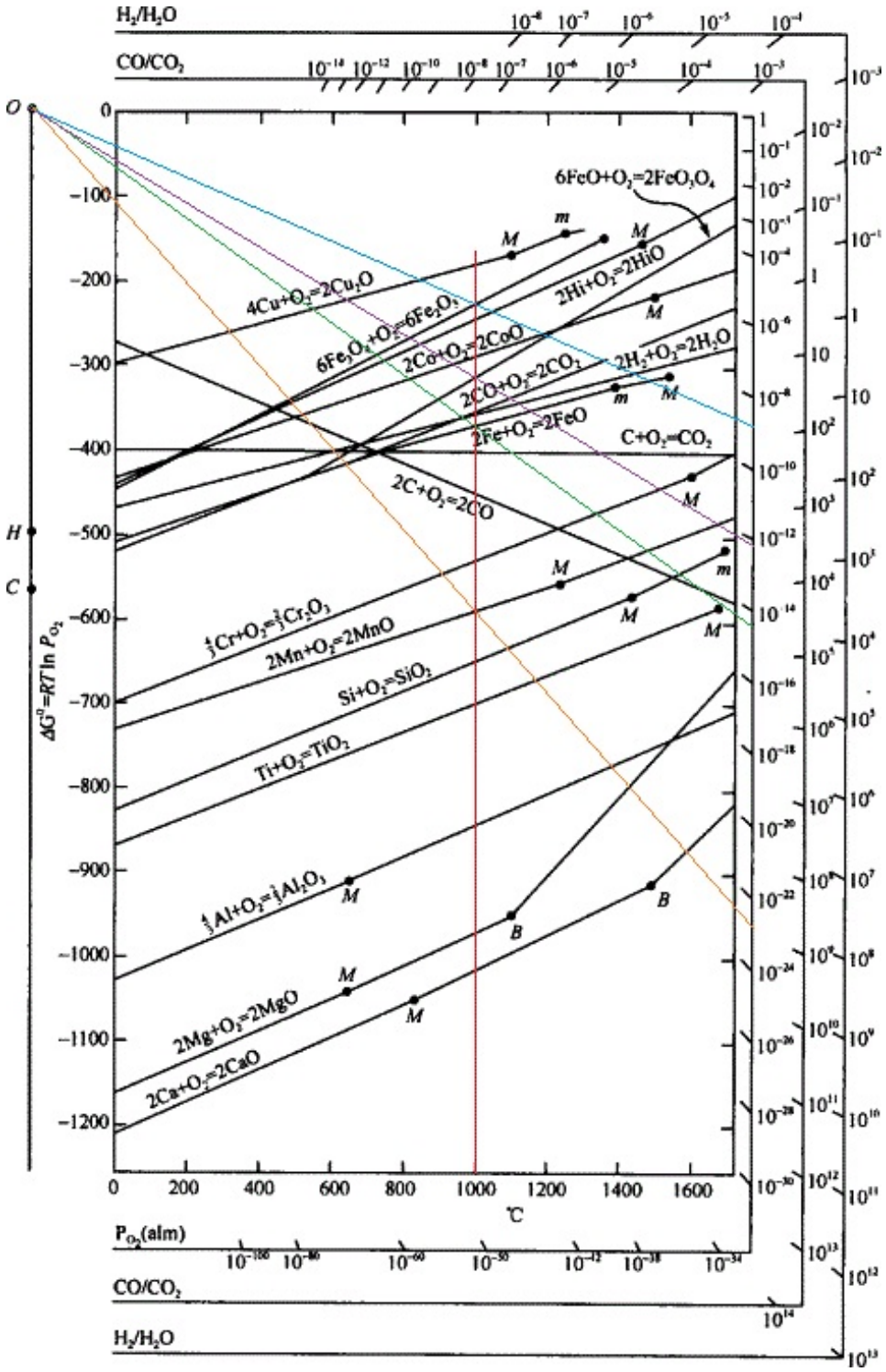

Figure 1.2: Ellingham diagram showing the oxygen partial pressures required for the formation of different oxides at 1000 °C [5]

1.3. High Temperature Oxidation of Fe and Fe-Mn Alloy

1.3.1. Pure Fe

There are primarily three types of oxides that can be formed by pure Fe – wüstite (FeO), magnetite (Fe_3O_4) and hematite (Fe_2O_3). The potential oxides to be formed can be predicted from the Fe-O phase diagram 1.3.

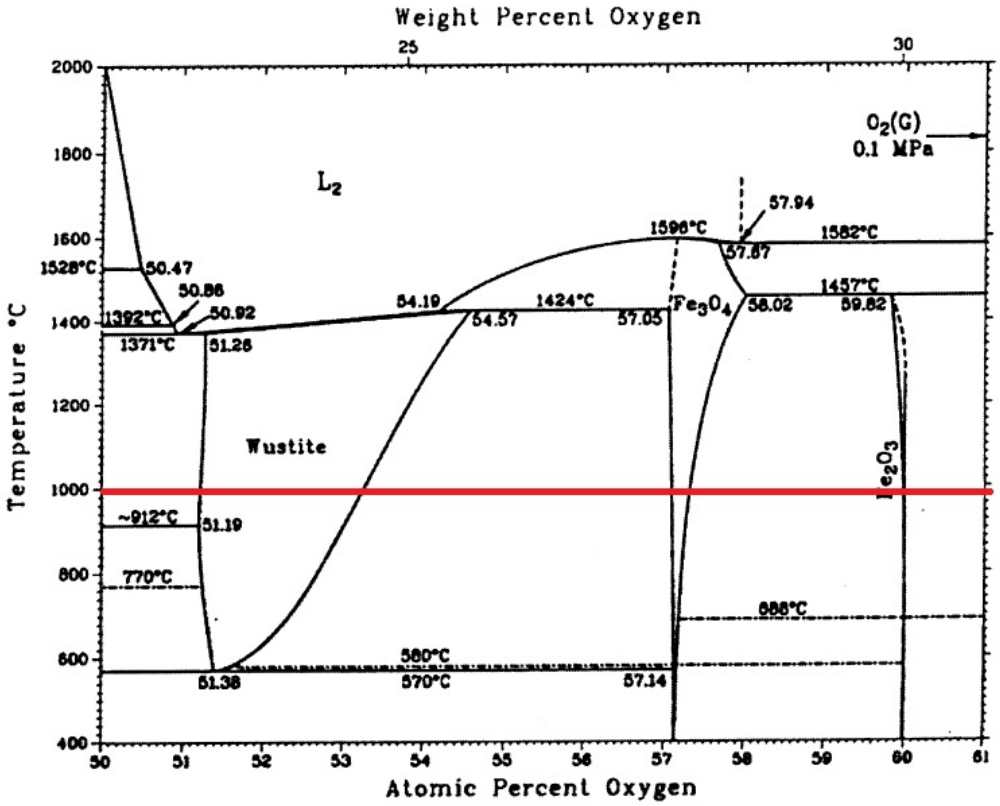

Figure 1.3: Fe-O phase diagram with a line indicating phases formed at 1000 °C [49]

The possible reactions of iron to form FeO, Fe_3O_4, and Fe_2O_3 are as follows:

$$Fe + \frac{1}{2}O_2 = FeO, \qquad \Delta G^\circ = -259,600 + 62.55T\frac{J}{mole} \tag{1.17}$$

$$3FeO + \frac{1}{2}O_2 = Fe_3O_4, \qquad \Delta G^\circ = -312,260 + 125.1T\frac{J}{mole}^1 \tag{1.18}$$

$$\frac{2}{3}Fe_3O_4 + \frac{1}{6}O_2 = Fe_2O_3, \qquad \Delta G^\circ = -83,147 + 45.5T\frac{J}{mole} \tag{1.19}$$

Depending on the conditions of temperature, atmospheric composition and total duration of the oxidation, different rates of oxidation have been found to be applicable for the high temperature oxidation of pure iron. In [46], Wagner and Pettit have described the oxidation of iron in the temperature range of 700-1100 °C in an atmosphere of $CO-CO_2$ gas mixture under total pressure varying between 0.4-1 atm, and have found that not only was a linear rate law followed for the oxidation kinetics, but that the mass gain curve showed two different linear regimes. The initial linear regime was observed when the oxide thickness was between 4×10^{-4} cm and 1.8×10^{-3} cm while the second linear regime was observed between 3×10^{-3} to 1×10^{-2} cm. Thus, it was experimentally observed that the linear law was followed until a certain critical thickness of oxide layer was achieved, here observed to be 10^{-2} cm, after which the oxidation kinetics followed the parabolic rate law. This is related to the change in the mechanism

[1] There was a typo regarding this equation in the original paper referenced i.e. [49], the corrected version (Fe_3O has been corrected to Fe_3O_4) as the authors intended has been given here.

of the oxidation as the thickness of the oxide layer increases – initially the rate determining step for the oxidation is the dissociation of CO_2 to CO and O at the surface of the metal after adsorption reactions at the phase boundary. It has been stated that the equation for the linear rate has been previously derived (in terms of grams of oxygen gained via mass gain of the sample) and is as follows:

$$\frac{\Delta \dot{m}}{A} = 16k'P'(1+k)[N'_{CO_2} - N'_{CO_2}(equil).] \tag{1.20}$$

where $\frac{\Delta \dot{m}}{A}$ = the experimental linear rate constant ($\frac{gm\ of\ O_2}{cm^2.s}$)
k' = rate constant of the phase boundary reaction ($\frac{moles}{cm^2.s.atm}$)
P' = sum of the partial pressures of CO and CO_2
K = the equilibrium constant for iron, wüstite and the gas mixture
N'_{CO_2} = mole fraction of CO_2 in $CO - CO_2$ mixture
$N'_{CO_2}(equil).$ = mole fraction of CO_2 in $CO - CO_2$ mixture in equilibrium with iron and wustite

The experimental results in [46] verify that equation (1.20) is followed for the range of temperatures and pressures specified. Further, it was found that the value of the rate constant in the initial linear regime was related to the grain size of the iron sample being tested. It has been postulated that in the initial linear regime, the dissociation of CO_2 and thus the reaction rate is influenced by the oxide layer that has been formed epitaxially on the metal surface while in the second linear regime, the rate is affected by the differently oriented oxide layer that now has a growth texture.

The influence of grain size on the oxidation kinetics of pure iron has been indicated in [43], wherein it is observed that the oxidation rate reduces with decrease in grain size. This is related to the movement of the metal ions i.e. metal diffusion along the grain boundaries in the oxide creates an inward flux of vacancies toward the metal/oxide interface. Here, vacancies could condense and form cavities in the metal below the grain boundaries. A cavity would lower the oxidation rate locally thus allowing the oxide at the grain boundary to dissociate, and cause the formation of a pore.

The results regarding the linear rate of oxidation being divided into two regimes and the influence of grain size and orientation on the kinetics of iron oxidation has also been mentioned in [10]. In annealed iron at temperatures of 1000 °C or more and in an atmosphere of $CO - CO_2$ gas mixture, it has been observed that the linear reaction rate and the two regimes can be distinguished when the total pressure is 0.1 atm or less. At conditions of lower oxidation rates (i.e. low partial pressure of CO_2 or low total pressures or low temperature) the changes in oxidation rate is less and so the linear rate is approached. The variation in morphology of the oxide layer during this transition (mostly consisting of wüstite) is also described, wherein the initial film grows epitaxially on the annealed iron and the resulting grains being similar to the underlying surface and as the oxidation progresses after the film-growth regime, faceted grains grow on the plate-like wüstite substrate.

When the oxide layer reaches the critical thickness, the kinetics approach parabolic rate law as the rate determining mechanism would be the diffusion of the Fe ions through the oxide layer (as the diffusion rate is inversely proportional to the thickness of the oxide layer) [46]. In [10] it is mentioned that the outer wüstite layer formed during the parabolic regime of oxidation appears to have columnar grains, while an inner layer appears to have pores and a region with smaller wüstite grains. As the oxidation occurs in an atmosphere of $CO - CO_2$ there isn't any formation of higher oxides.

According to R.Y. Chen [49], even though the initial oxidation is expected to occur rapidly, the overall oxidation kinetics at isothermal conditions is expected to follow the parabolic rate law when the duration of oxidation is greater than 15-20 min. For pure iron, within the parabolic regime, a thick wüstite layer is expected as an inner oxide layer, with a middle layer of magnetite of medium thickness and a very thin outer layer of hematite when oxidation occurs in air in the temperature range of 700 – 1250 °C. This is because the diffusion coefficient of Fe in wüstite is much greater than in magnetite, and the diffusion of O^{2-} and Fe ions through hematite layer is very slow.

The oxidation can be monitored in terms of weight gain (for example in the case of parabolic oxidation) by the use of an equation of the form [49]:

$$W^2 = k_p t + W_0^2 \tag{1.21}$$

where W = denotes the weight gain per unit area
k_p or k' = parabolic rate constant, usually measured in $g^2 cm^{-4} sec^{-1}$
W_0 = initial scale weight at the start ($t = 0$) of the parabolic oxidation

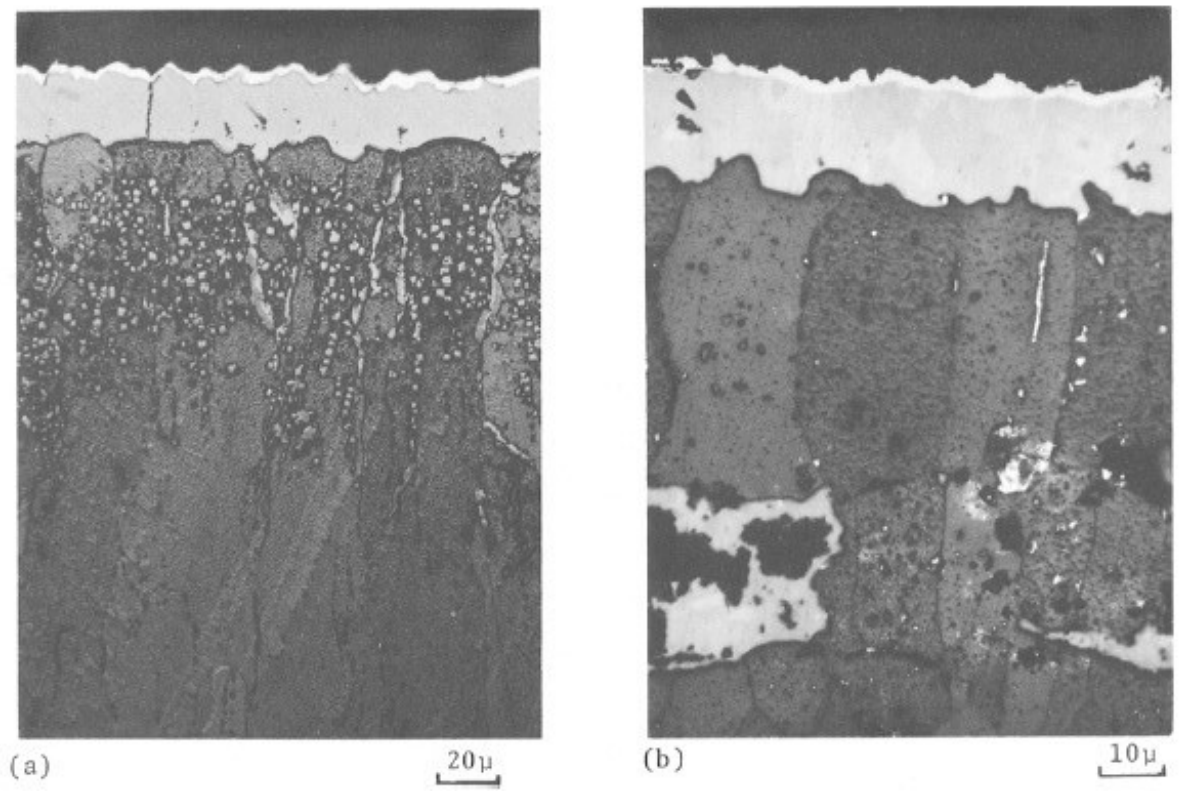

Figure 1.4: (a) Cross-section of scale formed on iron; (b) Cross-section of scale formed on manganese [27]

However, FeO is rarely present in its exact stoichiometric composition and can instead have a range of compositions ranging from $Fe_{0.954}O$ (corresponding to 48.81 at.% of iron) at 912°C at the wüstite iron interface, to $Fe_{0.836}O$ (45.53 at.% iron) at 1424°C at the wüstite–magnetite interface [49].

1.3.2. Fe-Mn Alloys

Manganese is well-known for its role in the strengthening of steels [3], however the high temperature oxidation of high manganese steels can cause a decrease in the surface concentration of manganese in steels and may result in a decrease in surface strength.

It is important to investigate the nature of the scales formed on the simpler binary Fe-Mn alloys in order to identify the scale components of more complex alloys. In the study by Jackson and Wallwork [27], the authors have studied the oxidation of the pure Fe and pure Mn in comparison with Fe-20%Mn and Fe-40%Mn binary alloys and indicated that the oxidation behaviour of Fe-Mn binary alloys optically and kinetically resembles that of the parent metals i.e. pure Fe and pure Mn. Scales formed on pure Fe and pure Mn at temperature of 800°C and 200 torr (≈ 0.26 atm) were three-layered and consisted of M_2O_3, M_3O_4, and MO (where M is the pure metal), with an increase in thickness toward the metal-oxide interface (see Figure 1.4 and Figure 1.5). The outermost layer of oxide in both of the Fe-Mn alloys were rich in manganese and appeared grey, while the inner layer that was thicker and appeared white was richer in Fe. The oxidation of both 20% and 40% Mn with Fe alloys was conducted at conditions of 200 torr oxygen atmosphere and at temperatures of 700°C and 800°C for 24-72 hrs. The different phases i.e. Fe_2O_3, Mn_2O_3, Mn_3O_4, $(Fe,Mn)_3O_4$ (cubic solid solution of Fe_3O_4 and Mn_3O_4), and $[(Fe,Mn)O]$ (solid solution of FeO and MnO), were identified with X-ray Diffractometry.

The authors [27] found that the thickness of the oxide layers varied with the alloy compositions and the conditions at which the metals were oxidised. Also the lower the manganese content, the closer the oxide composition was to the pure Fe metal oxides. In the case of Fe-20%Mn, the scale was predominantly composed of oxides of the form $[(FeMn)O]$, $[(FeMn)_3O_4]$, and Fe_2O_3 with separate layers of Mn_2O_3 and Mn_3O_4 formed above Fe_2O_3, but in smaller amounts. This implies that the formation of Fe_2O_3 occurred first, which means that Mn_2O_3 and Mn_3O_4 have higher dissociation pressures than

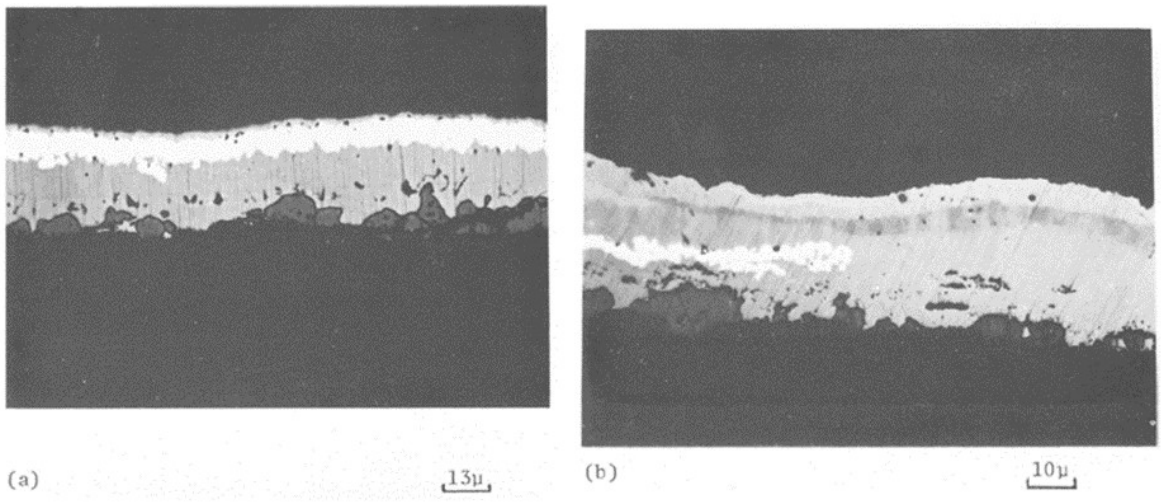

Figure 1.5: Metallographic cross-section of scale on (a) Fe-20%Mn and (b) Fe-40%Mn oxidised at 700°C for 70 hrs [27]

Fe_2O_3. On observing the Ellingham diagram (Fig. 1.2), this value will have to be several orders higher than that for MnO. However more importantly, this indicates the diffusion of Mn ions through the Fe oxide scale to form external oxides. Since it is stated that the composition of the oxide layer closest to the metal is $[(Fe, Mn)O]$ (similar to the wüstite formation in the oxidation of pure Fe) there is indication via the morphology of the scales alone, that the oxides formed are predominantly external. However, both the alloys showed a shallow layer of internal oxidation as well.

There is also an indication in [27] that the concentration gradient of Fe and Mn across the oxide layer is non-uniform because of the variation of oxide phases formed and the corresponding variation in diffusion coefficients of the metals in the different phases. The presence of surface layers of ferrite, due to enrichment of Mn in the oxide layer and subsequent phase transformation of austenite to ferrite (as explained in [4]), has also been indicated for the oxidation occurring at 700°C and 800°C.

Many of the conclusions arrived at by Jackson and Wallwork [27] have been confirmed by more recent works such as [31]. The authors in [31] have performed the high temperature oxidation of a steel having a composition of $Fe{-}31.8Mn{-}6.09Al{-}1.60Si{-}0.40C$, and this oxidation has been carried out under conditions of pure O_2 at 1 atm as well as synthetic air at 1 atm having an O_2 content of $20 \pm 0.5\%$ w/w. The temperatures were varied from 600-900°C and the oxidation was conducted for 2-38 hrs and the weight change was monitored using a thermobalance.

The kinetics were determined using a linear regression analysis using the data obtained from the oxidation experiments to fit to the following [31]:

$$(\frac{\Delta m}{s}) = \beta_1 t + \epsilon \quad (linear) \tag{1.22}$$

$$(\frac{\Delta m^2}{s}) = \beta_1 t + \epsilon \quad (parabolic) \tag{1.23}$$

$$(\frac{\Delta m^3}{s}) = \beta_1 t + \epsilon \quad (cubic) \tag{1.24}$$

$$(\frac{\Delta m}{s}) = \beta_1 log(t) + \epsilon \quad (logarithmic) \tag{1.25}$$

$$(\frac{s}{\Delta m}) = \beta_1 t + \epsilon \quad (logarithmic\ II) \tag{1.26}$$

where Δm = mass gain of sample
s = surface area of sample
t = time
β_1 = constant
ϵ = error term

The above models have been determined based on rate laws experimentally observed and already existing in literature [17].

Some of the important results with relation to the oxidation kinetics were that the thickness of the oxide layers increases with increase in temperature. The thickness of the layer oxidized at 600°C was in the range of 3 to 8 μm. The oxide layer after air and oxygen oxidation at 700 and 800°C, was 7 to 12 μm thick. In some areas of the alloy surface oxidized at 900°C, the oxide film had up to 15 μm thickness [31]. From the phases identified on the surface of the oxide scale, as given in Table 1.1, it is observed that there is significant enrichment of the iron oxide by manganese, as stated previously by [27]. It was concluded that in general, the studied alloy follows parabolic oxidation kinetics and the mechanism of oxidation is predominantly through diffusion implying that it is the rate-controlling process.

Table 1.1: Oxides identified by X-ray diffraction and the corresponding oxidation temperature and time after oxidation in air of an Fe–Mn–Al–Si–C alloy [31]

Oxide	Time (h)	Temperature (°C)
Mn_2O_3	22.5	600
$MnFe_2O_4, Mn_2O_3, (MnFe)_2O_3$	15	800
$MnFe_2O_4, Fe_3O_4, FeO, \gamma - Mn_2O_3, \gamma - Fe_2O_3, Mn_3O_4$	3	900
$MnFe_2O_4, FeO, Fe_2O_3, MnAl_2O_4, \gamma - Fe_2O_3$	45	1000
$MnFe_2O_4, Fe_3O_4, FeO$	2	1100

The effect of the varying composition of manganese in Fe-Mn binary alloys on its oxidation kinetics has been studied in [32]. The oxidation experiments were studied at a temperature of 1000°C for at least 4-5 hrs, under an atmosphere of different compositions of $CO - CO_2$, in order to ensure the formation of only [$(FeMn)O$] i.e. manganeseo-wüstite scale. The compositions of the Fe-Mn binary alloys studied varied from 1-59% Mn. On performing the oxidation experiments to study the dependence of the oxidation kinetics on the alloy composition as well as the composition of the oxidising atmosphere, it was found that the overall trend was similar to that of pure iron even at higher compositions of Mn. However, it was also found that the parabolic oxidation constants decreased with increasing alloy manganese contents and carbon monoxide partial pressures (see Figure 1.6).

Further it was found in [32] that the oxide formed on pure iron and the alloy containing 10 w/w % Mn exposed to pure carbon dioxide and a 100/10 $CO_2 - CO$ atmosphere also contained magnetite (Fe_3O_4) besides the expected [$FeMn(O)$]. All the other compositions exhibited only the presence of manganeseo-wüstite. The oxidation was noted to be mostly external with a small degree of internal oxidation; however even at 59 w/w% concentration of manganese, the penetration depth of the internal oxidation did not exceed 10% of the total scale thickness. The authors have also determined the Mn concentration profiles across the scale, determining the manganese depletion gradient to be linear and decreasing outward toward the scale, and the depletion layer extending no more than 50 μm inward from the alloy interface. The ratio of manganese to iron in the scale decreasing with distance from the alloy interface as been attributed to the mobility of iron in the scale being higher than that of manganese. This has been concluded by calculating the diffusivities of Fe and Mn using the data determined from the concentration profiles and deriving equations from the general equations by Wagner in [45].

In [29], the kinetics of the internal oxidation of Mn-steel alloys is described for oxidation at 950°C in a mixed atmosphere having a dew point of 10°C. The paper states that since the process is diffusion controlled, the kinetics followed by the sample oxidation is parabolic. The occurrence of phase transformation from γ to α iron is also observed and found to enhance the oxide precipitation.

1.4. Short-time Oxidation

The literature for short-time oxidation has been studied in this section, in order to gain a better understanding of the procedure involved.

Investigation of the short time oxidation kinetics has been discussed in [50] for the case of low carbon, low silicon steel a strip of thickness 0.75 mm was used for all the temperatures, but a strip of thickness 0.3 mm was also used for some oxidation experiments for the sake of comparison, and the compositions of the two are given in 1.2.

The basic procedure followed for the oxidation experiment involved heating the sample at a rate of 300 °C/ min in high purity nitrogen gas (99.99% N_2) flowing at a rate of 7 litre/ min to a target

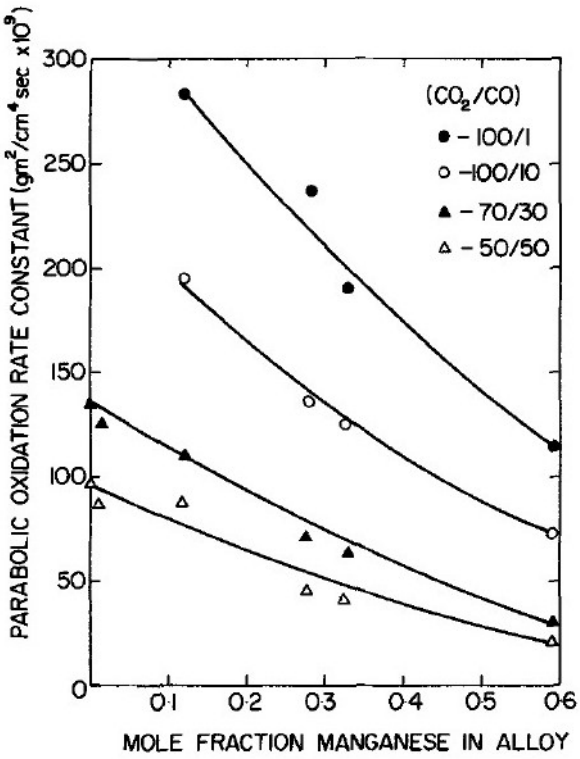

Figure 1.6: Parabolic oxidation constants for Fe-Mn alloys as a function of manganese content. [32]

Table 1.2: Steel Composition (in wt%) [50]

Element	C	Mn	Si	P	S	Cr	Ni	Cu	Al	N
0.75 mm thick strip	0.05	0.21	0.01	0.01	0.014	0.014	0.009	0.012	0.042	0.0032
0.3 mm thick strip	0.055	0.21	0.01	0.011	0.013	0.014	0.021	0.014	0.045	0.0031

temperature, holding it at the target temperature for about 2 min to allow the sample temperature to homogenize, and then the protective gas is switched to industry-purity air flowing at the same rate for a specified duration, mostly in the range of 6–30 or 6–60 sec, but for comparison purposes, the duration was extended to 1,800 sec at 850 °C . At the end of the oxidizing duration, the reaction gas was switched off and replaced with flowing high-purity nitrogen again. After holding the sample for 12 more seconds at the target temperature, the sample was initially cooled at 50 °C/ min to around 700 °C and then furnace-cooled to a temperature below 200 °C before it was withdrawn outside the furnace and cooled in ambient air to room temperature.

The weight gain data obtained was then used to find the kinetic rate constant by fitting the data using linear regression methods, and a summary of it is given in table 1.3 . Initially, the linear rate law is followed for very short timescales i.e. less than a minute, after which the parabolic rate law is followed. This is mostly in line with the previously discussed oxidation behaviour of iron having an overall parabolic rate of oxidation as also given by [49], possibly because the alloying elements are too low in percentage to greatly affect the overall oxidation behaviour of the samples.With the increase of oxidation temperature, the linear regime of oxidation is seen to increase in prominence, in terms of duration and rate, however due to blister formation and spallation of oxide layer, the exact duration of the linear regime and start of the parabolic regime was difficult to determine. In the case of the sample oxidised at 900 °C a linear rate is observed and is possibly in relation to the formation of blisters on the sample surface during the oxidation. The blisters reduce the surface area for iron diffusion from substrate to scale, giving a lower oxidation rate and linear kinetics.

Some important observations regarding the experiments in [50] is as follows:

- The weight gain as a function of the oxygen uptake was converted in terms of scale thickness and the general trend was observed that at least for the different durations examined, the scale

Table 1.3: Oxidation rate constants at the different target temperatures [50]

Target T °C	Short time steel oxidation rates Linear rate ($g\ cm^{-2}s^{-1}$)	Parabolic rate ($g^2cm^{-4}s^{-1}$)	Long term iron oxidation rates Parabolic rate ($g^2cm^{-4}s^{-1}$)
850 (18-60 sec)	-	1.37×10^{-7}	1.44×10^{-7}
900	3.98×10^{-5}	-	2.95×10^{-7}
1000 (0.75 mm)	-	9.14×10^{-7}	1.05×10^{-6}
1000 (0.3 mm)	-	8.28×10^{-7}	1.05×10^{-6}
1100 (0.75 mm)	$2.28 \times 10^{-4}(6 - 24\text{sec})$	$2.70 \times 10^{-6}(24 - 42\text{sec})$	3.10×10^{-6}
1100 (0.3 mm)	$2.21 \times 10^{-4}(6 - 30\text{sec})$	$2.22 \times 10^{-6}(24 - 42\text{sec})$	3.10×10^{-6}
1180 (0.75 mm)	$2.76 \times 10^{-4}(6 - 18\text{sec})$	-	-
1180 (0.3 mm)	$2.10 \times 10^{-4}(30 - 60\text{sec})$	-	-

thickness increased with the time of oxidation.

- Increase in the gas flow rate increases the overall scale thickness formed, however the percentage rate of oxygen consumption drops.
- The rate law followed had a dependency on the temperature of oxidation, and the morphology of the scales formed was also a direct effect of the kinetics followed. For example, the observation of a “rough” scale corresponded to linear kinetics, while parabolic kinetics were related to the formation of a smooth scale.
- At a certain critical thickness of the oxide layer for, for example in the case of the oxidation of both the samples at 1180 °C this thickness is in the range of 60-80 μm, a transition from linear kinetics to parabolic kinetics was observed.

1.5. Conclusions

After having studied the literature obtained so far, some conclusions that can be arrived at are:

- Fe-Mn binary alloys are more likely to follow an initial linear rate of oxidation for short time periods and then transition to parabolic oxidation kinetics after a critical thickness of oxide layer is achieved.
- It is possible for all oxides of iron (wüstite, magnetite and hematite) to exist at the oxidation condition of 950-1200°C and 0.1-0.3 atm p_{O_2}. It is likely for the oxide layer formed to primarily consist of wüstite.
- The oxide scale composition of Fe-Mn binary alloys is dependant on the composition of the metals in the alloys. Some amount of internal oxidation is expected (and is dependent on concentration of the more reactive metal in the alloy as well as the oxygen partial pressure) but the internal oxidation depth is much lesser than the thickness of the external oxide layer.

1.6. Research Objectives

1. Experimentally investigating the oxidation behavior of Fe-Mn binary alloy during short-time ($\sim$15 minutes) oxidation, where the techniques will involve Thermogravimetric Analysis (TGA) for studying the development of the oxide layer and its kinetics and X- ray Diffraction (XRD) for identifying the different phases of the oxides formed
2. How the control parameters affect the oxide formation, the parameters being the following:
   (a) Temperature of the isothermal oxidation process
   (b) The partial pressure of the different gases in the gas atmosphere during oxidation
   (c) The composition of the material
3. Determining the rate controlling oxidation mechanism

2

Oxidation Experiments

2.1. Objective

In order to determine the experimental rate constant during the oxidation of the different samples via observation of the oxidation kinetics, the oxidation experiments were performed using thermogravimetry analysis (TGA) technique.

2.2. Sample Preparation

The samples used for the experiments were small ingots of binary alloys of Fe-Mn with the composition of Mn ranging from $0.5 - 7\%$ (see Table: 2.1). The samples were cut by electric discharge machining (EDM) in order to be suitable for experimentation in the SETARAM TAG 24 machine. The dimensions of the samples were $15 \times 8 \times 2$ mm, with a hole at the top at about 2 mm from one of the short edges. A picture of one of the samples used is given in Figure: 2.1.

Figure 2.1: Fe-3%Mn ingot; unpolished

The samples were then progressively sanded with Emory papers ranging from grades P400 to P2500. The samples were washed with water before progressing to the next grade of paper.
After sanding, each sample was then ultrasonically cleaned in isopropyl alcohol for $1\,\mathrm{min}$. The samples were then dried with a stream of pure N_2 gas.
The samples were then polished with 3μ liquid and Mol cloth as well as 1μ liquid and Nap cloth. Ultrasonic cleaning with isopropanol was done between steps and after the final step. The samples were then dried with a stream of air.

Table 2.1: Chemical composition of the Fe-Mn binary alloys in weight percent

Alloy	C	Mn	Si	Al	Cr
Fe-0.5%Mn	0.002	0.506	0.002	0.0003	0.001
Fe-3%Mn	0.002	2.845	0.0014	0.0002	0.0002
Fe-7%Mn	-	7.057	0.011	-	0.03

In order to observe the grain size and microstructure, the samples were then etched using 2% Nital (a mixture of nitric acid and ethanol).The samples were then examined under different magnifications with a microscope (Figure: 2.2 and also in A.3.1).

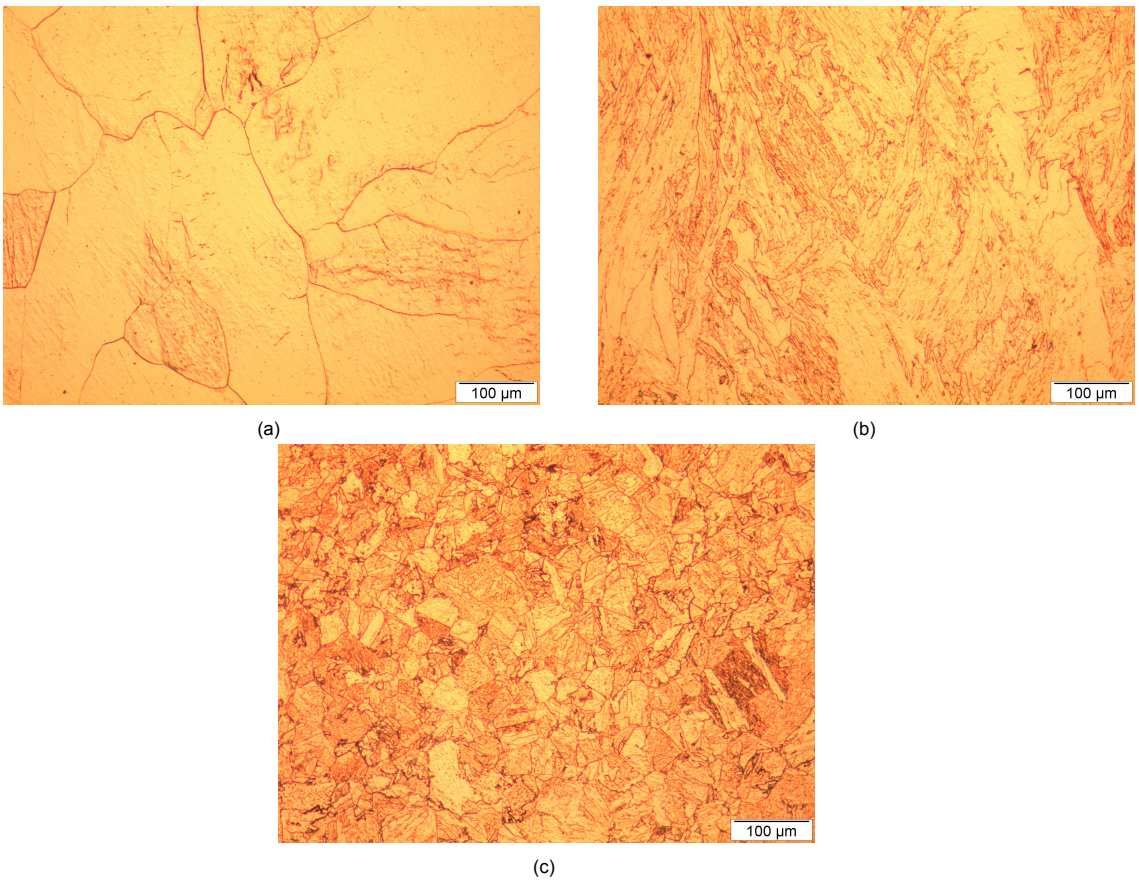

(a) (b)

(c)

Figure 2.2: Images showing the grains of (a) Fe-0.5%Mn, (b) Fe-3%Mn and (c) Fe-7%Mn

On observing the microscopy images in 2.2, the grain size seems to be progressively decreasing as the Mn content increases. As the grains seem irregularly shaped, the intercept procedure for determining grain size is used as opposed to the planimetric method that is usually applied to equiaxed grains [26]. The intercept method would involve counting the number of grain boundary intersections with a test line, per unit length of test line, and this number is used to calculate the mean lineal intercept length, $\bar{l}$ which can be approximated as the grain size. For the calculation, four lines were used to determine the mean lineal intercept using the ImageJ software. The approximate grain size is given in Table: 2.2 and the calculations are given in A.3.2.

2.3. Experimental Procedure

For the thermogravimetric analysis, TGA is used to record the change in temperature and the mass gain occurring during oxidation. Using this information, it is possible to measure the rate of oxidation and further find the rate constant of the oxidation. The oxidation is performed under isothermal conditions, wherein the mass change is recorded as function of time at constant temperature. The temperature

Table 2.2: Calculated approximate grain sizes

Alloy	Grain size (μm)
Fe-0.5%Mn	150
Fe-3%Mn	49
Fe-7%Mn	29

measurement is done via a thermocouple which has been placed under the sample.

The parameters to be controlled are the temperature at which the oxidation will be performed, the duration of the oxidation as well as the O_2 partial pressure during the oxidation.

- In the 'SETARAM TAG 24' machine, two furnaces are used during experimentation with the aim of compensating for the 'buoyancy effect', that can occur due to the flow of the different gases into the furnace chamber. The mass gain is detected via a microbalance and two crucible holders that are suspended on either side of the balance.

- An empty crucible is placed in each crucible holder. One crucible has a 'Reference' material made of alumina and having the same approximate weight as the sample to be measured. The experimental sample is placed in the crucible on the side that has a thermocouple. The sample is then weighed.

- A gas flow at normal pressure is necessary when taking thermal analysis measurements. The sweeping gas renews the atmosphere by carrying away the vapors emitted by the sample. An inert gas (helium, argon, nitrogen, etc.) is used to protect the sample from oxidation during heating process. Initially the furnace chamber is flushed with inert N_2 gas before heating the sample to a target temperature of, say, 1000 °C. Once the atmosphere is homogenised, the sample is heated to 1000 °C at a rate of 10 °C/ $\min$ and the target temperature is held for a few minutes for the ferrite to austenite transformation.

- The inert gas is then switched to an active gas mixture for the oxidation experiment. An active gas (oxygen, hydrogen, etc.) is a gas that reacts with the sample and the corresponding transformation can be studied. In the current case, the active gas used is oxygen.

- The flow rates are adjustable from 4 to 200 ml/min for the carrier gas and 0.3 to 16 ml/min for the auxiliary/active gas. Since the objective is to simulate atmospheric conditions i.e. a p_{O_2} of 0.2 atm, and the total gas flow rate is 53.3 ml/min, the flow rate required for O_2 would then be 10.6 ml/min and the N_2 flow rate would be 42.7 ml/min.

- The sample is then held in the oxidising atmosphere at the target temperature for a duration of 15-20 $\min$ and then the atmosphere is switched once again to inert gas.

- The sample is then cooled down to room temperature also at a rate of 10 °C/ $\min$ and then is removed from the furnace.

The mass gain and temperature change data during the experiment are recorded in Excel sheets and this data is then used for rate constant calculations.

2.4. Calculations

The possible rates of oxidation that are expected to be followed during the oxidation experiments, as deduced from the literature surveyed, are the linear rate of oxidation and the parabolic rate of oxidation. The experimental rate constants for the same can be calculated using the equations for the rate laws in terms of mass gain [50]:

$$W/A = k_l t + C \quad (linear) \tag{2.1}$$

$$[(W/A)]^2 = k_p t + C \quad (parabolic) \tag{2.2}$$

where W = the mass gain
A = the sample area
k_l = linear rate constant
k_p = parabolic rate constant

2.4.1. Experimental Linear Rate Constant

The data from the Excel sheets for all of the 11 experiments recorded were imported into MATLAB in order to obtain the data for analysis, and to plot the graphs of temperature change with respect to time as well as the mass gain with respect to time. The duration of linear rate of oxidation was considered as the as the time during which under a homogeneous atmosphere (i.e. the gas flow in the furnace chamber has reached steady state), the rate of mass gain has a linear slope and then the 'Basic Fitting' tool was used to fit the data to a linear fit and further obtain the value of the slope of the graphs i.e. the rate constants in MATLAB. The fitting was done only for the region specified because for a few seconds during the switching on and off of the gas supply, the flow rate is not steady and can affect the accurate estimation of the linear rate constant.

An example of the plotting done is given in the figure 2.3.The surface area of the samples (unpolished, not accounting for hole) is estimated to be $(A) = (15 \times 8 + 8 \times 2 + 15 \times 2) \times 2 = 332\ mm^2 = 3.32\ cm^2$.

The plots for the other experiments have been attached in the section A.1 of this report, and the linear rate constants and experimental parameters have been summarised in the table 2.3.

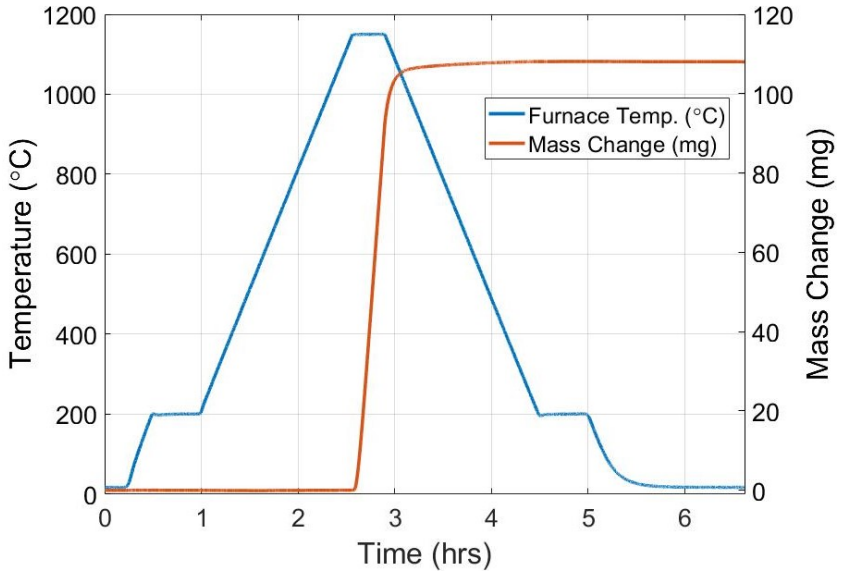

(a)

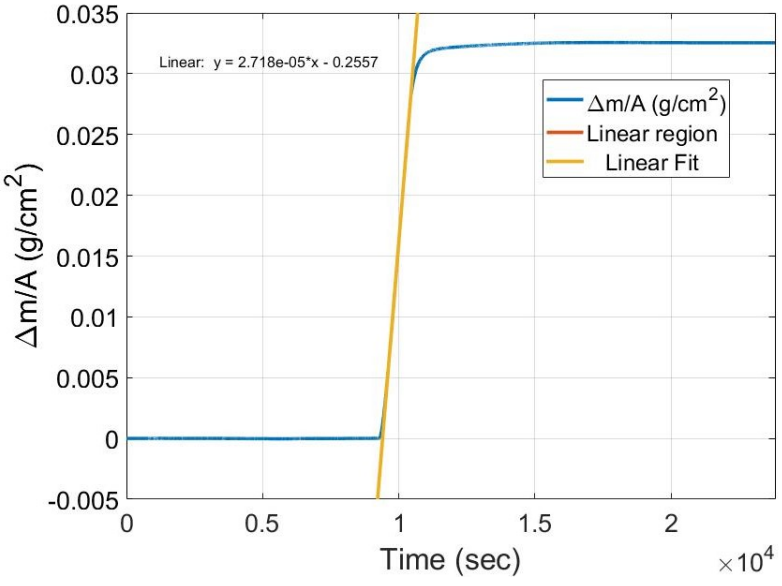

(b)

Figure 2.3: Results for Fe-7%Mn alloy oxidised for 20 min at 1150 °C in 20% O_2 (a) Mass gain and change in furnace temperature with respect to time and (b) Fitting of linear region of mass gain to obtain the slope

Table 2.3: Experimental rate constants for Fe-Mn alloys

S. No.	Oxidation Time t min.	Oxidation Temperature T °C	Oxygen Mole Fraction X_{O_2}	Experimental Rate Constant $k_{l_{exp.}}$ $(g/cm^2 sec)$
Fe-7%Mn				
1	15	1000	0.2	2.698×10^{-5}
2	15	1000	0.3	3.983×10^{-5}
3	15	1000	0.2	2.632×10^{-5}
4	15	1000	0.1	1.233×10^{-5}
5	20	1100	0.2	2.715×10^{-5}
6	20	1050	0.2	2.752×10^{-5}
7	20	1150	0.2	2.718×10^{-5}
Fe-3%Mn				
8	20	1000	0.2	2.714×10^{-5}
9	20	1100	0.2	2.724×10^{-5}
Fe-0.5%Mn				
10	20	1000	0.2	2.693×10^{-5}
11	20	1100	0.2	2.719×10^{-5}

2.5. Results

Upon examination of the obtained experimental rate constants, it can be observed that for the same O_2 partial pressure, the values are very close to each other. The temperature in the range of 1000-1150 °C and the composition in the range of 0.5-7%Mn does not seem to have as much of an effect on the value of the rate constant. In comparison to the results of [50] as given in the table 1.3, the values of the experimental rate constant obtained for the same temperature range seem to be 10 times lower, which could be because of the difference in the method of investigation employed (discontinuous weight measurement in the case of [50]). A reason as to why the linear rate of oxidation continues to last for greater than 15-20 min, when in [50] the linear region of oxidation lasts only for time intervals in the range of seconds or a couple of minutes at the most, might be related to a discussion found in [34] - where the authors discuss the short-circuit diffusion of Fe cations through the austenite grain boundaries leading to Fe cations being readily available for the reaction of oxygen ions at the oxide-gas interface for longer times. It is also likely that the critical thickness at which the oxygen ions start reacting with the wüstite has not yet been reached, resulting in a continuation of the linear regime of oxidation without transitioning into the parabolic regime.

3

X-Ray Diffraction

As per [27] and [49], Fe-Mn alloys with Mn% of ≤20% on being oxidised at high temperatures form an inner layer of wüstite scale, with a middle layer of magnetite and an outer layer of hematite, similar to the oxidation of pure Fe. Both [27] and [31] have verified the presence of Manganese in the oxides formed during the oxidation of Fe-Mn alloys with high Mn weight%, however it should also be noted that the Mn% examined in these two studies are 20-40% and ≈30% respectively, while this project considers binary alloys with the composition of Mn% that is smaller and in the range of 0.5-7%Mn. Some of the phases that are expected to be formed during the high temperature oxidation of Fe-Mn binary alloys are therefore Manganeseo-Wüstite ($Fe(Mn)O$), Hematite(Fe_2O_3) and Magnetite(Fe_3O_4), and this is also observed from the phase diagram in Fig. 3.1. Since $log_{10}\ p_{O_2} = -0.69$ at $p_{O_2} = 0.2\ atm$, there exists the possibility of formation of all the different phases of oxides as shown in the phase diagram fig. 3.1 (for the condition of 1000 °C temperature and 1 atm p_{O_2}).

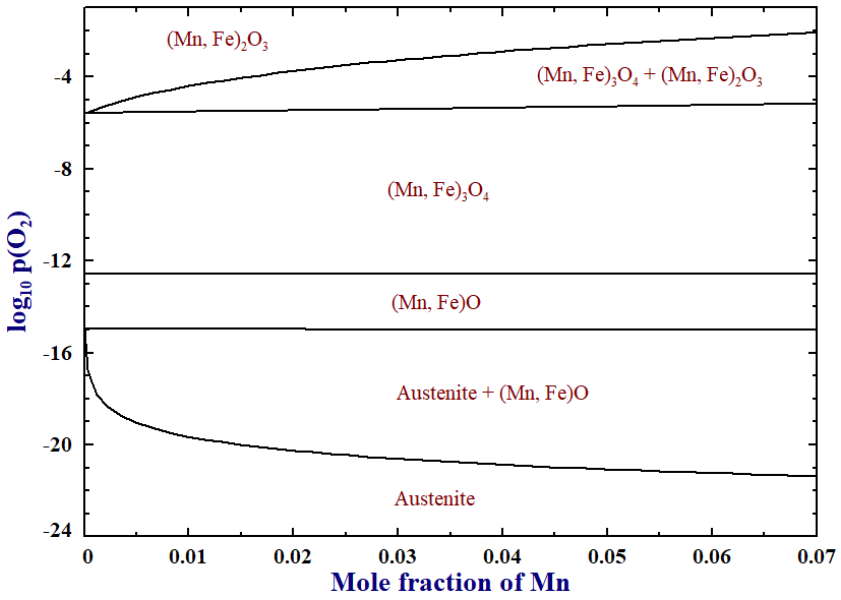

Figure 3.1: Fe-Mn phase diagram with respect to $log_{10}\ p_{O_2}$ [1]

3.1. Objective

In order to identify the different oxide phases formed during the short-time oxidation of Fe-Mn binary alloys, it is necessary to perform the characterisation of the oxides. Depending on the oxide phases identified, it is possible to confirm the rate law followed during the oxidation experiment and by extension the mechanism of the oxidation that determines the oxidation rate. After the completion of the oxidation

experiments, the Fe-Mn binary alloy samples were taken for characterisation using X-ray diffraction. The method used was the standard powder diffraction methodology, wherein monochromatic radiation of a fixed wavelength λ is used for phase identification on a fixed sample and the 2θ locations at which the highest peak intensities occur in the resultant diffraction spectrum is analysed.

The different phases of interest along with their characterising peaks (the three highest peaks and their respective 2θ) are given in Table 3.1.

Table 3.1: Powder Diffraction Data showing prominent peaks for the phases of interest. [42], [16]

Phase	2θ	d-spacing	Miller Indices		
	($^\circ$)	(nm)	h	k	l
Austenite	43.8	0.2065	1	1	1
$Fe-3\%Mn$	51.02	0.1788	2	0	0
(fcc)	75.04	0.1265	2	2	0
Wüstite	36.15	0.2483	1	1	1
FeO	41.99	0.215	2	0	0
(fcc)	60.89	0.1520	2	2	0
Hematite	33.12	0.2703	1	0	4
Fe_2O_3	35.61	0.2519	1	1	0
(hcp)	54.00	0.169	1	1	6
Magnetite	35.02	0.2560	3	1	1
Fe_3O_4	61.75	0.1501	4	4	0
(fcc)	56.25	0.1634	5	1	1

3.2. Experimental Specifications

For the XRD characterisation, the experimental conditions and specifications are as follows:

- *Sample*: The samples used for characterisation have a composition of Fe-7%Mn, and have the dimensions 15×8×2 mm as previously mentioned.
- *Instrument*: The instrument used was the Bruker D8 Advance diffractometer with Bragg-Brentano geometry and Lynxeye position sensitive detector, and Cu Kα radiation was used.
- *Measurements*: The measurements were done as a coupled θ-2θ scan in the range 20°-100°, step size 0.030°2θ and the counting time per step was 2 sec.

3.3. Results

The figure 3.2 shows the XRD pattern of the oxide formed on Fe-7%Mn alloy. The wüstite phase has been identified, however the presence of magnetite has also been observed. Thermodynamically, it is possible for all the oxides to be present at high temperatures in the given oxygen partial pressure conditions, but the formation of magnetite and hematite usually occurs only after the linear regime of oxidation has ended and the oxidation has then entered the parabolic region i.e. the major transport process is that the O^{2-} ions diffuse through the FeO (wüstite) layer to react with the oxide to form magnetite at the oxide/gas interface [18]. However magnetite can also be formed at lower temperatures in high oxygen environment due to instability of wüstite [11]. This hypothesis is tested by performing the high temperature XRD for in-situ oxidation of the metal alloys and phase-identification in chapter 4.

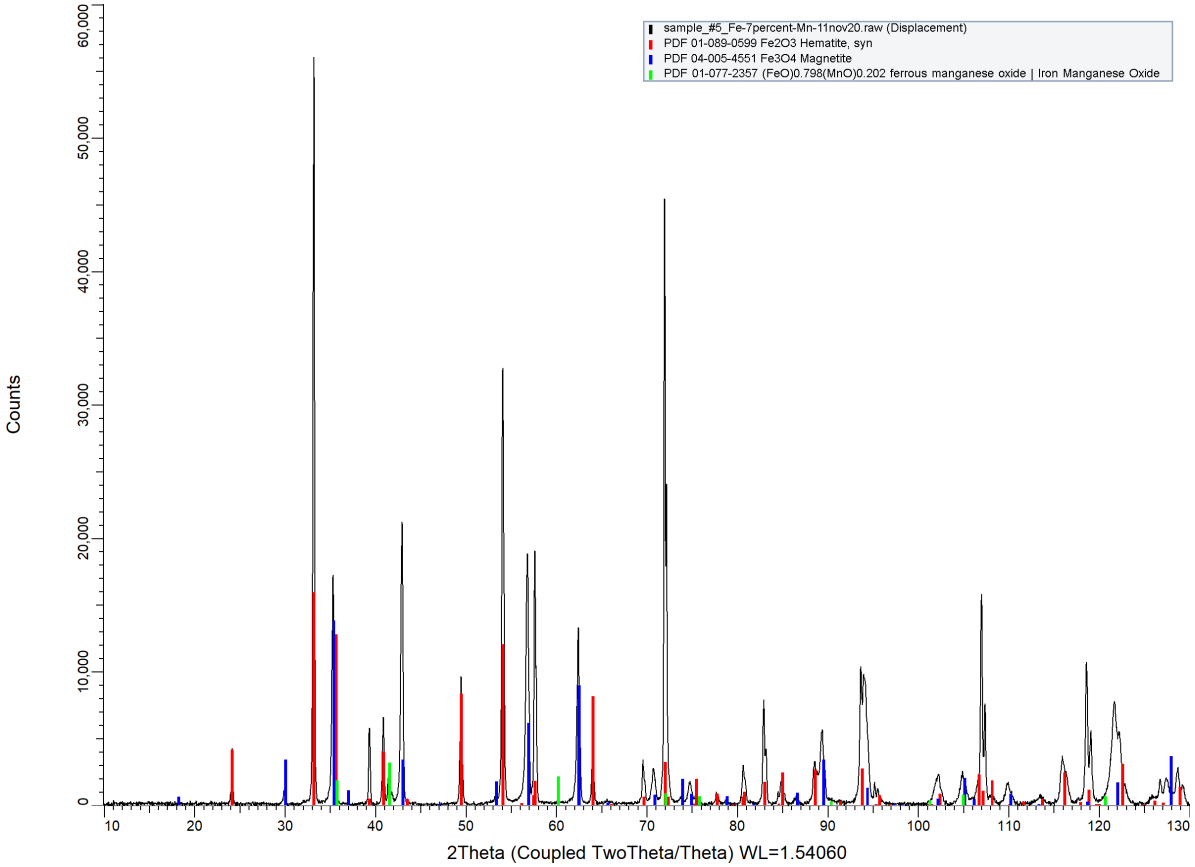

Figure 3.2: XRD pattern of the oxide layer surface of Fe-7%Mn [24]

4

High Temperature XRD Experiment

4.1. Objective

The objective of the experiment is to perform the high temperature oxidation of Fe-Mn binary alloy with conditions similar to that of the short-time oxidation described earlier in this report, while simultaneously studying the formation of the oxide phases with respect to time, through characterisation with XRD using standard powder diffraction methodology. Observing the formation of magnetite is of particular interest, in order to verify whether its formation occurs during high temperature short-time oxidation specifically, or at some other point during the experiment.

4.2. Sample

The sample is a small sheet of dimensions 7.2 mm × 8 mm × 1 mm having the composition of Fe-3%Mn. Since all the Fe-Mn binary alloys have the presence of magnetite in the oxide phase, arbitrarily the sample with the composition of Fe-3%Mn was chosen for the HT-XRD experiment. The sample was originally of the dimensions 15 mm × 8 mm × 2 mm, but has been machined using electrical discharge machining (EDM) to smaller dimensions in order to fit into the sample holder of the available set-up.

4.3. XRD Parameters Calculation

Since the objective of the experiment is to recreate the conditions of the short-time oxidation experiments performed earlier while characterising the oxide phases, it is necessary to be able to finish the XRD scan for the phases of interest within the stipulated time for a short-time oxidation experiment. Since previously, during the XRD analysis, it had been determined that the step size for the scan was of the order 0.03°2θ and the step time is 2 sec, for a 2θ range of say, 20-100°, the time taken per scan would be in the order of 1.5 hrs, which exceeds the time for a short-time oxidation experiment by a large amount. One solution to this issue is to reduce the 2θ range to include only the peaks of highest intensity of the phases of interest to be shown on the resulting diffraction pattern. In order to reduce the 2θ range for which the XRD scan can be performed, it is necessary to know the 2θ angles at which the highest intensity peaks occur for the different oxides. In the following sections, the calculations of the required parameters for the identification of the highest intensity peaks of the phases of interest using XRD are briefly explained. Since the effect of temperature on the lattice parameter in the range 1000-1100°C is not significant for this experiment [2], it has not been taken into account. All the calculations were performed using MS Excel.

4.3.1. Lattice Parameter

The lattice parameters for pure Fe and pure Mn are easily available in literature and as Powder Diffraction Files (PDF), however for the characterisation of the Fe-Mn binary alloys, it is necessary to know the lattice parameter of the alloy after taking into account the effect of the variation in Mn% on the lattice parameter. According to [30], the lattice parameters (in nm) for α and γ iron can be calculated using the following equation:

$$a_\alpha = 0.28664 + (0.00543 \pm 0.00016)x_{\mathrm{Mn}}$$
$$a_\gamma = (0.35729 \pm 0.00005) + (0.01144 \pm 0.00018)x_{\mathrm{Mn}} \quad (4.1)$$

where x_{Mn} = the mole fraction of Mn in the alloy
a_α, a_γ = the lattice parameters of the ferrite (α) and austenite (γ) phases

In the case of the other phases of interest i.e. the Fe oxides, according to [15], the lattice parameters are summarised in Table 4.1

Table 4.1: Table listing the lattice parameters of some iron oxides [15]

Phase	Crystal System	Lattice Parameter	
		a (nm)	c (nm)
Hematite (Fe_2O_3)	Hexagonal	0.5038	1.3772
Magnetite (Fe_3O_4)	Cubic	0.84	-
Wüstite (FeO)	Cubic	0.43	-

4.3.2. Interplanar Spacing

In order to determine the interplanar spacing d_{hkl}, the following steps were taken:

Bragg's law states that [16]:

$$n\lambda = 2d' \sin\theta \quad (4.2)$$

where n = order of reflection
d'(d_{hkl}) = interplanar spacing
θ = angle of reflection

Also for cubic crystal lattices:

$$d_{hkl} = \frac{a}{\sqrt{h^2 + k^2 + l^2}} \quad (4.3)$$

where a = lattice parameter
h, k, l = Miller indices

The above is valid for cubic crystal systems and has been derived from the Bragg equation for a generalised Bravais lattice and is given by the equation (4.4) found in [9]:

$$\frac{1}{d^2} = \frac{1}{V^2}\left(S_{11}h^2 + S_{22}k^2 + S_{33}l^2 + 2S_{12}hk + 2S_{23}kl + 2S_{31}lh\right) \quad (4.4)$$

where V is the volume of the unit cell given by:

$$V = abc\sqrt{1 - \cos^2\alpha - \cos^2\beta - \cos^2\gamma + 2\cos\alpha\cos\beta\cos\gamma} \quad (4.5)$$

and the constants S_{ij} (representing the relations between the unit cell edges and angles for the different crystal systems) are given by:

$$S_{11} = b^2c^2\sin^2\alpha$$
$$S_{22} = c^2a^2\sin^2\beta \quad ; S_{33} = a^2b^2\sin^2\gamma$$
$$S_{12} = abc^2(\cos\alpha\cos\beta - \cos\gamma)$$
$$S_{23} = a^2bc(\cos\beta\cos\gamma - \cos\alpha)$$
$$S_{31} = ab^2c(\cos\gamma\cos\alpha - \cos\beta) \quad (4.6)$$

In the case of α-ferrite, the crystal lattice is known to be body centred cubic (bcc) and in the case of γ-austenite, the crystal lattice is known to be face centered cubic (fcc), so the simplified version for the d_{hkl} can be calculated as given in (4.3).

The oxides wüstite and magnetite are also known to have a cubic structure so the equation as per (4.3) can be used, however for the case of hematite for example, the crystal lattice has a hexagonal structure ($\alpha = \beta = 90°, \gamma = 120°$ and $a = b \neq c$) and so the equation give as per (4.4) will have to be modified accordingly.

On substituting values for hexagonal lattice into the generalised equations, the following equation is obtained [16]:

$$\frac{1}{d_{hkl}^2} = \frac{4}{3} \cdot \frac{h^2 + hk + k^2}{a^2} + \frac{l^2}{c^2} \tag{4.7}$$

where a,c = lattice parameters for hexagonal crystal system
d_{hkl} = interplanar spacing
h, k, l = Miller indices

4.3.3. Allowed Reflections

The structure factor for the different reflections possible according to the crystal structure are as given in Table 4.2.

Table 4.2: Diffraction Selection Rules

Unit Cell Type	Allowed Reflections	Forbidden Reflections
Primitive	Any H,K,L	None
Body Centered	H+K+L = 2n (even)	H+K+L = 2n+1 (odd)
Face-centered	H,K,L all odd or all even	H,K,L mixed odd, even
Hexagonal (HCP)	L even; H+2K≠3n	L odd and H+2K = 3n

4.3.4. Final Range Estimation

After obtaining all of the above data, a summary of the calculated values for obtaining the possible peaks for Fe-3%Mn are then given in the table 4.3. In the table, the highlighted values are the 2θ at which the highest peak intensities were likely to be observed. On observation from the table, the 2θ at which the three highest peak intensities for the three oxides of interest occur all seem to fall within the range of 34-62°. This has also been corroborated by the XRD data from [23], as can be seen from the close-up of the XRD pattern in the given range in 4.1.

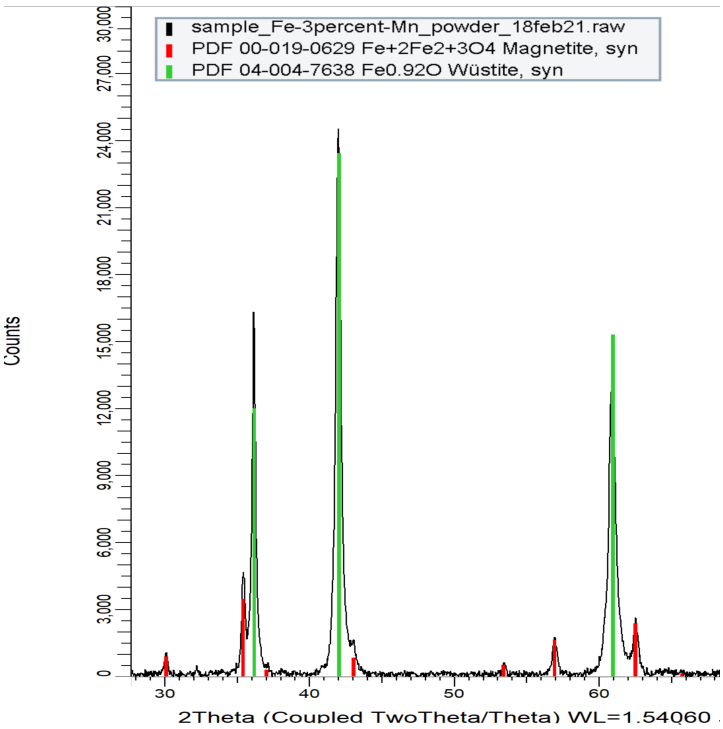

Figure 4.1: Figure showing the peaks for the oxide phases in the range $32 - 62$ ° in the XRD pattern for Fe-3%Mn (oxidised in 20%O_2 at 1000 °C for 20 min) [23]

Table 4.3: The calculated parameters for the XRD characterisation of Fe-3%Mn binary alloy

Fe-3%Mn															
Mn Mole Fraction:							0.0305								
a_α (nm) =			0.287				a_γ (nm) =				0.358				
Miller Indices			Magnetite (fcc)		Ferrite(α) (bcc)		Austenite(γ) (fcc)		Wüstite (fcc)		Hematite (hcp)				
h	k	l	d_{hkl}	2θ	d_{hkl}	2θ	d_{hkl}	2θ	d_{hkl}	2θ	h	k	l	d_{hkl}	2θ
1	1	0			0.203	44.644					1	0	0	0.436	20.337
1	1	1	0.490	18.080			0.207	43.800	0.248	36.151	0	0	2	0.689	12.845
2	0	0	0.425	20.907	0.143	64.978	0.179	51.023	0.215	41.988	1	0	1	0.416	21.345
2	1	1			0.117	82.273					1	0	2	0.369	24.128
2	2	0	0.300	29.735	0.101	98.862	0.126	75.048	0.152	60.885	1	0	3	0.316	28.194
3	1	0			0.091	116.268					1	1	0	0.252	35.611
3	1	1	0.256	35.020			0.108	91.159	0.130	72.900	2	0	0	0.218	41.353
2	2	2	0.245	36.632	0.083	136.978	0.103	96.487	0.124	76.711	1	1	2	0.237	38.005
3	2	1									2	2	0	0.126	75.407
4	0	0	0.212	42.553			0.089	118.945	0.108	91.539	3	1	0	0.121	79.070
3	3	1	0.195	46.585					0.099	102.674	2	0	1	0.215	41.893
4	2	0	0.190	47.870					0.096	106.474	0	0	4	0.344	25.856
4	2	2	0.173	52.773							2	0	2	0.208	43.479
3	3	3	0.163	56.248							1	0	4	0.270	33.117
4	4	0	0.150	61.751							2	0	3	0.197	46.025
4	4	2	0.142	65.954							2	1	0	0.165	55.692
5	1	1	0.163	56.248							2	1	1	0.164	56.125
											1	1	4	0.203	44.530
											1	1	6	0.170	54.002

4.4. Specifications

The following specifications were finally used for the HT-XRD experiment:

- An X-ray diffractometer with a mounted heater is to be used for the experiment. Cu Kα radiation will be used for the experiment. Sample was clamped in an Anton-Paar DHS1100 high temperature stage and was measured at the center position. Cu Kα radiation source was used.
- Locked coupled scans were in the 2θ range: $22 - 55$ °, with a step size of 0.05 ° and a step time of 1 sec.
- Scans were performed at room temperature, 500 °C, 900°C and 1000°C during both the heating and cooling periods. There was approximately a time difference of half an hour between scans.
- The heating and cooling rates of the sample in order to attain the different target temperatures at which the scans take place were not regulated, but were very fast and in the range of 100 °C/ min.

4.5. Procedure Outline

- The procedure for the experiment involves initially heating the sample to a temperature of 1000 °C in an inert atmosphere (pure N_2 is preferred) at a total pressure of 1 atm. After the target temperature is reached, an XRD scan is performed in the range of $22 - 55$ ° in order to confirm the sample phase as austenite. With the given parameters (see above) this should take about 15 min, during which the chamber atmosphere is homogenised.
- The atmosphere is then switched to a combination of N_2-20%O_2 and this condition is held for about an hour. During oxidation, a quick scan is performed at the different temperatures specified, in order to detect the sequential formation of the oxides wüstite and magnetite. Through this method only the first few highest intensity peaks of each oxide phase can be detected.
- Then the atmosphere is once again changed to pure N_2, and the sample is cooled down to room temperature. During the cooling down process as well, XRD scans are performed once the specified temperature is attained to verify formation of magnetite.

4.6. Results and Discussion

Before oxidation, the XRD scan of sample at 1000°C shows an austenite phase due to the transformation of ferrite to austenite at temperatures >910°C. Once oxidised, the oxide layer is likely to consist mostly of wustite. The figure 4.2 shows the formation of wustite as the temperature increases. However, since the XRD scans in Chapter 3 have revealed the presence of magnetite, this magnetite is likely to be formed due to the decomposition of wustite into magnetite due to instability at temperatures <570°C during the cooling process. The formation of magnetite at 500 °C during the cooling period and its persistence at room temperature can be observed from the figure 4.2 and can also be observed from the figures attached in A.4.

As temperature rises, there is formation of oxide because the N_2 gas supplied was possibly not pure and as a result some amount of O_2 was present from the beginning of the experiment. At 500 °C, unexpectedly small amounts of magnetite was detected but it does not recur in the subsequent scans. Besides these two points, the formation of wustite until the temperature of 1000 °C and the presence of magnetite during the cooling cycle at 500 °C can be observed.Thus the presence of magnetite in the scale is not a result of the diffusion mechanism through the wustite oxide layer during the high temperature oxidation but can be confirmed as due to the decomposition of wustite to magnetite and ferrite at lower temperatures via the equation below [8]:

$$4\mathrm{Fe}_{1-\mathrm{x}}\mathrm{O} \rightarrow \mathrm{Fe}_3\mathrm{O}_4 + (1 - 4\mathrm{x})\mathrm{Fe} \tag{4.8}$$

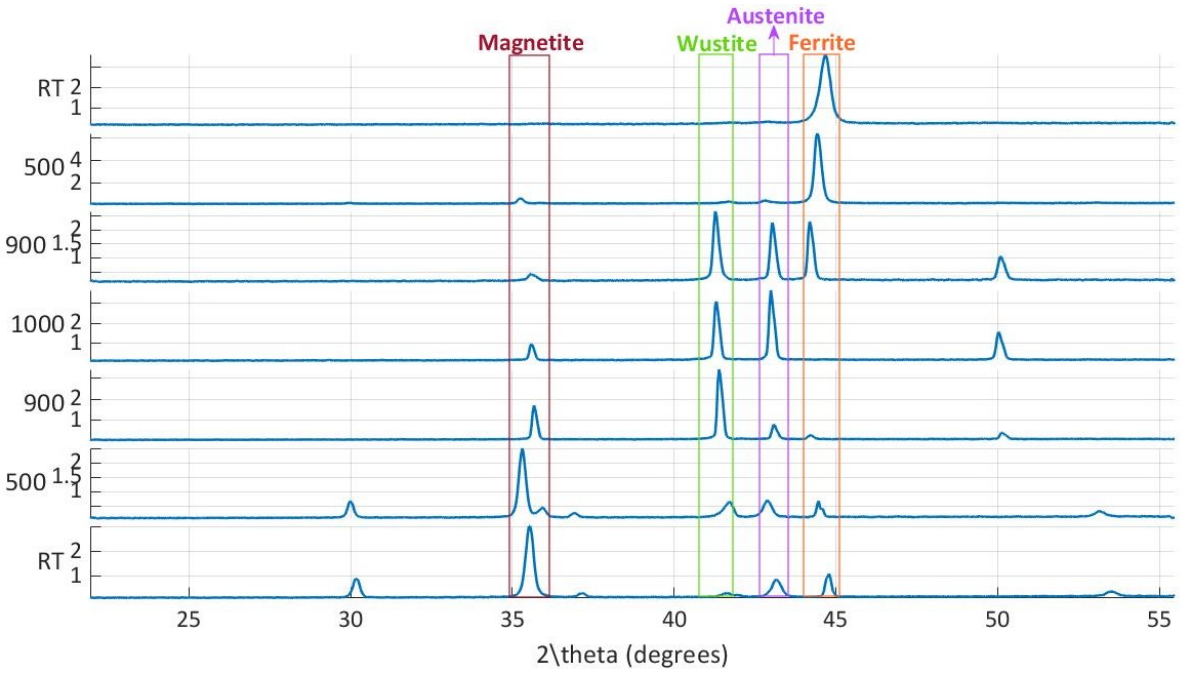

Figure 4.2: HT-XRD results of Fe-3%Mn at different temperatures (given to the left of the y-axis in °C; RT refers to room temperature) showing the formation of the phases. [25]

The evolution of the wüstite scale to form magnetite has been discussed also in [12], wherein it was observed that the formation of magnetite and the resulting scale structure was affected by the temperature at which the oxidation occurred and the rate at which the sample was cooled, and also reported that the formation of magnetite could be decreased (and the amount of retained wüstite increased) by increasing the cooling rate.

5

Mechanism of Oxidation

In order to determine the mechanism of the oxidation that occurs during the short-time oxidation experiments conducted in this project, it is necessary to evaluate whether the methods existing in literature for the prediction of the linear rate constants can give an accurate estimation of the same, or whether the value of the linear constant that has been theoretically arrived at is close to the experimentally determined value. Since these methods for predicting the theoretical rate constants are based on different models of oxidation, a close match between theoretical and experimental linear rate constants can give a good indication of the mechanism by which the high temperature oxidation takes place in the Fe-Mn binary alloys under study.

Studies such as Abuluwefa et al. [22] and Yuen et al.[49] have briefly summarised and theorised potential mechanisms of oxidation based on the effect of the oxygen concentration and temperature ranges. However since the literature available on Fe-Mn binary alloys specifically is limited, the models that will be tested in this chapter will be those developed for variants of low-carbon steel in $O_2 - N_2$ binary gas atmospheres.

5.1. Theoretical Linear Rate Constant

From the data obtained during the oxidation experiments (see chapter 2 and the Appendix A.1), it is observed that the rate of growth of the oxide layer follows a linear trend. As previously discussed, the possible mechanisms for the formation of oxide according to the rate of oxidation could be:

- *Linear*: Surface reactions or gas transport from the bulk gas in the oxidising atmosphere
- *Parabolic*: Solid phase diffusion of iron or oxygen ions through the oxide layer

Since the oxidation is clearly in the linear regime, and because surface reactions are known to be the controlling mechanism only in the case of low oxygen atmospheres such as $CO - CO_2$ [37], the gas diffusion from the atmosphere to the reaction surface is likely to be the rate determining mechanism. Knowing that the major oxide formed during the oxidation is wüstite, the equation for the linear rate constant can be given by [22]:

$$k_l = M_{\mathrm{O}} k_{\mathrm{MTC}} \left(C^{\mathrm{G}}_{\mathrm{O}_2} - C^{*}_{\mathrm{O}_2} \right) \tag{5.1}$$

where k_{MTC} = the mass-transfer coefficient (cm/s)
M_O = the molar mass of atomic oxygen $(g/g-mol)$
C_{O_2} = the molar concentration of oxygen in the gas mixture ($moles/cm^3$), where the superscript 'G' refers to the bulk of the gas and '*' to the sample surface.

Table 5.1: Experimental specifications during oxidation

Parameter	Value	Unit
Total Pressure	1	atm
Total flow rate	53.3	ml/min
Furnace Chamber Diameter	18	mm
Furnace Chamber cross-sectional area	10.18	cm^2
Gas Velocity	0.087	cm/s
Sample length	1.5	cm
Furnace Chamber Volume	285	cm^3

Table 5.2: Gas properties used for calculations (from Poirier and Geiger [41])

Property	Gas		Unit
	O_2	N_2	
Molar Mass	32	28	gm/mol
Lennard-Jones Parameters			
σ	3.467	3.798	nm
$\frac{\varepsilon}{k_B}$	106.7	71.4	K
Critical Constants			
T_C	154.6	126.2	K
V_C	50.4	89.8	cm^3/mol
Diffusion Volume	16.6	17.9	-

Also from Abuluwefa [22] and Chen [50],

$$k_{\mathrm{MTC}} = \frac{4}{3}\frac{D_{\mathrm{O_2}}}{l}(\mathrm{Re})^{1/2}(\mathrm{Sc})^{1/3} \tag{5.2}$$

where Re = Reynolds number (ul/ν)
Sc = Schmidt number (ν/D_{O_2})
D_{O_2} = diffusion coefficient of oxygen in the binary gas mixture (cm^2/s)
u = gas velocity past the sample surface (cm/s)
l = length of the sample (cm)
ν = kinematic gas viscosity (cm^2/s)[1]

The $D_{O_2}(\mathrm{cm^2\ s^{-1}})$ can further be calculated via the equation for the diffusion coefficient of O_2 in a binary mixture of O_2 and N_2 [40] :

$$D_{AB} = \frac{\left(1\times10^{-3}\right)T^{1.75}}{p\left(v_B^{1/3}+v_A^{1/3}\right)^2}\left[\frac{1}{M_A}+\frac{1}{M_B}\right]^{1/2} \tag{5.3}$$

where T = temperature, K
p = pressure, atm
M_A, M_B = molecular weight of species A and B, $gmol^{-1}$,
v_A, v_B = diffusion volumes [2]

Here, except for the system pressure and temperature, all the quantities required are constants whose values are easily available in various databases. The constants used for the calculations are given in the Tables 5.1 and 5.2.

[1] In [22], the units of kinematic viscosity ν has been given as $gm/cm-sec$ but this is a typographical error and has been corrected accordingly.

[2] According to Fuller et al.[20], the diffusion volume is a dimensionless special diffusion parameter whose value has been arrived at by least square analysis for the specific use in equation 5.3.

In order to calculate the kinematic viscosities (given by $\nu = \eta/\rho$, where η is absolute viscosity and ρ is density) so as to arrive at Re and Sc, the absolute viscosity (η) for the two gases has to be calculated for the different temperatures at which the oxidation experiment is taking place. This is arrived at by first calculating the viscosity of the individual gas [41]:

$$\eta = 2.67 \times 10^{-5} \frac{\sqrt{MT}}{\sigma^2 \Omega_\eta} \tag{5.4}$$

where M = molecular weight of the species
T = temperature in Kelvin
σ = characteristic diameter of the molecule in Å
Ω_η = collision integral of the Chapman-Enskog theory, which is a function of a dimensionless temperature parameter $\frac{k_B T}{\varepsilon}$

The Ω_η is calculated by first finding the parameter given by $\frac{k_B T}{\varepsilon}$ for the temperature of interest for each gas and then finding the value as given in Poirier and Geiger [41], assuming the Ω_η scales linearly with the parameter $\frac{k_B T}{\varepsilon}$.

In order to calculate the viscosity for a mixture of gases, the following conventional method given by Poirier and Geiger [41] is used:

$$\eta_{\text{mix}} = \sum_{i=1}^{n} \frac{x_i \eta_i}{\sum_{j=1}^{n} x_j \Phi_{ij}} \tag{5.5}$$

in which

$$\Phi_{ij} = \frac{1}{\sqrt{8}} \left[1 + \frac{M_i}{M_j}\right]^{-1/2} \left[1 + \left[\frac{\eta_i}{\eta_j}\right]^{1/2} \left[\frac{M_j}{M_i}\right]^{1/4}\right]^2 \tag{5.6}$$

where n = number of chemical species in the mixture
x_i and x_j = the mole fractions of species i and j
η_i and η_j = the absolute viscosities of species i and j at the system temperature and pressure
M_i and M_j = the corresponding molecular weights

Note that Φ_{ij} is dimensionless, and when i = j, Φ_{ij} = 1.

Using the ideal gas equation,

$$pV = nRT \tag{5.7}$$

where p = pressure (atm), V= volume (litre)
n = moles, R= gas constant ($0.0821 \frac{l.atm}{mol.K}$)
T = temperature (K)

The densities of each gas and of the binary mixture of gases at the different temperatures were calculated.

Using the calculated values of the absolute viscosities and densities of the gas mixtures at various temperatures (see Figure 5.1), the kinematic viscosities of the same were calculated. These were then used for the calculation of the dimensionless Reynolds and Schmidt numbers as required for the calculation of the mass transfer coefficient k_{MTC}.

Finally for the calculation of the theoretical linear rate constant, there is the requirement for the oxygen concentration at the surface of the sample and in the bulk of the atmosphere i.e. $C^*_{O_2}$ and $C^G_{O_2}$ respectively. A calculation of the form given below is done in order to find the oxygen concentration in the furnace chamber in terms of $moles/cm^3$. Assuming that the gas is homogeneous in the furnace chamber:

- First, using the ideal gas equation and assuming ideal gas behaviour, the volume occupied by the gas mixture at the system conditions (for example: p= 1 atm, n= 1 mole, R= 0.082 $\frac{l.atm}{mol.K}$, T= 1000 °C).
- Then the number of moles of gas present in 1 cm^3 is found out.

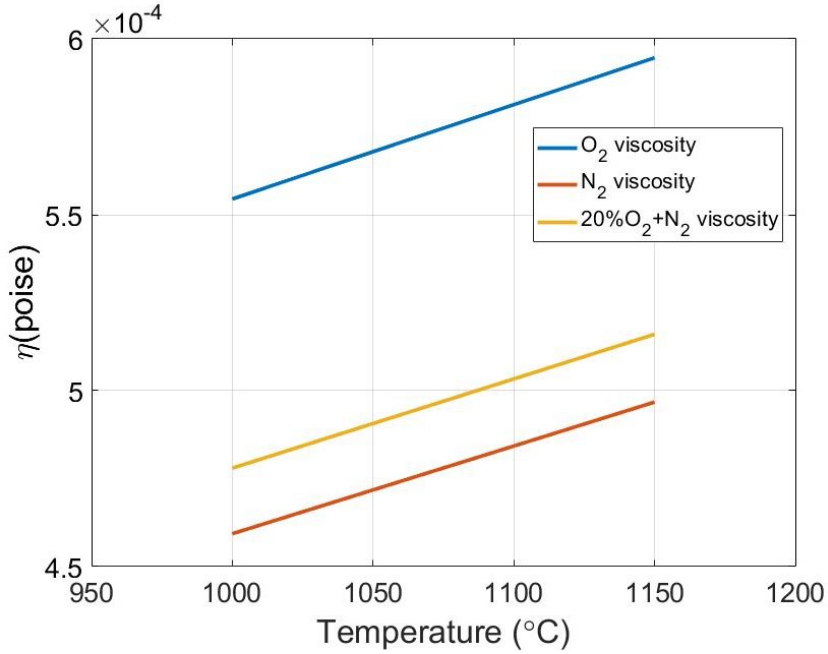

(a)

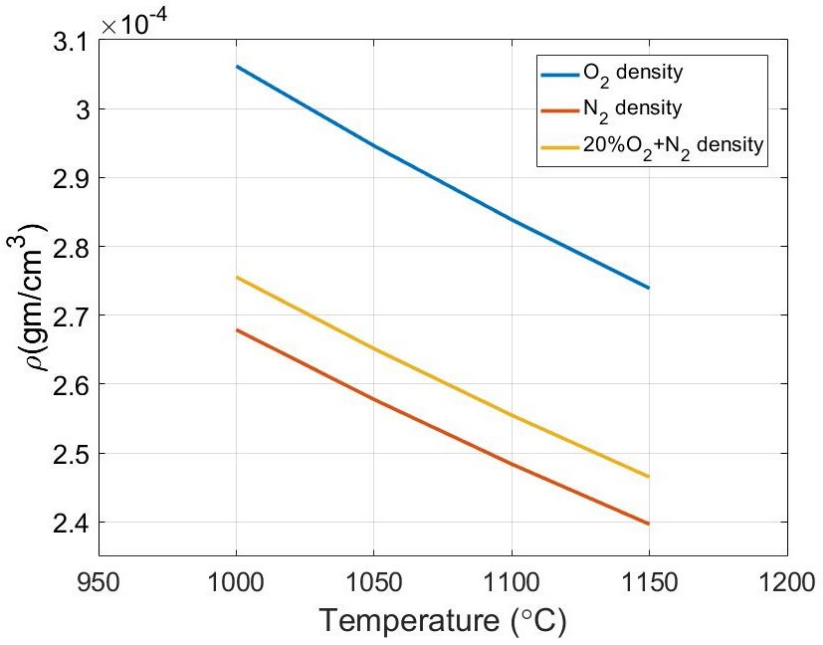

(b)

Figure 5.1: The dependence of the (a) viscosity and (b) density of O_2 and N_2 gas on temperature.

- The total moles of gas in the furnace chamber is then found by multiplying the above obtained quantity with the furnace volume already calculated using the available furnace dimensions (see Table 5.1).

- For 20%O_2, the mole fraction of the oxygen in the gas mixture at any time would then be 0.2. On multiplying the mole fraction with the total available moles in the furnace chamber, the number of moles of oxygen is obtained.[3]

[3]Avogadro's law: Equal volumes of ideal gases at same temperature and pressure have same number of moles - so the volume fraction translates to mole fraction.

- On dividing the number of moles of oxygen by the volume of the furnace chamber, the concentration of oxygen in terms of $moles/cm^3$ is obtained.

Another assumption made is that the oxygen concentration at the sample surface is zero. Since the oxidation occurs rapidly, it is assumed that the oxygen at the surface of the sample is always immediately consumed and that there is not enough time for the oxygen from the bulk of the gas to replenish the oxygen at the surface of the sample through mass transport. This is also mentioned in Chen et al.[13] as when the scale is very thin and the solid diffusion is rapid, the mass transport of the oxygen in the bulk is the rate determining mechanism, so the partial pressure of oxygen at the scale-gas interface is considered the same as that at the metal-scale interface. Then the theoretical rate constant is dependent only on the concentration of the oxygen in the furnace chamber.

After calculation, the theoretical linear rate constant is compared with the experimentally obtained linear rate constant (see Table:5.3), and it can be observed that there is a 24-40% overestimation of the calculated values in comparison to the observed values, i. e. the theoretically calculated rate constants are higher than the observed experimental rate constants. The percentage deviation is given in the table 5.3 and appears to be systematic rather than a result of experimental parameters as the degree of deviation is consistent across a range of varying experimental conditions. However there appears to be a higher deviation of the theoretical rate constant from the experimental rate constant at higher O_2 vol% (see Figure 5.2a), which is a trend similar to what is seen in [22].

By using the above method of calculation, the theoretical rate constant has a dependence on the oxygen concentration in the oxidising atmosphere of the furnace chamber that is similar to that of the experimental rate constant, proving that the rate determining mechanism of the oxidation is in fact the gas phase transport of the oxygen from the bulk gas to the reaction surface of the sample. The effect of temperature, in the range 1000-1150 °C, on the linear rate constant was not significant (see Fig. 5.2b).

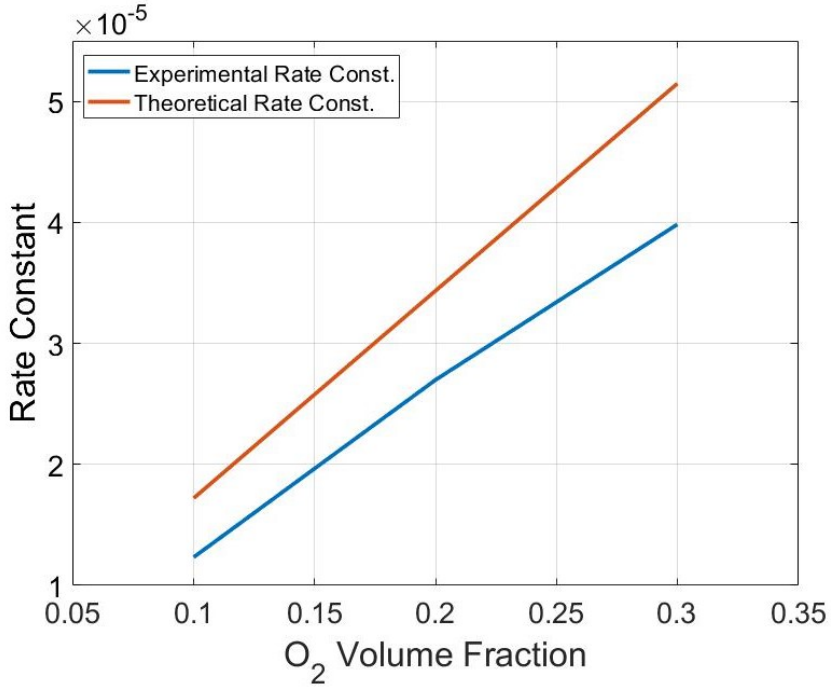

(a)

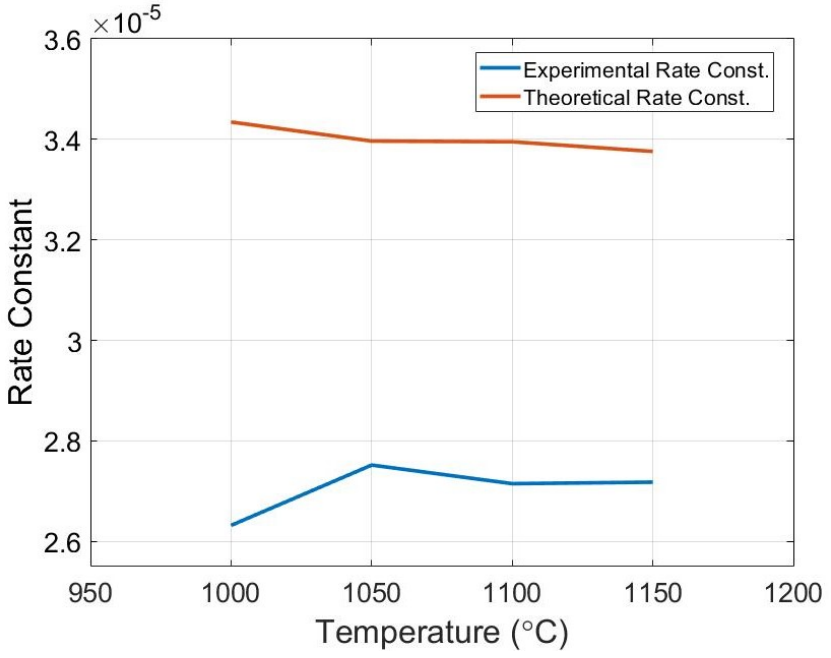

(b)

Figure 5.2: The dependence of experimental and theoretical rate constant for Fe-7%Mn on (a) the oxygen concentration when oxidised at 1000 °C for 15 min and (b) temperature in 20% O_2 atmosphere.

Table 5.3: Comparison of experimental and theoretical linear rate constants for Fe-Mn alloys

Oxidation Time t min.	Oxidation Temperature T °C	Oxygen Mole Fraction X_{O_2}	Experimental Rate Constant $k_{l_{exp.}}$ $(g/cm^2 sec)$	Theoretical Rate Constant $k_{l_{theor.}}$ $(g/cm^2 sec)$	% Deviation
Fe-7%Mn					
15	1000	0.2	2.698×10^{-5}	3.434×10^{-5}	27.3
15	1000	0.3	3.983×10^{-5}	5.147×10^{-5}	29.22
15	1000	0.2	2.632×10^{-5}	3.434×10^{-5}	30.49
15	1000	0.1	1.233×10^{-5}	1.721×10^{-5}	39.55
20	1100	0.2	2.715×10^{-5}	3.395×10^{-5}	25.05
20	1050	0.2	2.752×10^{-5}	3.397×10^{-5}	23.42
20	1150	0.2	2.718×10^{-5}	3.376×10^{-5}	24.21
Fe-3%Mn					
20	1000	0.2	2.714×10^{-5}	3.434×10^{-5}	26.55
20	1100	0.2	2.724×10^{-5}	3.395×10^{-5}	24.64
Fe-0.5%Mn					
20	1000	0.2	2.693×10^{-5}	3.434×10^{-5}	27.53
20	1100	0.2	2.719×10^{-5}	3.395×10^{-5}	24.87

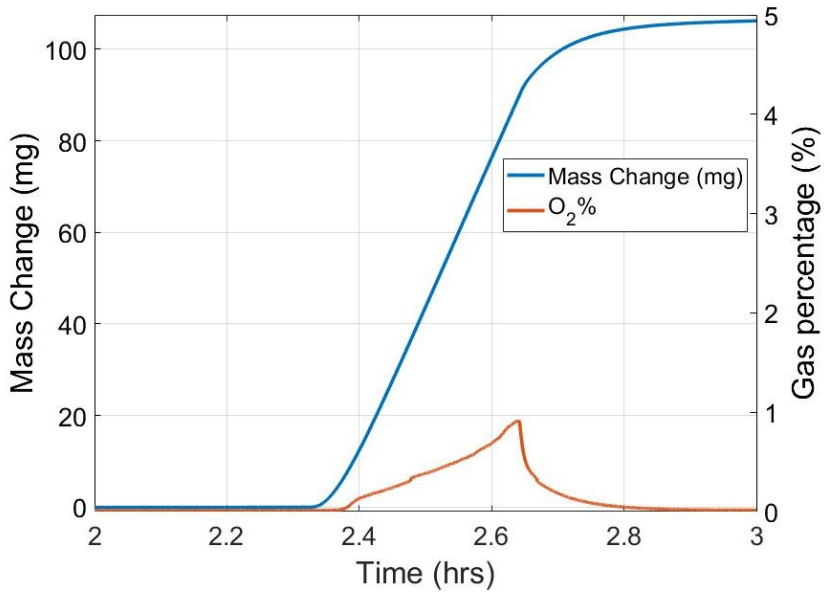

Figure 5.3: The variation in O_2 partial pressure for Fe-3%Mn sample oxidised at 1000 °C for 20 min in 20% $O_2 - N_2$ binary gas mixture in the TAG machine

Since an overestimation of 24-40% in the value of the calculated linear rate constant is quite large, the reasons for this deviation could be due to the following:

- The rapid consumption of oxygen during the initial stage of oxidation has an effect on the average concentration of the oxygen in the bulk of the gas especially at lower flow rates. This has been corroborated with the data from the Quadrupole Mass Spectrometry(QMS) readings that were recorded simultaneously during the oxidation experiments. For a sample (see fig. 5.3), the observed partial pressure of O_2 was much lower than the set values, and since the QMS sensor is placed 1 cm away from the sample, the deviation in expected value of partial pressure has been attributed to the rapid consumption of oxygen during the experiment. As a result, if the actual partial pressure of oxygen near the sample surface is determined (which is in fact lower than the set value assumed) and used for the calculation of the theoretical linear constant, it is possible to arrive at an estimate that is closer to the experimental value. In [13] also a similar variation in oxygen partial pressure near the oxidation sample has been discussed, and a lower value of the calculated linear rate constant was arrived at.

- Also, the assumption for the equations 5.1 and 5.2 is that the gas phase transport takes place in a semi-infinite space, where the gas flow over the sample is laminar, as also discussed in [13]. For this condition, the dimensions of the sample are considered to be much larger in comparison to the width of the boundary layer as given by the equation 5.8:

$$\delta_0 = 5.0 \times \left(\frac{v}{u}\right)^{1/2} x^{1/2} \tag{5.8}$$

  On using the values of gas velocity u = 0.087 cm/sec (given in Table 5.1), kinematic viscosity v varying from 1.72-2.1 cm^2/sec and the leading edge of the boundary layer (x) to be at 1.5 cm (length of the sample), the width of the boundary layer is between 27 and 31 cm. This is not possible as the dimensions of the sample itself are $1.5 \times 0.8 \times 0.2$ cm, and also the diameter of the furnace chamber used in the oxidation experiments is only 1.8 cm. So the condition of semi-infinite space was never fulfilled and therefore the mass transfer coefficients previously calculated are not the best estimate possible. The value of average gas velocity deduced from the gas flow rate also cannot be used as the value for the gas velocity near the sample surface, as the fluid does not follow the pattern for laminar flow. This also affects the estimation of the theoretical

rate constant, so if a correction factor for a better estimate of the gas velocity is used, it may be possible to have a better estimate of the theoretical rate constant as well.

- During the oxidation experiment, one of the underlying assumptions while switching between the active and inert atmospheres in the furnace is that the switch occurs immediately i.e. that a homogeneous atmosphere with the desired O_2 partial pressure is achieved without the requirement of additional time for homogenization. It is also assumed that there is negligible fluctuations in the set values of the partial pressure of the active gas (O_2) at least for the duration of the experiment. However, practically it is observed from the Quadrupole Mass Spectrometry (QMS) data that is acquired simultaneously during the oxidation experiment that these assumptions do not hold. On testing an inert "dummy" sample (made of alumina) with the set conditions of 20%O_2 for 15 min (see fig. 5.4), it was observed that some time was taken to for the set value of O_2 concentration to be reached. Also due to instrumental limitations, it is difficult to estimate the exact values of O_2 concentration in the furnace chamber while the oxidation experiment is being conducted. On using the following equation [35]:

$$\mathrm{C_n} = \frac{\mathrm{I_n^+}}{\mathrm{S_n}}[\mathrm{mbar}] \tag{5.9}$$

where $\mathrm{C_n}$ = the partial pressure of the component n [mbar]
$\mathrm{I_n}$ = ion current as measured for component $\mathrm{n[A]}$
$\mathrm{S_n}$ = the sensitivity for a corresponding gas [A/mbar]

the possible partial pressure values can be estimated from the ion current data obtained from the QMS (which is how the figure 5.4 has been obtained), however these values are not accurate. This also may have influenced the value of the overall experimental linear rate constant.

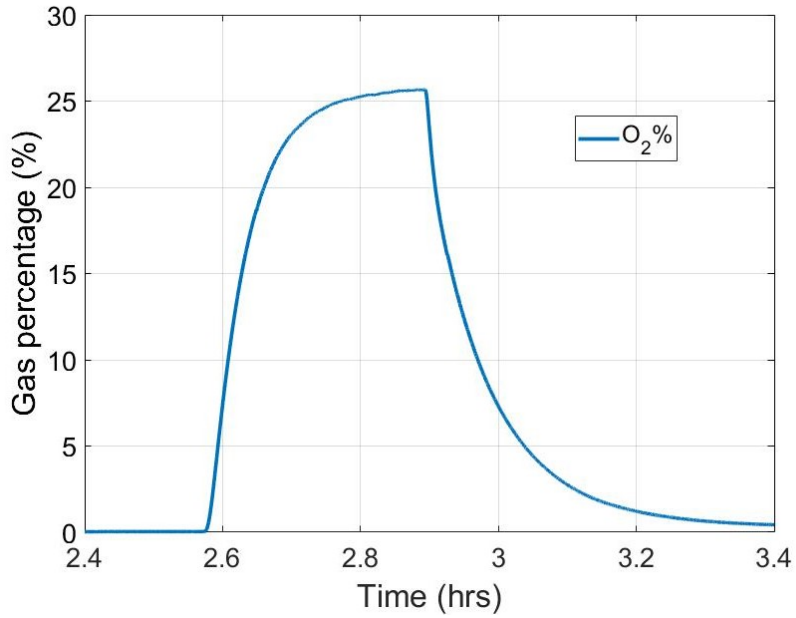

Figure 5.4: The variation in O_2 partial pressure with time using alumina sample in the TGA with a set value of 20% O_2.

5.2. Potential Oxidation Mechanism

Generally, the mechanism observed for the oxidation of iron is divided into two stages [22]: an initial linear rate of oxidation, followed by a parabolic rate of oxidation. the linear rate is usually observed for a short time until a critical thickness of oxide layer (of about $4 \times 10^{-3} - 0.1$ mm according to Pettit and Wagner [38]) is achieved, after which the rate of oxidation becomes parabolic.

Initial oxidation rates are observed to depend on the oxidizing species and can be controlled either by the rate of chemical reaction (i.e. the adsorption rate) at the metal surface or by the rate of transport of the oxidizing species through the gas mixture to the reaction surface. However since the surface

reactions occur rapidly, especially in oxidation environments with high O_2 concentration, [47] it is more likely that the transport of oxygen gas through the bulk of the oxidising atmosphere to the alloy surface then becomes the slower, rate-controlling step. This is also supported by the QMS data previously mentioned in this chapter, and that the oxidation at the sample surface occurs rapidly (leading to the rapid consumption of O_2 near the sample surface) in comparison to the rate at which the oxygen gas is made available near the sample.

It is also possible that the linear rate occurs due to the high porosity of the oxide layer [47], however this seems unlikely. According to [47], Pilling and Bedworth's study [39] states that if the volume of oxide formed on a metal sample is less than the volume of metal consumed in the oxidation reaction, then a porous oxide layer is likely to result, and it is possible to express this information as the Pilling-Bedworth ratio given below:

$$PBR = \frac{V_{OX}}{xV_M} \tag{5.10}$$

where V_M = the molar volume of the metal
V_{OX} = the molar volume of the oxide
x = moles of metal being consumed per mole of oxide formed

and can also be rewritten as:

$$PBR = \frac{\mathrm{M}_{\text{oxide}} \cdot \rho_{\text{metal}}}{\mathrm{n} \cdot \mathrm{M}_{\text{metal}} \cdot \rho_{\text{oxide}}} \tag{5.11}$$

where $\mathrm{M}_{\text{oxide}}$ = molar mass of the oxide
ρ_{oxide} = density of oxide
ρ_{metal} = density of the metal
$\mathrm{M}_{\text{metal}}$ = molar mass of metal
n = number of atoms of metal per molecule of the oxide

However, the calculated value of PBR for wüstite is 1.7-1.8 and this condition of having Pilling-Bedworth ratio of less than 1 is fulfilled only by alkali and alkali earth metals, according to the values listed in [36]. Further on, the calculated Pilling-Bedworth's ratios for all of the iron oxides listed, including magnetite and hematite, are also greater than 1.

As per [13] and [44], the linear rate constant in the case of iron oxidation in binary $O_2 - N_2$ gas mixtures, for oxygen concentration up to 3%, is controlled by the rate of transport of oxygen through the gas phase to the reaction surface. Further on, Selenz and Oeters [44] have stated that the linear rate constant observed for the oxidation of an iron sample in a binary $O_2 - N_2$ gas mixture is not significantly affected by the temperature of oxidation, which has also been confirmed by the data obtained from the experiments and can be observed in the Fig. 5.2b. However, this mechanism is observed to be applicable even to the effect of oxygen concentrations of 10-30%, which is the oxidising atmosphere of the furnace chamber for the experiments conducted in this study.

5.3. Conclusions

From the above discussions, it is clear that the binary Fe-Mn alloys under study does follow the same trend as low-carbon steel during oxidation of steel, however there are large deviations from existing models in terms of accurately determining the value of the linear rate constant theoretically. The rate determining mechanism is the gas transport of O_2 from the bulk gas to the sample surface through a gas boundary layer at the sample surface, and the rates of oxidation are highly dependent on the concentration of oxygen in the oxidising atmosphere. The effect of temperature on the other hand, at least for the range of 1000-1150°C, seems to be far lesser than that of oxygen concentration.

6

Conclusions & Recommendations

6.1. Conclusions

Based on the results obtained in the current research project, the following conclusions can be drawn:

- On isothermally oxidising the Fe-Mn alloy samples in the temperature range of 1000-1150 °C and p_{O_2} ranging from 0.1-0.3 atm, it was found that the rate was dependent on the partial pressure of oxygen in the furnace chamber, however it was found that the oxidation rate was independent of the Mn content. The linear regime of oxidation lasts for longer time in comparison to the literature reviewed and it has been hypothesized that this maybe due to the short-circuit diffusion of Fe ions through the grain boundaries of austenite, as a result of which the Fe ions are readily available for oxidation to wüstite for longer time periods. The critical thickness required for the transition from linear rate to parabolic rate of oxidation has also not yet been achieved.
- After the oxidation experiment, XRD characterisation of the oxide layer at room temperature showed that besides wüstite, magnetite was also identified even though only wüstite was expected to form in the linear regime of oxidation.
- Using HT-XRD, it was confirmed that only wüstite was formed during high temperature oxidation and the formation of magnetite was confirmed to be due to the instability of wüstite at temperatures lower than 570 °C. It was formed during the cooling cycle in the oxidation experiment. The cooling rate was not fast enough to prevent magnetite formation.
- In order to identify the rate determining mechanism for the high temperature oxidation, the theoretical rate constant for the same oxidation conditions is calculated, using a model available in literature. The rate determining mechanism has been confirmed to be the gas transport of O_2 from the bulk to the sample surface. The rate of oxidation is therefore sensitive to the oxygen concentration in the furnace chamber while the effect of the composition and temperature in the given ranges was not as significant.

6.2. Recommendations

In order to further understand the oxidation behaviour of Fe-Mn binary alloys and by extension the oxidation of steels, researching the following topics in depth could provide some useful insights:

- **Varying the oxygen partial pressure and gas flow rate**: As has already been studied in this project, the oxidation rate is dependent on the partial pressure of O_2. Varying the partial pressure of oxygen and the effect of the variation of gas flow rate on the gas phase boundary layer and the resulting comparison of the theoretical and experimental rates of oxidation could be a subject of exploration.
- **Transition from Linear to Parabolic Rate**: In the experiments conducted so far in this project, the linear rate exists for as long as 20 min. Data on the critical thickness of oxide necessary for the transition from linear to parabolic rate to occur and the time required for this to happen could give

information on the diffusion mechanism of the Fe^{2+} and O^{2-} ions during oxide formation. Some preliminary calculations have already been performed and detailed in A.5, however the estimates for the transition time is in the range of hours and it remains to be tested experimentally whether under the given experimental conditions the time taken for the transition of the oxidation rate from linear to parabolic is indeed in the same range.

- **Effect of higher cooling rates**: In this project, it was concluded that the wüstite formed at high temperature decomposed to magnetite on cooling, thus the final oxide structure available after the experiment is not the same as that obtained at the high temperature. An investigation on solving this issue could be performed such as by using a furnace with a faster cooling rate, enabling the sample to be quenched and thus preserve the high temperature oxide formed for further examination.
- **Effect of other atmospheric gases on oxide formation**: As the idea of this project was to contribute to the development of a generic oxidation model of steel, it would be worthwhile also to investigate the effect of varying concentration of atmospheric gases such as CO_2 and H_2O on the overall oxide formation and oxidation rates in Fe-Mn binary alloys.

A

Appendix

A.1. Mass Gain plots of high temperature oxidation

A.1.1. MATLAB code used for analysis and plotting

The code used to obtain the plots of the variation in furnace temperature and mass gain with respect to time are versions of the following lines for different mass gain datasets as obtained from the SETARAM TAG machine:

```
dataset_17_FeMn=xlsread('#17.xls','210126_FeMn7_20min_1150C_N2,O2_','A2:C14890');
timehrs1=dataset_17_FeMn(:,1);
furntemp=dataset_17_FeMn(:,2);
deltamass=dataset_17_FeMn(:,3);
figure(1);
hold on;
yyaxis left
p1=plot(timehrs1,furntemp);
ylabel('Temperature (\circC)');
yyaxis right
p2=plot(timehrs1,deltamass);
ylabel('Mass Change (mg)');
xlabel('Time (hrs)');
legend('Furnace Temp. (\circC)','Mass Change (mg)');
legend('Position',[0.65 0.7 0.025 0.07])
grid on
pbaspect([4 3 1])
p1.LineStyle = '-';
p1.LineWidth = 2.75;
p1.Marker = 'none';
p2LineStyle = '-';
p2.LineWidth = 2.75;
p2.Marker = 'none';
ax = gca;
ax.Box = 'on';
ax.FontSize=20;
ax.XLim = [0 inf];
ax.LabelFontSizeMultiplier = 1.2;
ax.GridColor = [0.11 0.11 0.11];
ax.GridLineStyle = '-';
yyaxis left
ax.YLim = [-1 1200];
ax.YColor = 'black';
```

```
yyaxis right
ax.YLim = [-1 100];
ax.YColor = 'black';
hold off;
```

For finding the rate constants, a similar code was used along with the 'Basic Fitting' tool:

```
lineartimehrs=dataset_17_FeMn(5961:6477,1);
%linfurntemp=dataset_17_FeMn(5961:6477,2);
lineardeltamass=dataset_17_FeMn(5961:6477,3);
lintimehrs=dataset_17_FeMn(:,1);
lindeltamass=dataset_17_FeMn(:,3);
lintimesec=lintimehrs*3600;
lindeltamasspera=lindeltamass./(3.32*1000);
lineartimesec=lineartimehrs*3600;
lineardeltamasspera=lineardeltamass./(3.32*1000);
figure(1);
hold on;
p1=plot(lintimesec,lindeltamasspera);
p2=plot(lineartimesec,lineardeltamasspera);
xlabel('Time (sec)');
ylabel('\Deltam/A (g/cm^2)');
legend('\Deltam/A (g/cm^2)','Linear region');
legend('Position',[0.65 0.7 0.025 0.07])
grid on
pbaspect([4 3 1])
p1.LineStyle = '-';
p1.LineWidth = 2.75;
p1.Marker = 'none';
p2.LineStyle = '-';
p2.LineWidth = 2.75;
p2.Marker = 'none';
ax = gca;
ax.XLim = [0 inf];
ax.Box = 'on';
ax.FontSize=20;
ax.LabelFontSizeMultiplier = 1.2;
ax.GridColor = [0.11 0.11 0.11];
ax.GridLineStyle = '-';
ax.YColor = 'black';
hold off;
```

A.1.2. Figures Obtained

The results obtained from the above code are given by the figures.
It can be observed that the k_l value is in the range of $1 - 3 \times 10^{-5}\ \frac{g}{cm^2 sec}$.

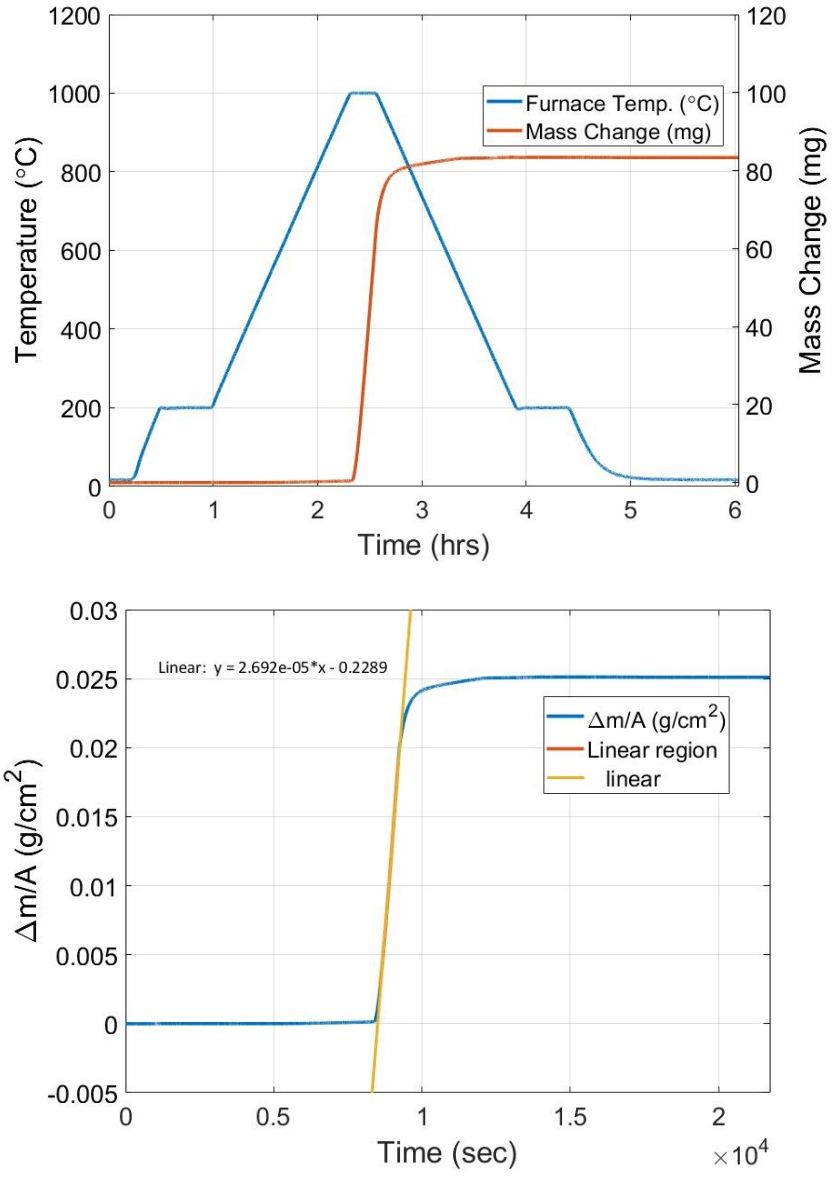

Figure A.1: Results for 201029 Fe-7%Mn alloy oxidised for 15 min in 20%O_2 at 1000 °C

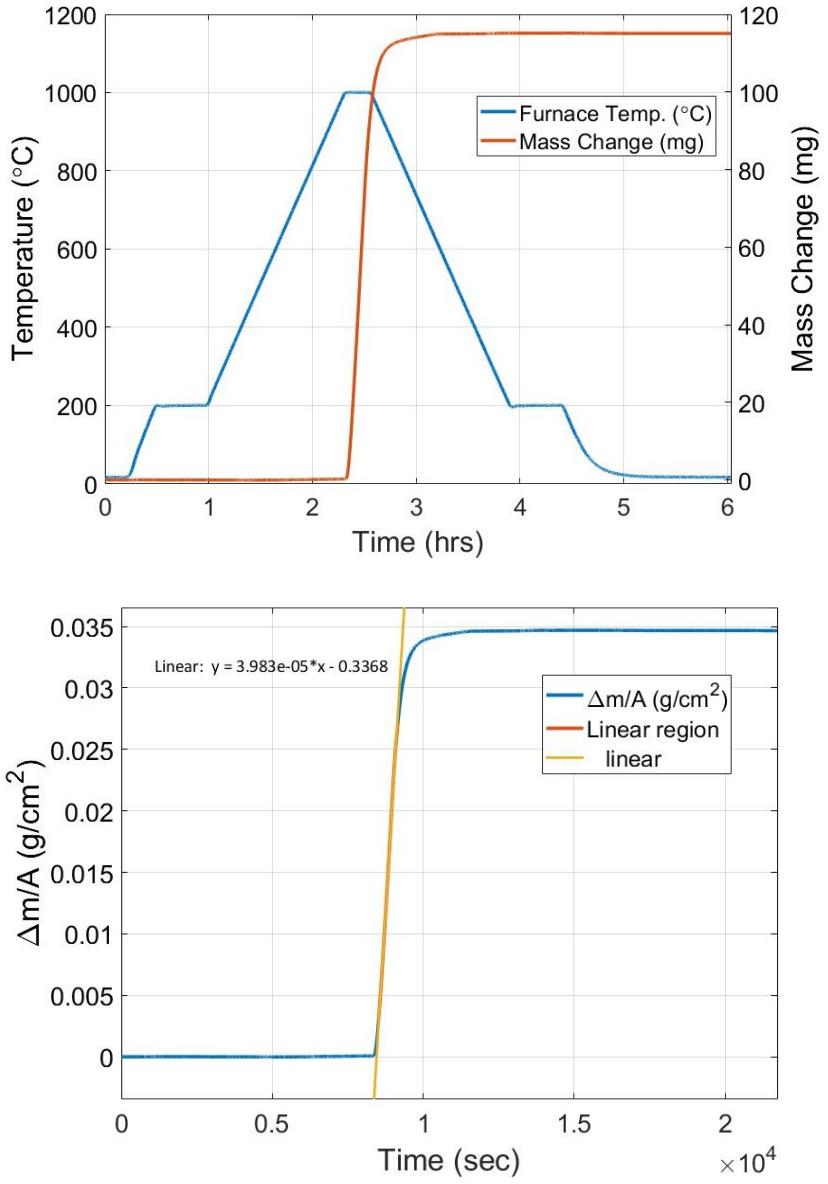

Figure A.2: Results for 201030 Fe-7%Mn alloy oxidised for 15 min in 30%O_2 1000 °C

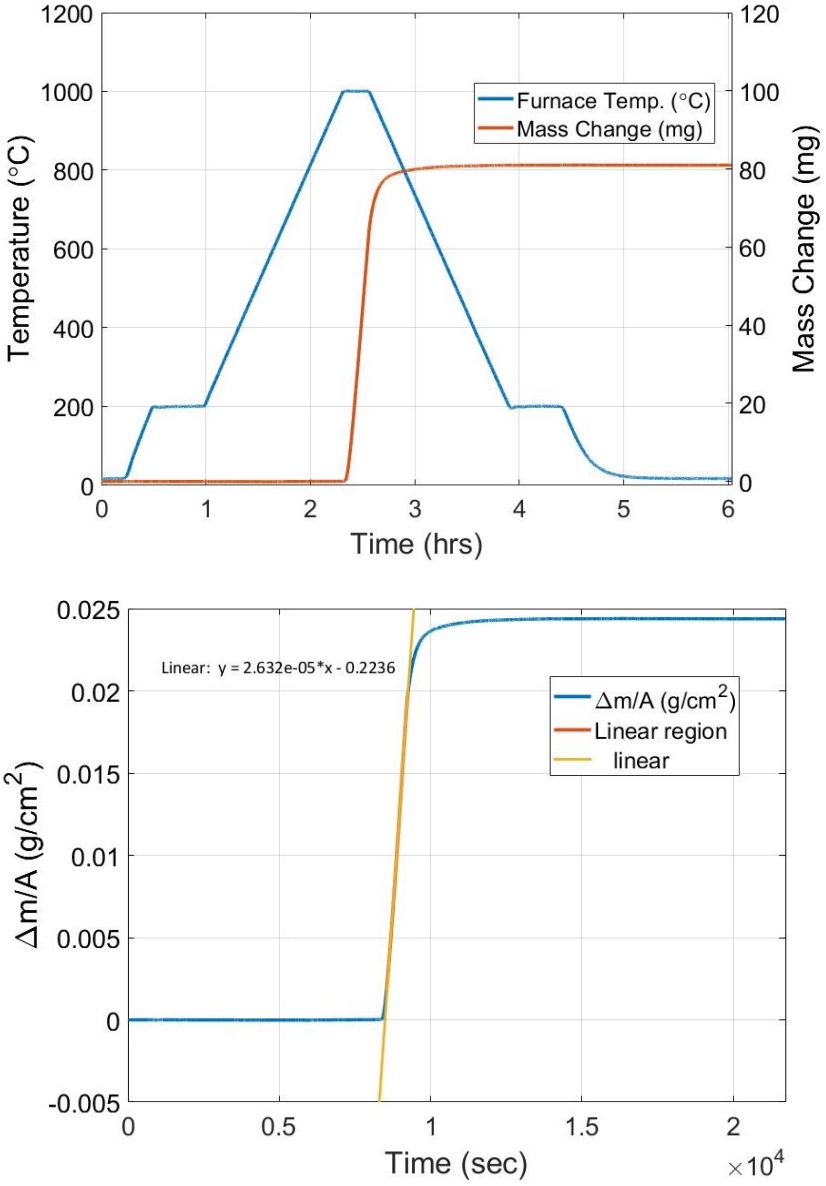

Figure A.3: Results for 201117 Fe-7%Mn alloy oxidised for 15 min in 20%O_2 at 1000 °C

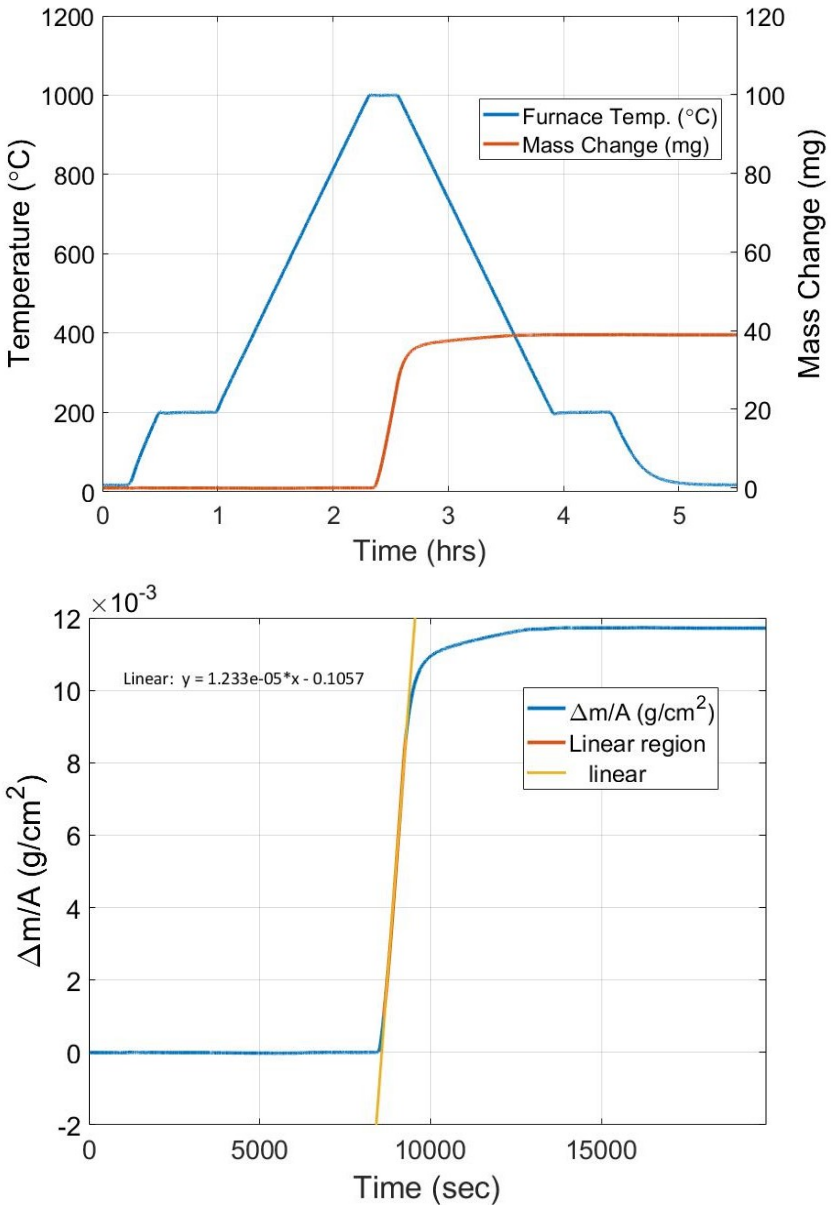

Figure A.4: Results for 201217 Fe-7%Mn alloy oxidised for 15 min in 10%O_2 at 1000 °C

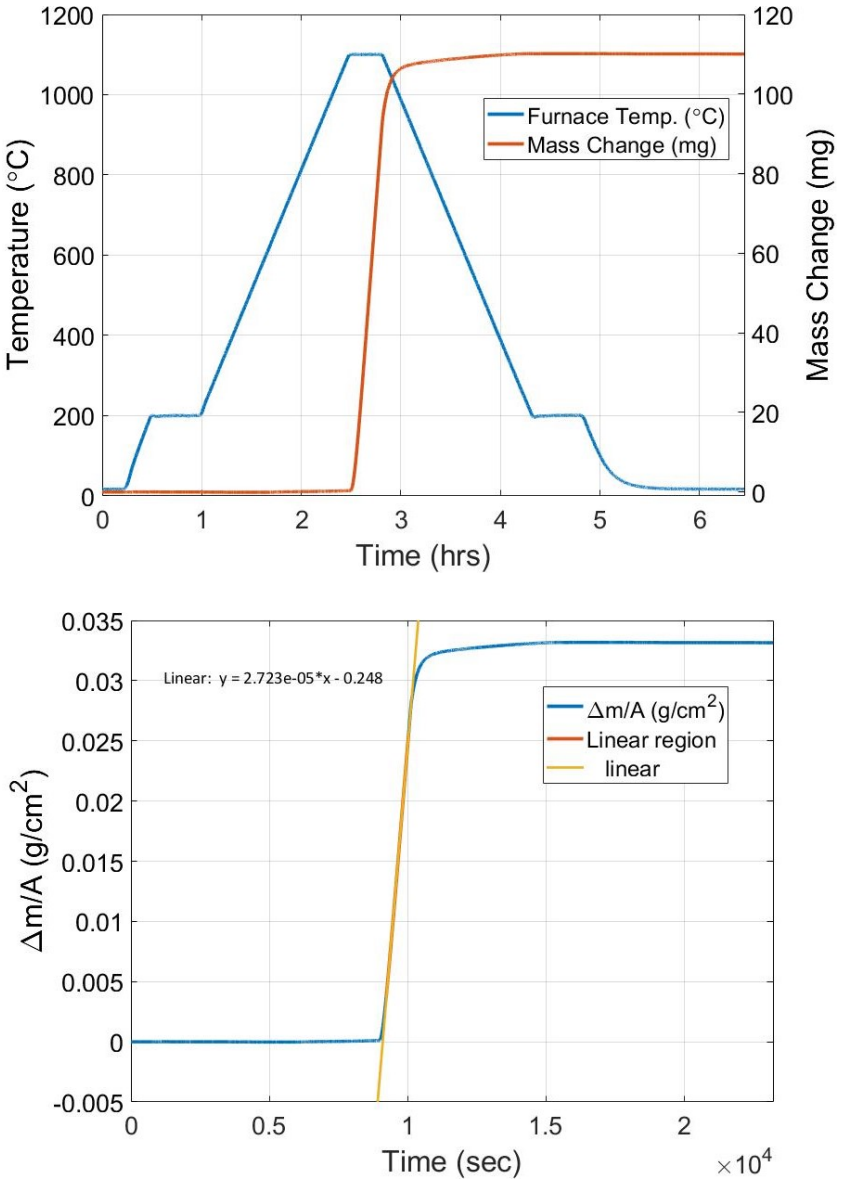

Figure A.5: Results for 200107 Fe-7%Mn alloy oxidised for 20 min in 20%O_2 at 1100 °C

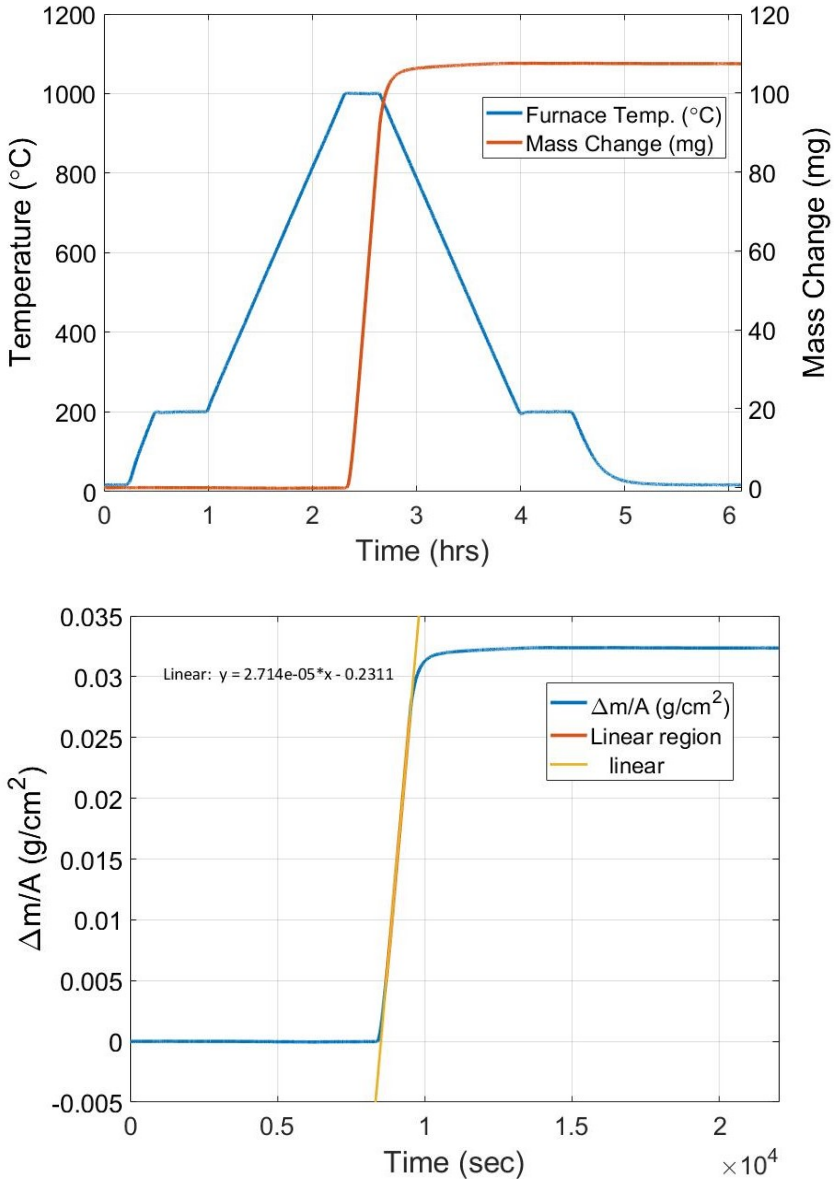

Figure A.6: Results for 200111 Fe-3%Mn alloy oxidised for 20 min in 20%O_2 at 1000 °C

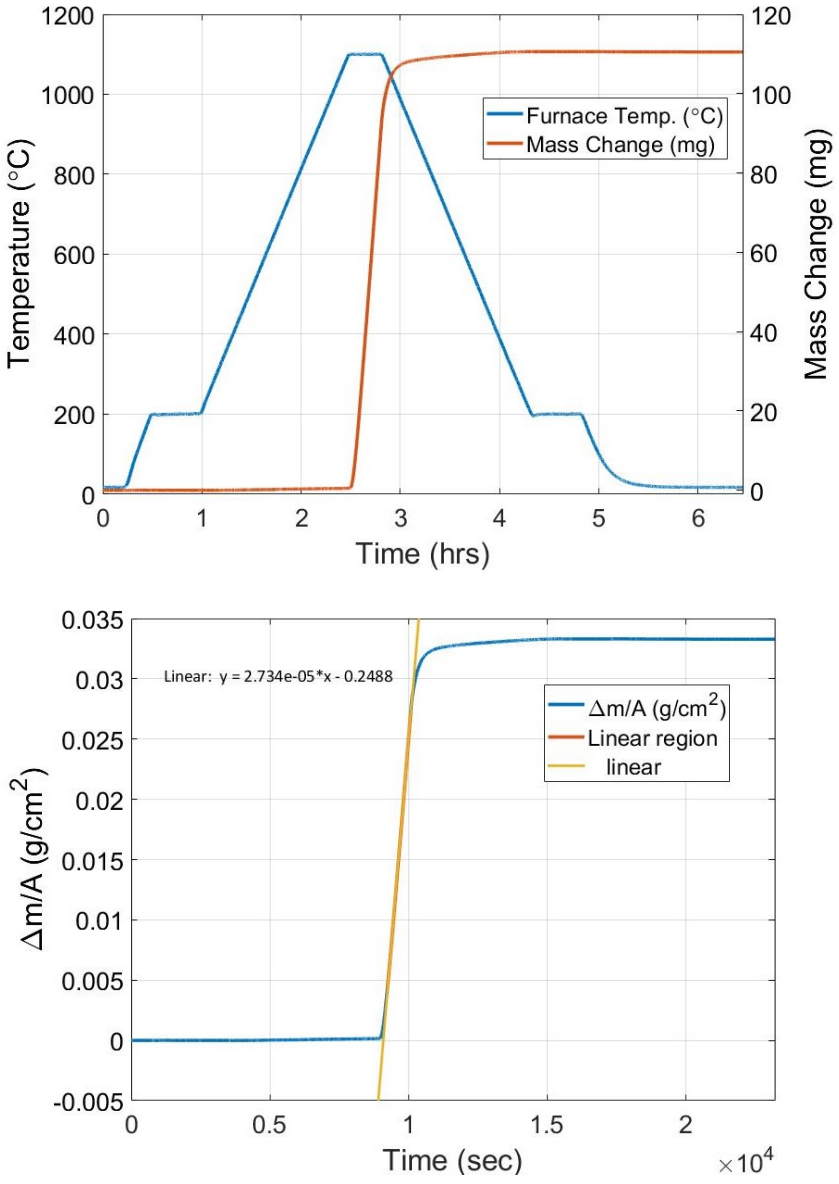

Figure A.7: Results for 200108 Fe-3%Mn alloy oxidised for 20 min in 20%O_2 at 1100 °C

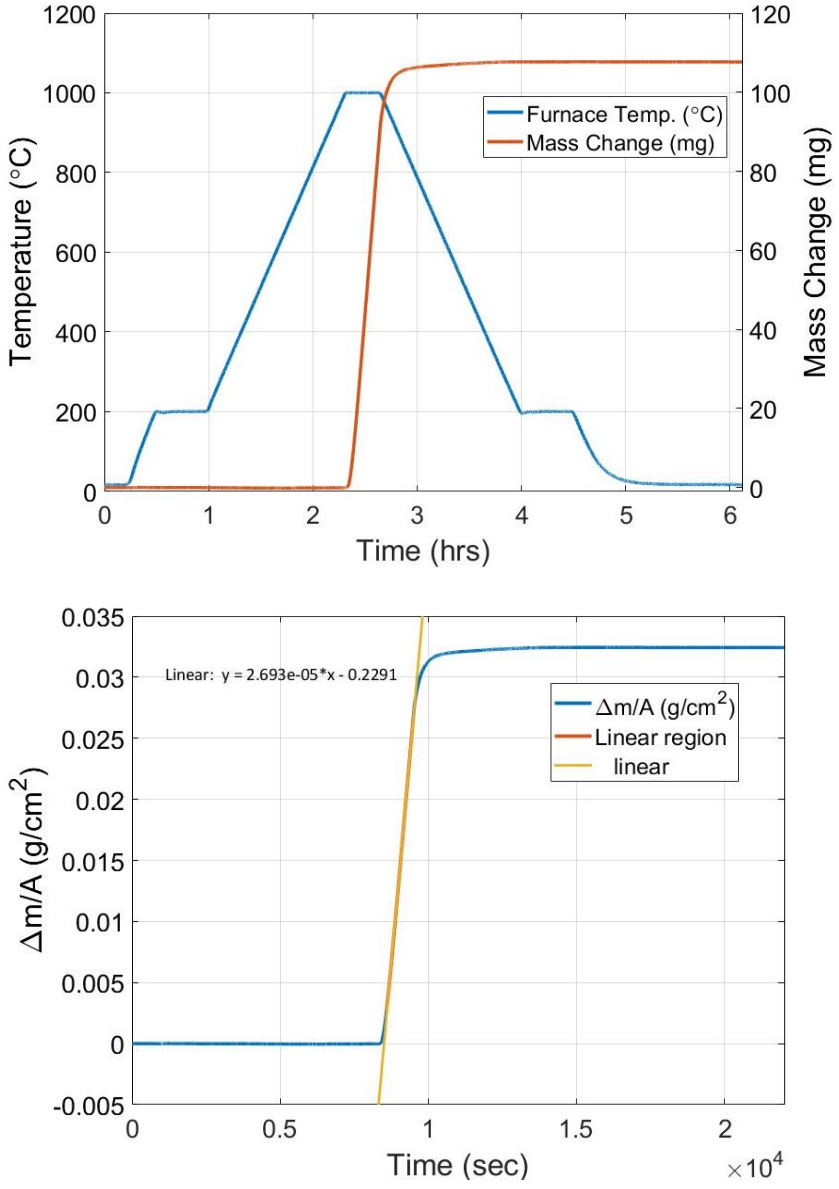

Figure A.8: Results for 200112 Fe-0.5%Mn alloy oxidised for 20 min in 20%O_2 at 1000 °C

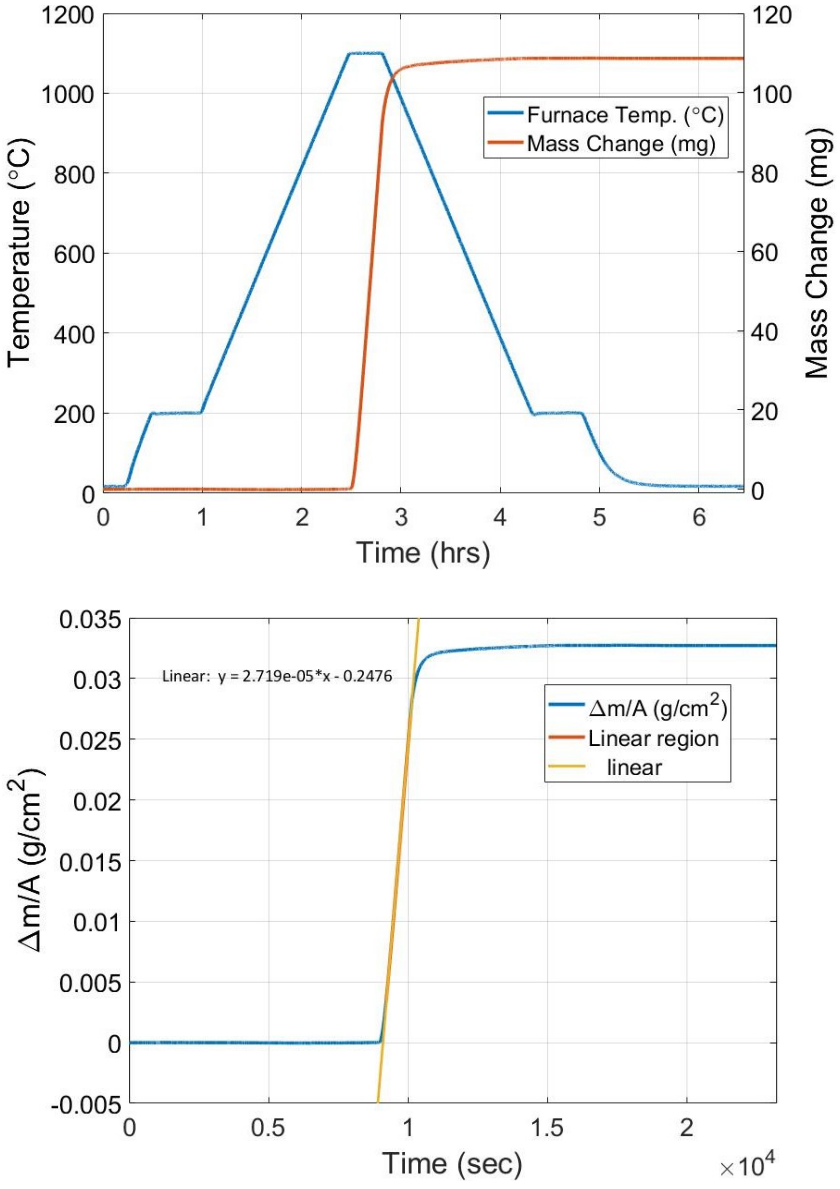

Figure A.9: Results for 200114 Fe-0.5%Mn alloy oxidised for 20 min in 20%O_2 at 1100 °C

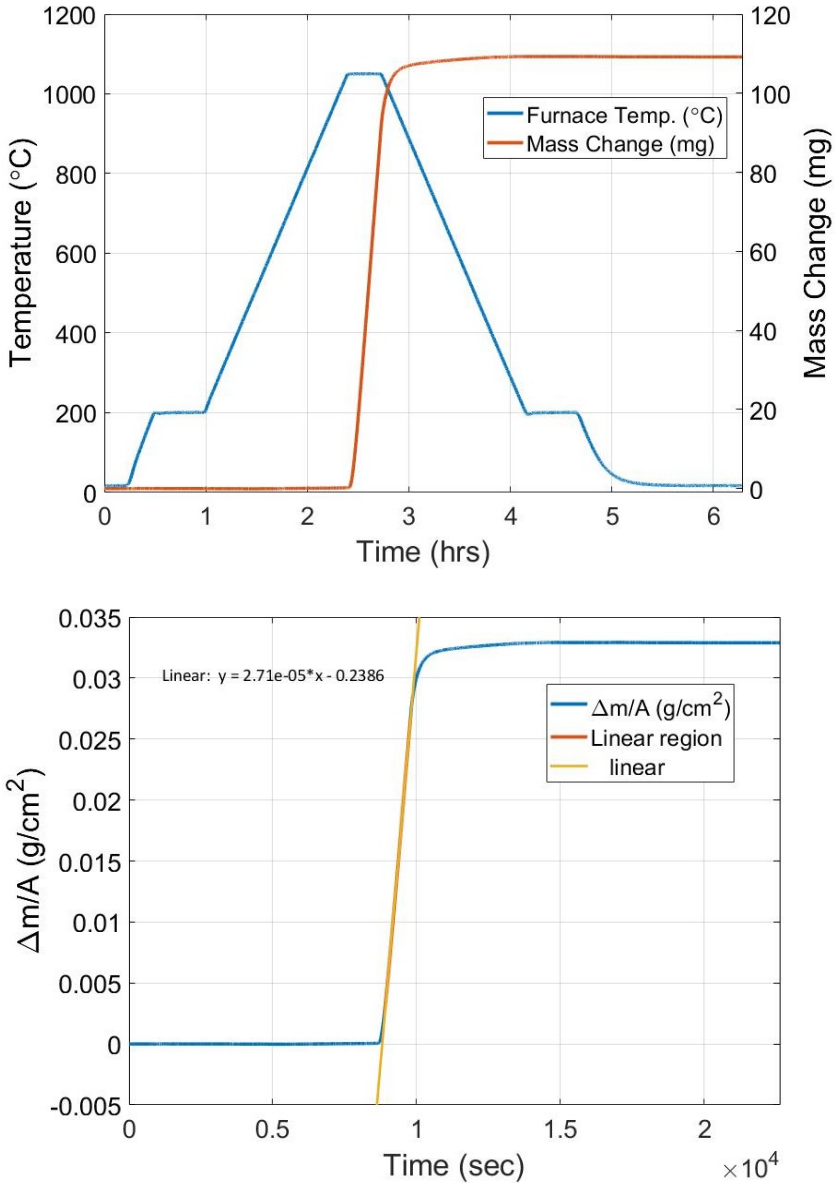

Figure A.10: Results for 200125 Fe-7%Mn alloy oxidised for 20 min in 20%O_2 at 1050 °C

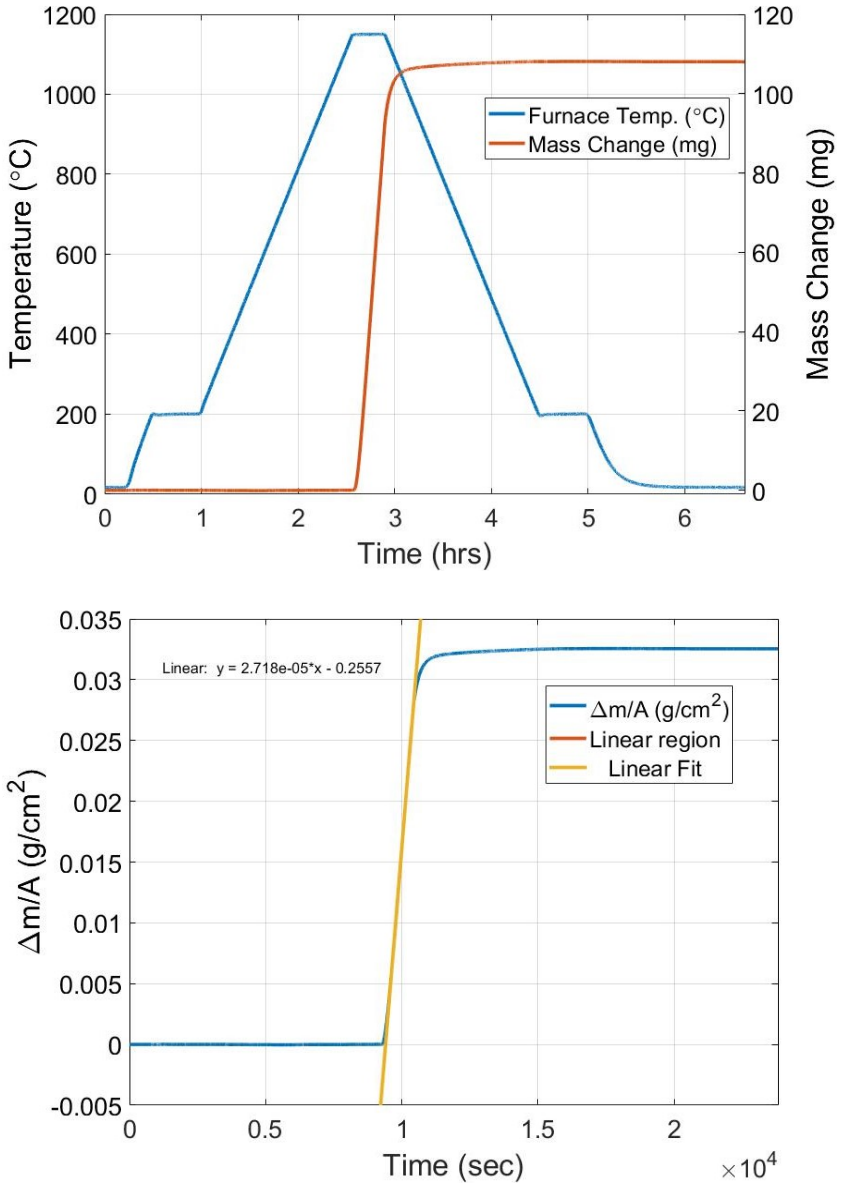

Figure A.11: Results for 200126 Fe-7%Mn alloy oxidised for 20 min in 20%O_2 at 1150 °C

A.2. QMS plots of partial pressure fluctuation

A.2.1. MATLAB code used for analysis and plotting

In order to plot the signals obtained from the Quadrupole Mass Spectrometer (QMS), versions of the following code was used:

```
dataset_17_FeMn=xlsread('#17.xls','210126_FeMn7_20min_1150C_N2,O2_','A2:C14890');
dataset_17_mass_FeMn=xlsread('#17_mass.xlsx','#17','Q20:U16519');
timehrs1=dataset_17_FeMn(:,1);
deltamass=dataset_17_FeMn(:,3);
timehrs2=dataset_17_mass_FeMn(:,1);
O2percent=dataset_17_mass_FeMn(:,5);
figure(1);
hold on;
yyaxis left
p2=plot(timehrs1,deltamass);
xlabel('Time (hrs)');
ylabel('Mass Change (mg)');
%title('210126 Fe-7%Mn Oxidation 20 min. at 1150C (20% O_2)(#17)');
yyaxis right
p1=plot(timehrs2,O2percent);
ylabel('Gas percentage (%)');
xlabel('Time (hrs)');
legend('Mass Change (mg)','O_2%');
legend('Position',[0.65 0.7 0.025 0.07])
grid on
pbaspect([4 3 1])
p1.LineStyle = '-';
p1.LineWidth = 2.75;
p1.Marker = 'none';
p2LineStyle = '-';
p2.LineWidth = 2.75;
p2.Marker = 'none';
ax = gca;
ax.Box = 'on';
ax.FontSize=20;
% ax.XLim = [0 inf];
ax.XLim = [2.4 3.4];
ax.LabelFontSizeMultiplier = 1.2;
ax.GridColor = [0.11 0.11 0.11];
ax.GridLineStyle = '-';
yyaxis left
ax.YLim = [-1 inf];
ax.YColor = 'black';
yyaxis right
ax.YLim = [0 5];
ax.YColor = 'black';
hold off;
```

A.2.2. Figures Obtained

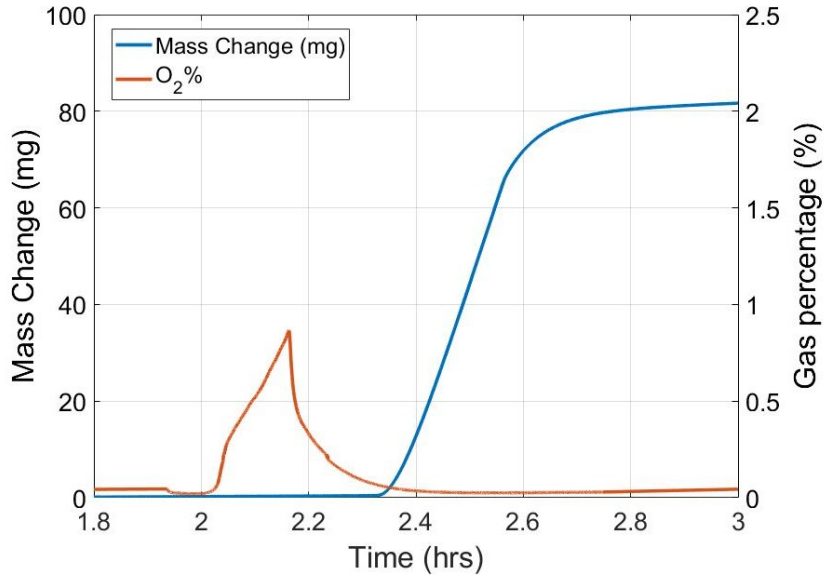

(a) QMS results for 201029 Fe-7%Mn alloy oxidised for 15 min in 20%O_2 at 1000 °C

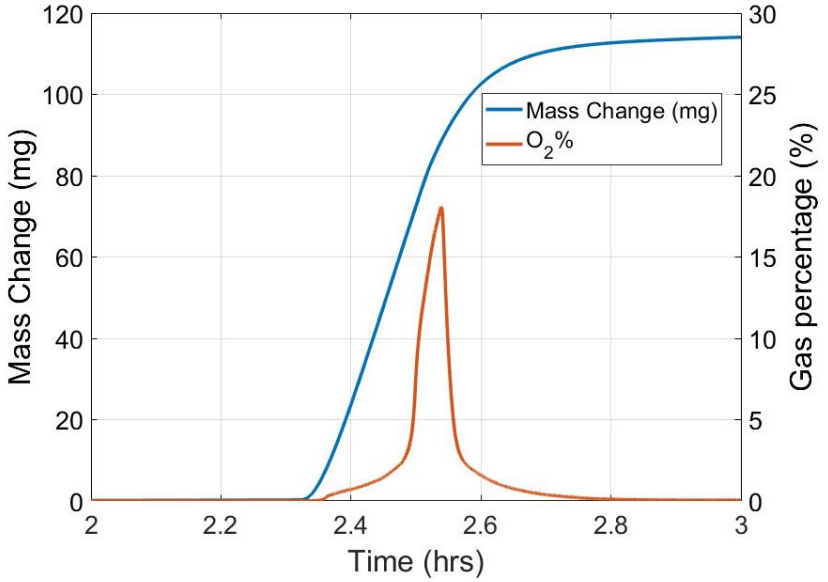

(b) QMS results for 201030 Fe-7%Mn alloy oxidised for 15 min in 30%O_2 1000 °C

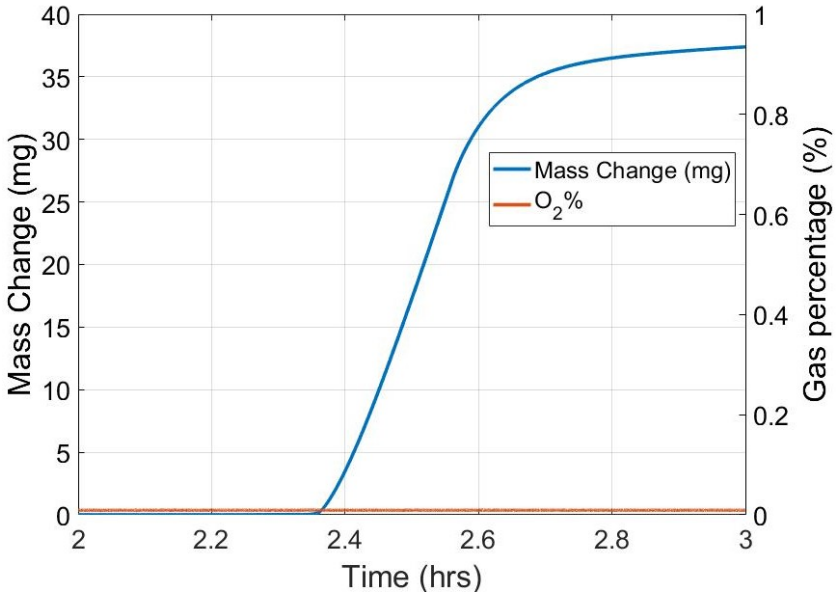

(c) QMS results for 201217 Fe-7%Mn alloy oxidised for 15 min in 10%O_2 at 1000 °C

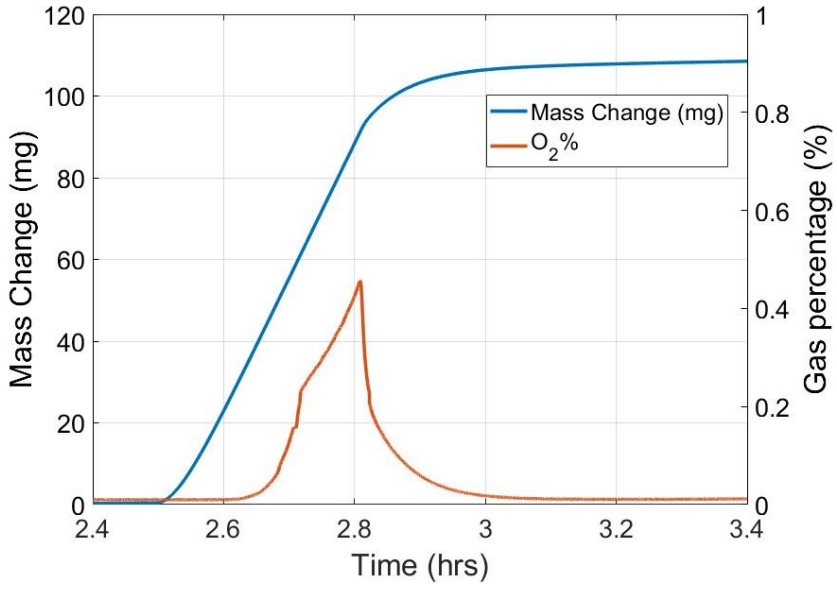

(d) QMS results for 200107 Fe-7%Mn alloy oxidised for 20 min in 20%O_2 at 1100 °C

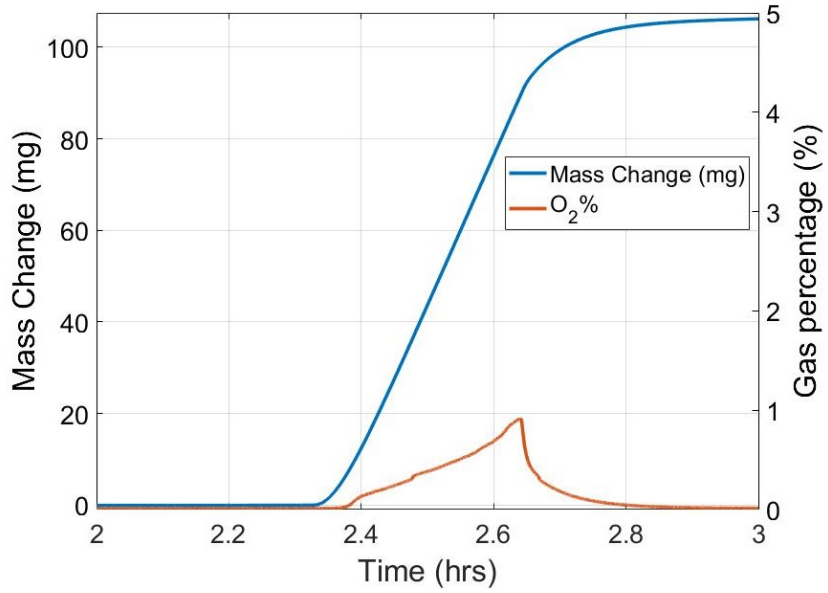

(e) QMS results for 200111 Fe-3%Mn alloy oxidised for 20 min in 20%O_2 at 1000 °C

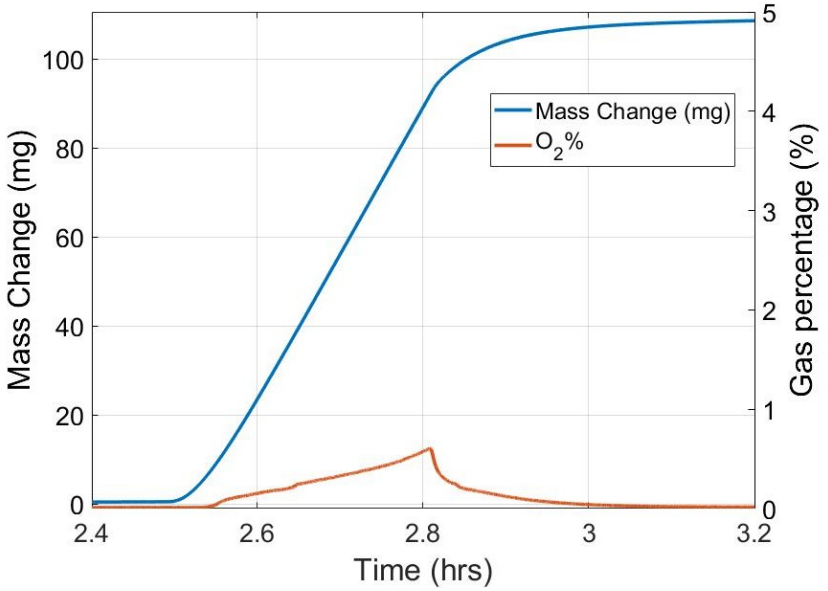

(f) QMS results for 200108 Fe-3%Mn alloy oxidised for 20 min in 20%O_2 at 1100 °C

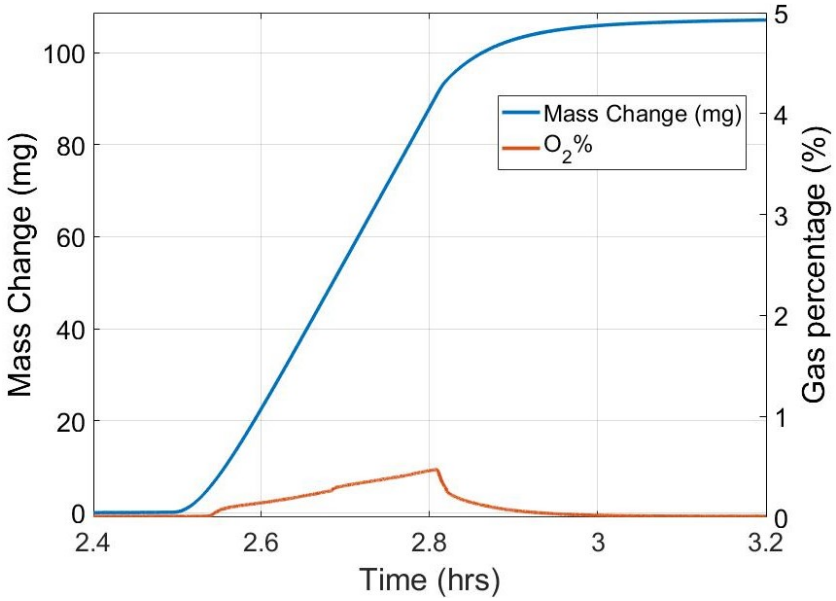

(g) QMS results for 200114 Fe-0.5%Mn alloy oxidised for 20 min in 20%O_2 at 1100 °C

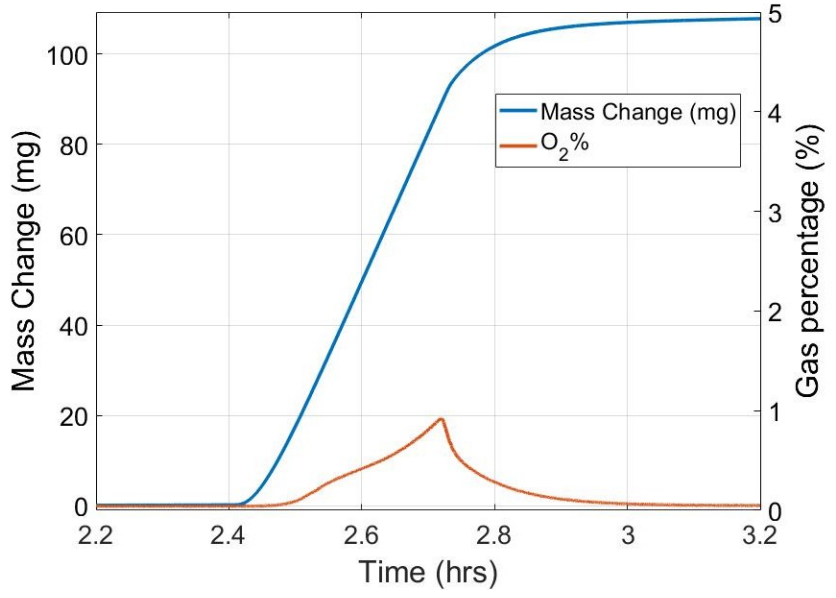

(h) QMS results for 200125 Fe-7%Mn alloy oxidised for 20 min in 20%O_2 at 1050 °C

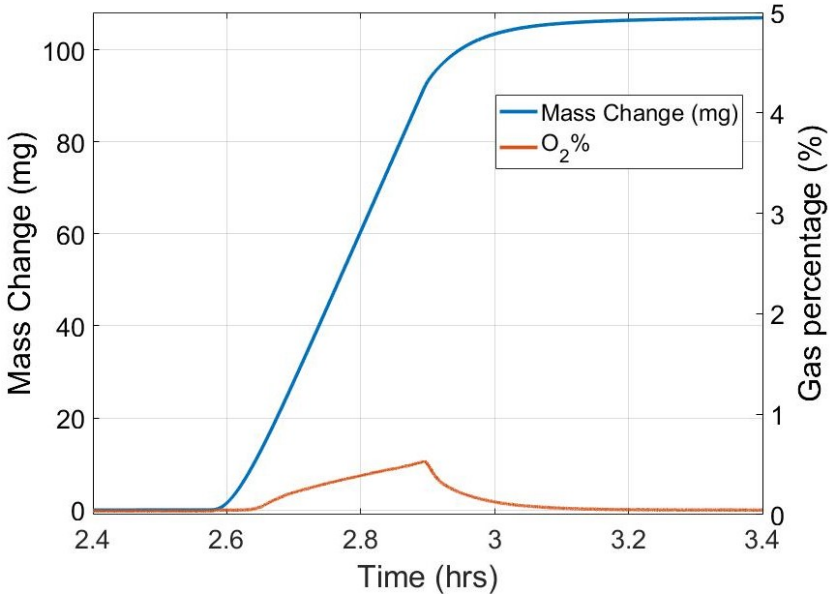

(i) QMS results for 200126 Fe-7%Mn alloy oxidised for 20 min in 20%O_2 at 1150 °C

A.3. Optical Microscopy

A.3.1. Images Obtained

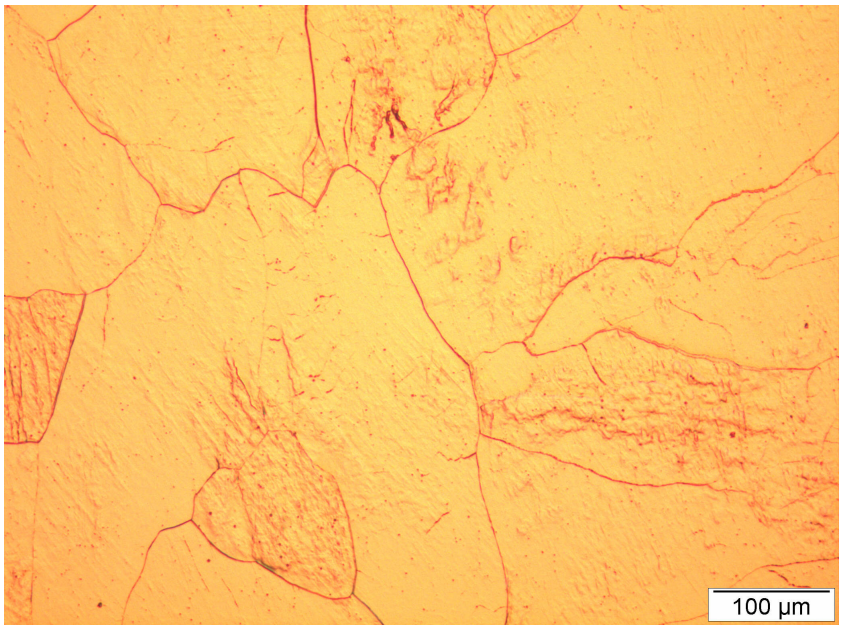

(a)

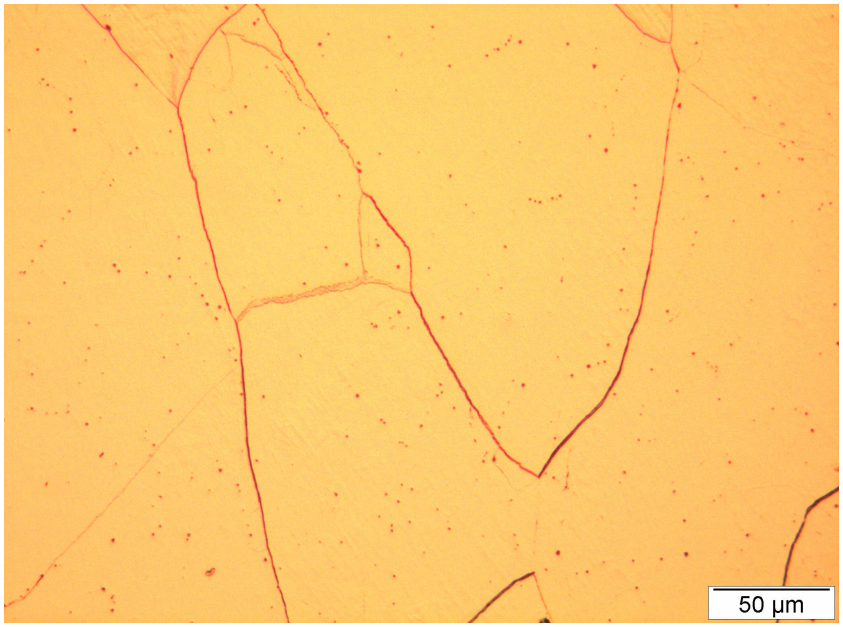

(b)

Figure A.13: Images showing the grains of (a) & (b) Fe-0.5%Mn at two different magnifications

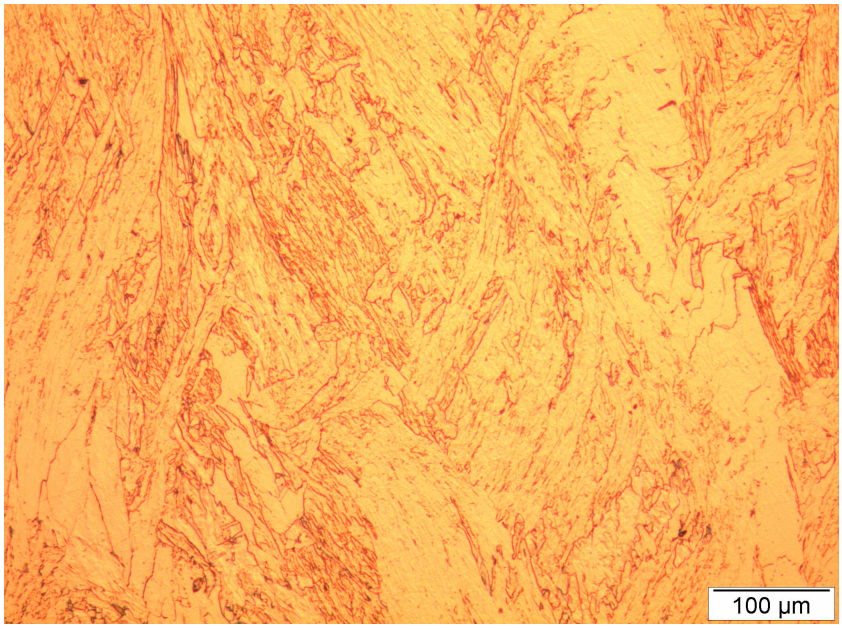

(c)

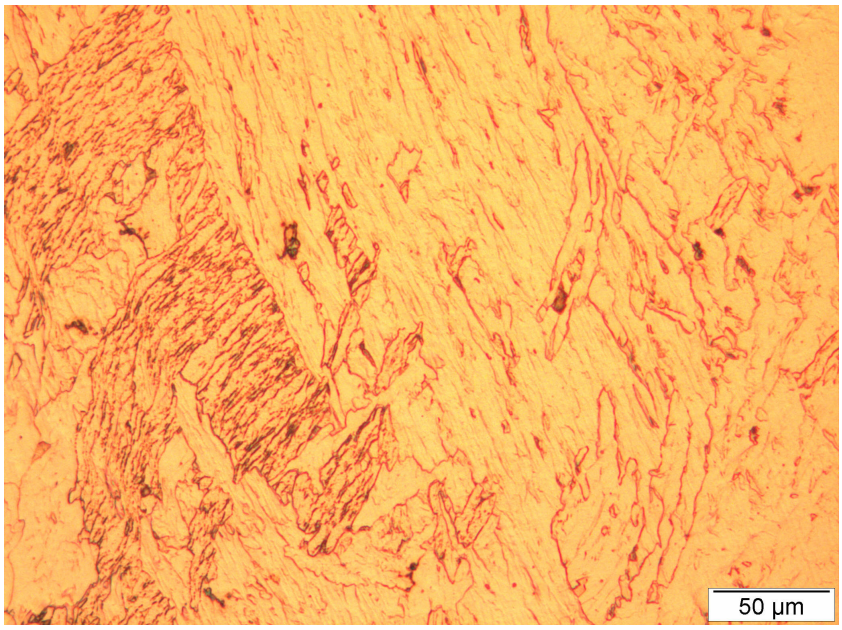

(d)

Figure A.13: Images showing the grains of (c) & (d) Fe-7%Mn at two different magnifications

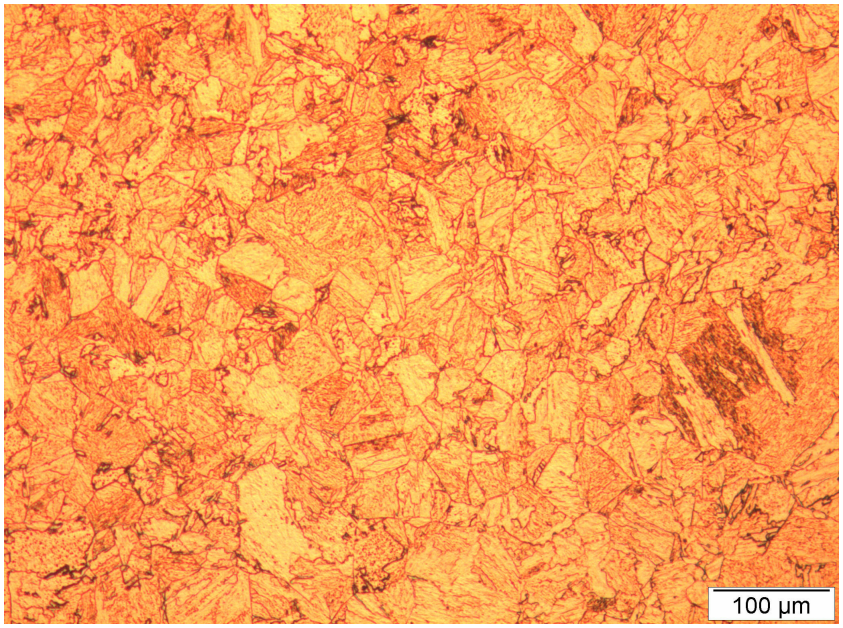

(e)

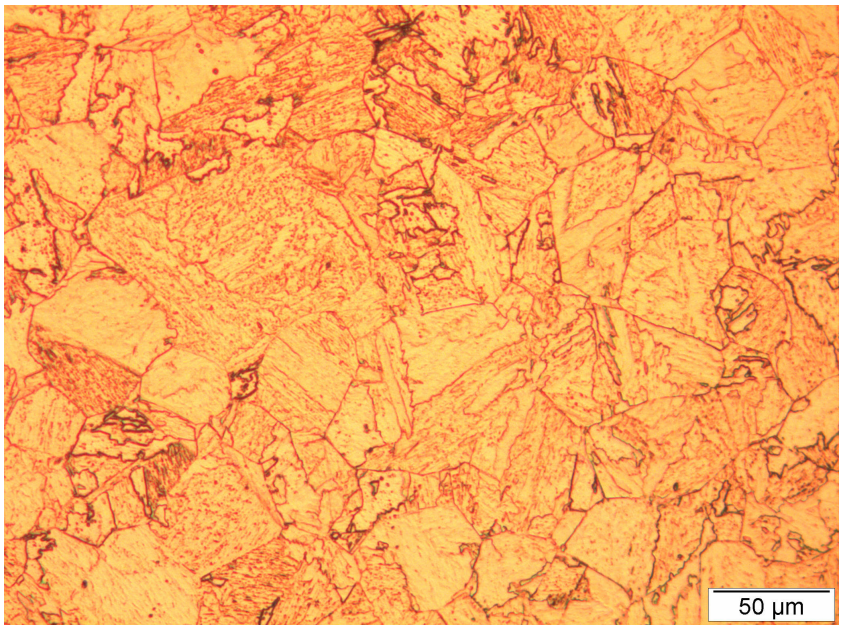

(f)

Figure A.13: Images showing the grains of (e) & (f) Fe-7%Mn at two different magnifications

A.3.2. Grain Size Calculation

Table A.1: Data from ImageJ for calculation of Fe-0.5%Mn grain size

	Area	Mean	Min	Max	Angle	Length	No. of Intercepts	Mean Intercept Length (mm)
1	3.18E-04	185.03	107.05	201.90	36.46	0.91	9.00	0.10
2	3.17E-04	187.43	0.00	254.96	-36.40	0.90	4.50	0.20
3	1.90E-04	180.02	0.00	255.00	-90.45	0.54	3.50	0.15
4	2.56E-04	179.47	0.00	255.00	0.08	0.73	5.00	0.15
							Sum =	0.60
							Avg. =	0.15

Table A.2: Data from ImageJ for calculation of Fe-3%Mn grain size

	Area	Mean	Min	Max	Angle	Length	No. of Intercepts	Mean Intercept Length (mm)
1	7.96E-05	174.46	92.21	198.93	36.55	0.45	11.50	0.04
2	7.95E-05	177.35	0.00	254.75	-36.59	0.45	11.00	0.04
3	4.75E-05	171.39	0.00	194.08	-89.44	0.27	6.00	0.05
4	6.39E-05	182.39	0.00	254.89	0.66	0.36	5.00	0.07
							Sum =	0.20
							Avg. =	0.05

Table A.3: Data from ImageJ for calculation of Fe-7%Mn grain size

	Area	Mean	Min	Max	Angle	Length	No. of Intercepts	Mean Intercept Length (mm)
1	7.61E-05	168.90	81.94	198.83	36.52	0.44	15.00	0.03
2	7.63E-05	172.15	0.00	254.93	-36.61	0.44	14.50	0.03
3	4.54E-05	166.34	77.99	196.00	-89.66	0.26	10.00	0.03
4	6.12E-05	166.59	47.03	199.40	0.50	0.36	11.50	0.03
							Sum =	0.12
							Avg. =	0.03

A.4. HT-XRD scans

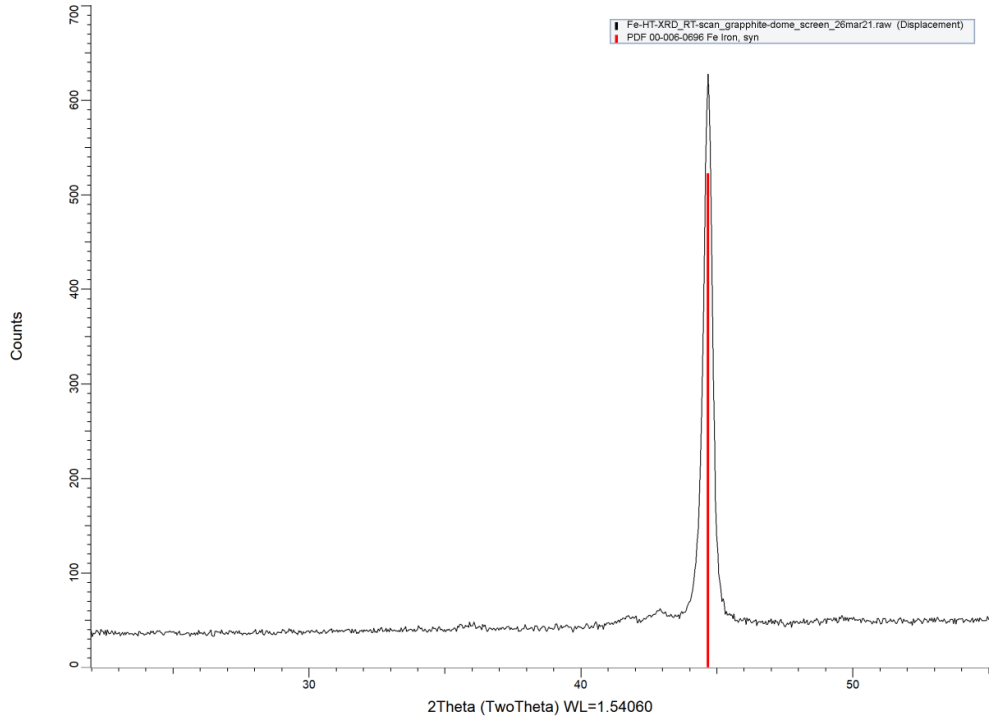

(a)

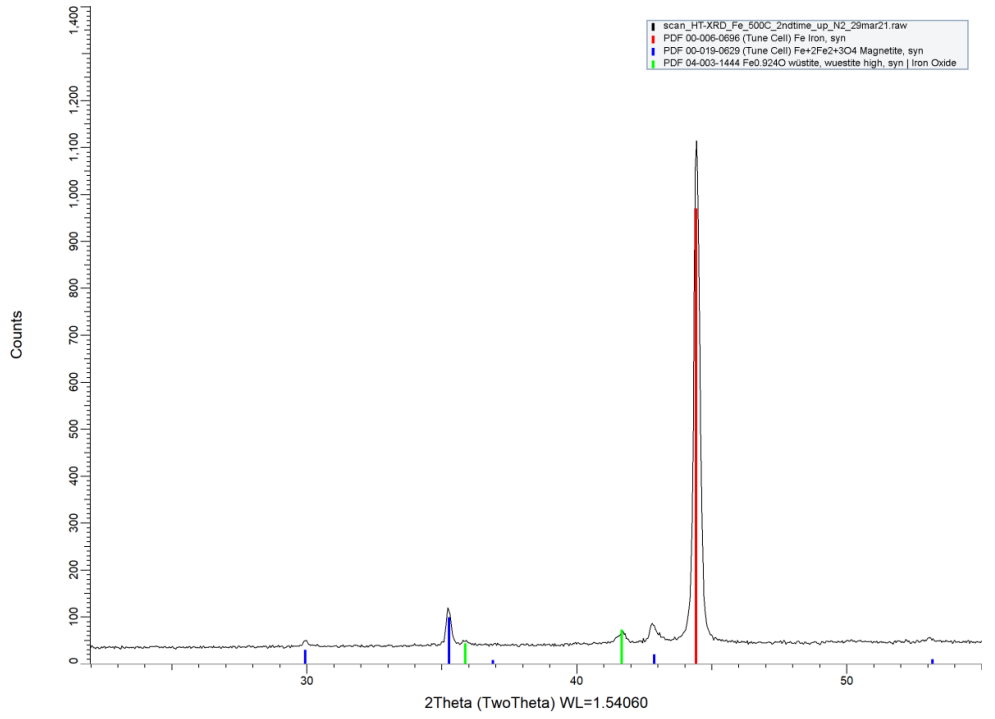

(b)

Figure A.14: XRD pattern for the Fe-3%Mn sample during the heating regime at (a) Room Temperature (b)500 °C [25]

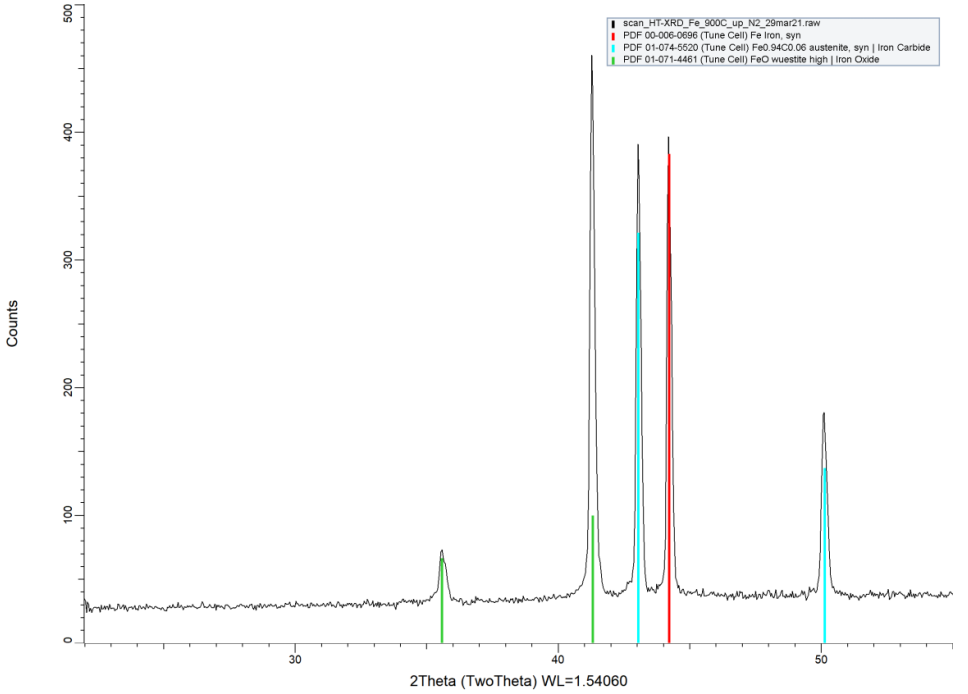

(c)

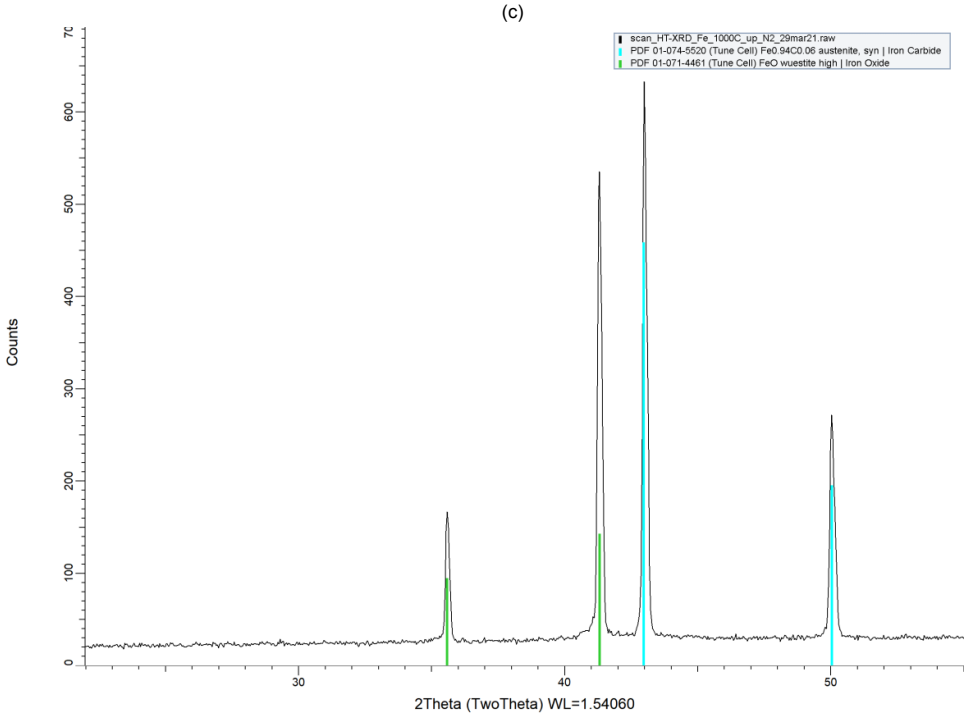

(d)

Figure A.14: XRD pattern for the Fe-3%Mn sample during the heating regime at (a)900 °C and (b)1000 °C [25]

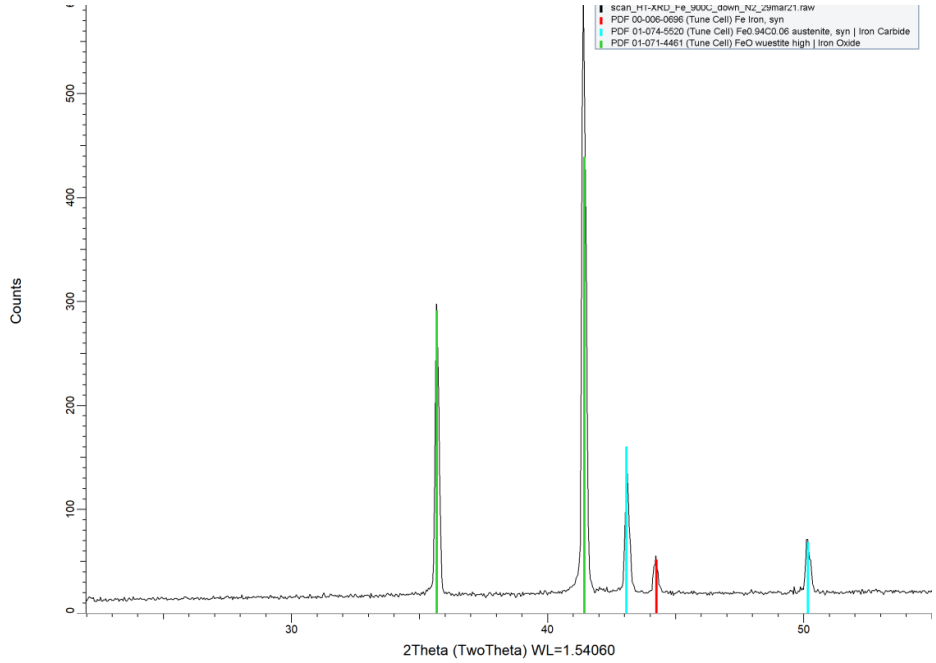

(e)

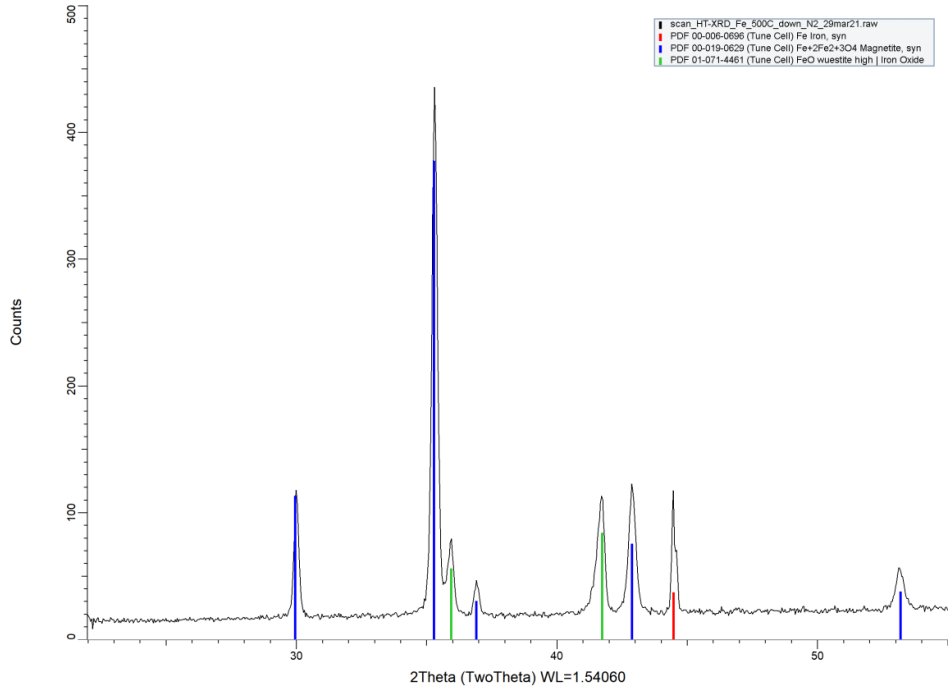

(f)

Figure A.14: XRD pattern for the Fe-3%Mn sample during the cooling regime at (a)900 °C and (b)500 °C [25]

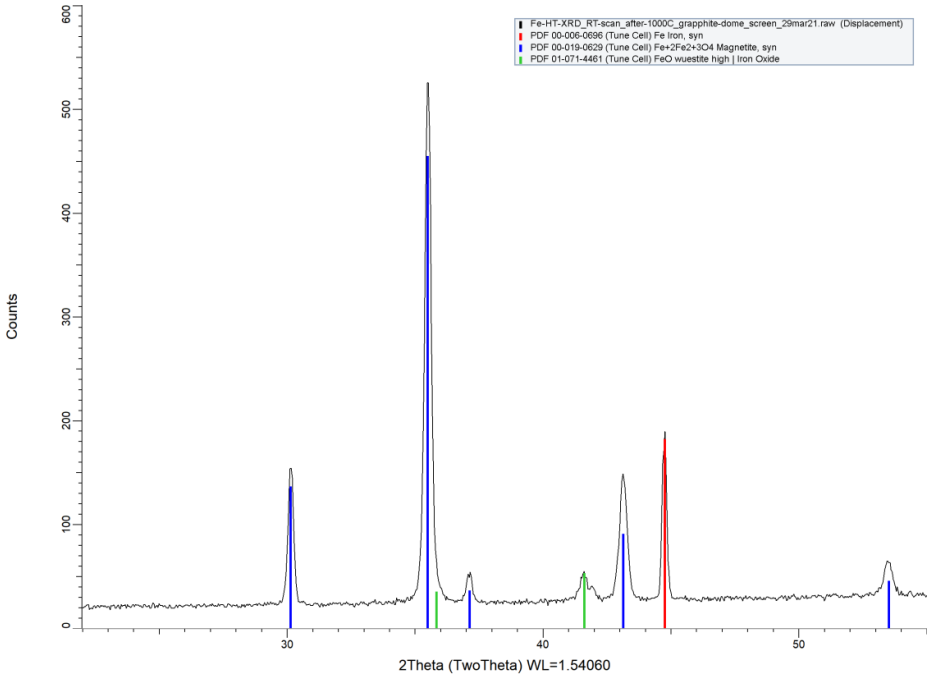

Figure A.14: XRD pattern for the Fe-3%Mn sample after the cooling regime at Room Temperature [25]

A.5. Transition from Linear to Parabolic Rate

According to [14], for deriving the equations required for the calculation of the time taken to transition from linear to parabolic rate of oxidation, some assumptions have been made as follows:

- The reaction surface is considered to be smooth and the gas is moving in direction and parallel to the surface of the sample being oxidised, where x is the distance from the leading edge downstream of the gas flow.
- The gas flow is considered as laminar, and forms a steady hydrodynamic boundary layer over the surface of the sample.
- The length and width of the sample are assumed to be much larger than the thickness of the hydrodynamic boundary layer and therefore, the space above the surface of the sample, where the gas transfer takes place, is regarded as semi-infinite.

In order to calculate the local transition time for linear-to-parabolic rate, the following quantities are required. From [14], the theoretical parabolic rate constant can be calculated as:

$$k_{P,x} = M_o f_o \rho k_{r,x} = 16 f_o \rho k_{r,x} \tag{A.1}$$

where M_o = molecular weight of O_2
f_o = weight fraction of oxygen in wustite
ρ = density of wustite (5.7 gm/cm^3)

In order to find $k_{r,x}$, The following equation is used, (also from [14]):

$$k_{r,x} = \frac{1}{1-y} C_{\mathrm{O(FeO)}} D_{\mathrm{Fe(FeO)}} \ln\left[\frac{P''_{\mathrm{O_2}}}{P'_{\mathrm{O_2}}}\right] = \frac{1}{1-y} C_{\mathrm{O(FeO)}} D_{\mathrm{Fe(FeO)}} \left(\frac{\Delta G''^{\circ}_T - \Delta G'^{\circ}_T}{RT}\right) \tag{A.2}$$

where (1 - y) = average Fe:O ratio in wustite ($Fe_{1-y}O$)
$P'_{\mathrm{O_2}}$, $P''_{\mathrm{O_2}}$ = the oxygen partial pressures at the steel–wustite and wustite–magnetite interfaces, respectively
$C_{\mathrm{O(FeO)}}$ = average oxygen concentration in $mole(O)/cm^3$ across the wustite layer
$D_{\mathrm{Fe(FeO)}}$ = self diffusion coefficient of iron in wustite in cm^2/s

The free energies of formation can be calculated from the equations of formation of wustite and magnetite:

$$\begin{aligned} 2\mathrm{Fe} + \mathrm{O_2} = 2\mathrm{FeO} \quad \Delta G'^{\circ}_T = RT \ln P'_{\mathrm{O_2}} = -528,630 + 130.8T(\ \mathrm{J/mol}) \\ 6\mathrm{FeO} + \mathrm{O_2} = 2\mathrm{Fe_3O_4} \quad \Delta G''^{\circ}_T = RT \ln P''_{\mathrm{O_2}} = -624,840 + 250.4T(\ \mathrm{J/mol}) \end{aligned} \tag{A.3}$$

Assuming a non-stoichiometric wustite composition of $Fe_{0.907}O$, since the XRD data available has identified a wustite phase of composition $Fe_{0.92}O$ in some of the oxidised samples, the coefficient of self-diffusion $D_{\mathrm{Fe(FeO)}}$ is given from equation: (25) in Chen and Yuen [14]:

$$D_{\mathrm{Fe(FeO)}} = 0.0118 \exp\left(\frac{-124,350}{RT}\right) \tag{A.4}$$

where R = gas constant in J/K
T = temperature in K

The time taken for transition from a linear to a parabolic rate is then given from equation: (34) in Chen and Yuen [14]:

$$t_{x,\ \text{transition}} = \frac{W_{x,\ \text{transition}}}{k_{l,x}} = \frac{a \cdot x^{1/2}}{\left[b/x^{1/2}\right]} = \frac{a \cdot x}{b}\ . \tag{A.5}$$

where,

$$a = \frac{k_{P,x}}{2b} \tag{A.6}$$

and,

$$b = \frac{1}{3} M_{O_2} \left(\frac{D^4}{\nu} \right)^{1/6} u^{1/2} C_0 \tag{A.7}$$

where $W_{x,\text{ transition}}$ = transition thickness (cm)
$k_{l,x}$ = local linear rate constant (theoretical) (g/cm^{2}sec)
$k_{P,x}$ = local parabolic rate constant (theoretical) (g^2/cm^{4}sec)
D = diffusion coefficient of O_2 in binary gas mixture (cm^2/sec)
ν = viscosity of binary gas mixture (cm^2/sec)
u = gas velocity (cm/s)
C_0 = concentration of O_2 (moles/cm^3)

Further on, a list of the parameters and constants used for this calculation can be found in Table A.4. The values of most of the quantities are available in literature, however the following were derived:

- The weight fraction of atomic oxygen in wustite (f_o): The composition of wustite was assumed to be $Fe_{0.907}O$ as this is the composition used for deriving the self-diffusion coefficient of iron in wustite. The f_o was therefore calculated as $\frac{16}{0.907 \times 55.85 + 16} = 0.24$.
- The average oxygen concentration in $mole(O)/cm^3$ across the wustite layer ($C_{O(FeO)}$): This has been calculate by (for 1 mole of wustite):

$$\frac{Mol.\,wt.\,of\ atomic\ oxygen}{\frac{Mol.\,wt.\,of\ wustite}{Density\ of\ wustite}} = \frac{16}{\frac{0.907 \times 55.85 + 16}{5.7}} = 0.085 \tag{A.8}$$

While in Chen and Yuen [13] different values of $C_{O(FeO)}$ with respect to temperature of oxidation have been listed, there is only 1-2% difference in value of $C_{O(FeO)}$ for the temperature range of 1000-1150°C, so it has been assumed to be a constant value of 0.085.

Table A.4: Table showing the parameters used for the calculation of the $t_{trans.}$

Quantity	Value	Unit
R	8.314	J/K
Molecular Weight (Fe)	55.85	gm/mol
f_o (wustite)	0.24	
Density (wustite)	5.7	gm/cc
$C_{O(FeO)}$	0.085	mol/cc

In order to obtain the maximum transition time, i.e. the time interval beyond which the parabolic rate law is followed, the 'x' can be substituted by L = the length of the sample. By this evaluation, it seems that the time taken for transition from linear to parabolic rate is in the range of a few hours. From the data available, it is observed that there is a dependence of the transition time on the O_2 vol% (see figure: A.15), and the transition time seems to be very sensitive to changes in the oxygen concentration of the oxidising atmosphere. At lower oxygen levels it is possible that the critical thickness required for diffusion of Fe cations to be the rate determining mechanism takes longer to be achieved, and so the transition time is longer.

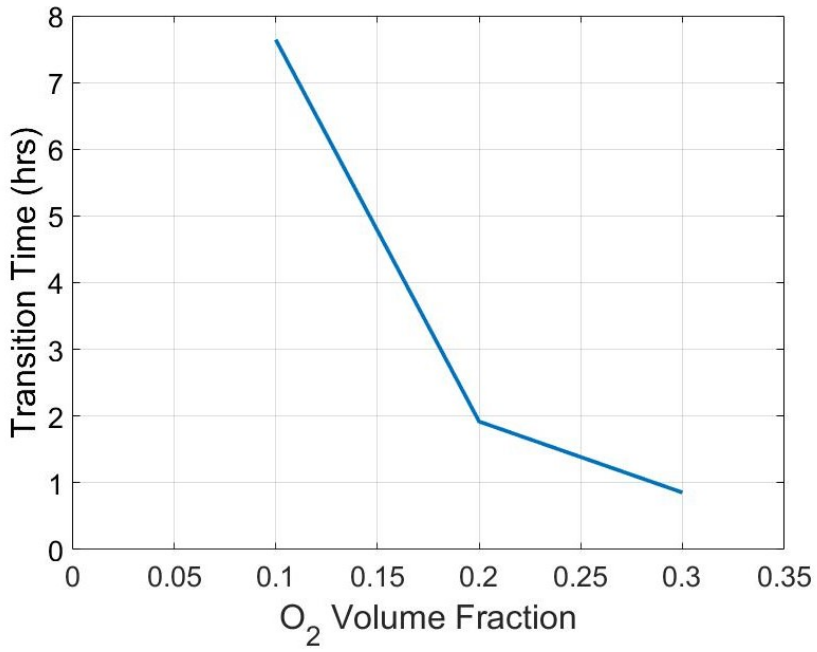

Figure A.15: Figure showing the dependence of Transition Time on O_2 vol% in the furnace chamber for Fe-7%Mn at 1000 °C

Table A.5: Comparison of experimental and theoretical linear rate constants alongside the transition time from linear to parabolc rate for Fe-Mn alloys

S. No.	Oxidation Time t min.	Oxidation Temperature T °C	Oxygen Mole Fraction X_{O_2}	Experimental Rate Constant $k_{l_{exp.}}$ $(g/cm^2 sec)$	Theoretical Rate Constant $k_{l_{theor.}}$ $(g/cm^2 sec)$	% Difference	Max. Transition Time $t_{trans.}$ min.
Fe-7%Mn							
1	15	1000	0.2	2.698×10^{-5}	3.43453×10^{-5}	27.299	115.094
2	15	1000	0.3	3.983×10^{-5}	5.14694×10^{-5}	29.223	51.25
3	15	1000	0.2	2.632×10^{-5}	3.43453×10^{-5}	30.491	115.094
4	15	1000	0.1	1.233×10^{-5}	1.72071×10^{-5}	39.55	458.538
5	20	1100	0.2	2.715×10^{-5}	3.39521×10^{-5}	25.05	117.78
6	20	1050	0.2	2.752×10^{-5}	3.39656×10^{-5}	23.42	117.68
7	20	1150	0.2	2.718×10^{-5}	3.37595×10^{-5}	24.21	119.12
Fe-3%Mn							
8	20	1000	0.2	2.714×10^{-5}	3.43453×10^{-5}	26.55	115.094
9	20	1100	0.2	2.724×10^{-5}	3.39521×10^{-5}	24.64	117.78
Fe-0.5%Mn							
10	20	1000	0.2	2.693×10^{-5}	3.43453×10^{-5}	27.53	115.094
11	20	1100	0.2	2.719×10^{-5}	3.39521×10^{-5}	24.87	117.78

Bibliography

[1] Soroush Aghaeian. *Phase diagram showing possible oxide formation in Fe-Mn binary with respect to oxygen partial pressure*.

[2] Z. Basinski, W. Hume-Rothery, and A. Sutton. “The Lattice Expansion of Iron”. In: *Proceedings of the Royal Society of London. Series A, Mathematical and Physical Sciences* 229 (1179 1955), pp. 459–467. URL: http://www.jstor.org/stable/99693.

[3] H. K. D. H. Bhadeshia and R. W. K. Honeycombe. “Chapter 2: Strengthening of Iron and its Alloys”. In: *Steels: Microstructure and Properties*. 2017, pp. 23–59.

[4] H. K. D. H. Bhadeshia and R. W. K. Honeycombe. “Chapter 4: Solutes that substitute for Iron”. In: *Steels: Microstructure and Properties*. 2017, pp. 101–133.

[5] Neil Birks. *Introduction to the High-Temperature Oxidation of Metals. Chapter 2: Thermodynamic Fundamentals*. Cambridge University Press, 2006, pp. 16–38.

[6] Neil Birks. *Introduction to the High-Temperature Oxidation of Metals. Chapter 1: Methods of Investigation*. Cambridge University Press, 2006, pp. 1–15.

[7] Neil Birks. *Introduction to the High-Temperature Oxidation of Metals. Chapter 3: Mechanisms of Oxidation*. Cambridge University Press, 2006, pp. 39–72.

[8] P. Henk Bolt. “Understanding the Properties of Oxide Scales on Hot Rolled Steel Strip”. In: *Steel Research International* 75 (6 2004), pp. 399–404. DOI: https://doi-org.tudelft.idm.oclc.org/10.1002/srin.200405786.

[9] David Brandon and Wayne D. Kaplan. *Microstructural Characterization of Materials*. 2008. Chap. Diffraction Analysis of Crystal Structure, pp. 55–65.

[10] R. Bredesen and P. Kofstad. “On the oxidation of iron in $CO_2 + CO$ gas mixtures: I. Scale morphology and reaction kinetics”. In: *Oxidation of Metals* 34 (1990).

[11] D. Bruce and P. Hancock. “Note on the Temperature Stability of Wüstite in Surface Oxide Films on iron”. In: *British Corrosion Journal* 4 (1969), pp. 221–222. DOI: https://doi-org.tudelft.idm.oclc.org/10.1179/000705969798325361.

[12] R.Y. Chen and W.Y.D. Yuen. “A Study of the Scale Structure of Hot-Rolled Steel Strip by Simulated Coiling and Cooling”. In: *Oxidation of Metals* 53 (2000), pp. 539–560. URL: https://doi.org/10.1023/A:1004637127231.

[13] Rex Y. Chen and W. Y. D. Yuen. “Short-Time Oxidation Behavior of Low-Carbon, Low-Silicon Steel in Air at 850–1180 °C: II. Linear to Parabolic Transition Determined Using Existing Gas-Phase Transport and Solid-Phase Diffusion Theories.” In: *Oxidation of Metals 73* (2010), pp. 353–373. DOI: https://doi.org/10.1007/s11085-009-9180-z.

[14] Rex Y. Chen and W. Y. D. Yuen. “Short-Time Oxidation Behavior of Low-Carbon, Low-Silicon Steel in Air at 850–1180 °C: III. Mixed Linear-and-Parabolic to Parabolic Transition Determined Using Local Mass-Transport Theories”. In: *Oxidation of Metals 74* (2010), pp. 255–274. DOI: https://doi.org/10.1007/s11085-010-9212-8.

[15] R. M. Cornell and U. Schwertmann. *The Iron Oxides: Structure, Properties, Reactions, Occurences and Uses. Chapter 2: Crystal Structure*. 2003, pp. 9–38. DOI: 10.1002/3527602097.

[16] B.D. Cullity. *Elements of X-ray diffraction. Chapter 3: Diffraction I: The Directions of Diffracted Beams*. 1977, pp. 78–96.

[17] M. Danielewski. *Corrosion: Fundamentals, Testing, and Protection. Kinetics of Gaseous Corrosion Processes*. Vol. 13A. ASM International, 2003, pp. 97–105.

[18] M. H. Davies, M. T. Simnad, and C. E. Birchenall. “On the Mechanism and Kinetics of the Scaling of Iron”. In: *Journal of Metals* 3 (1951), pp. 889–896. URL: https://doi-org.tudelft.idm.oclc.org/10.1007/BF03397397.

[19] E. P. Degarmo. “Bulk Forming Processes”. In: *Materials and Processes in Manufacturing*. Wiley, 2007, p. 382.

[20] E. N. Fuller, P. D. Schettler, and J. C. Giddings. “NEW METHOD FOR PREDICTION OF BINARY GAS-PHASE DIFFUSION COEFFICIENTS”. In: *Industrial and Engineering Chemistry* 58 (1966), pp. 18–27. DOI: https://doi-org.tudelft.idm.oclc.org/10.1021/ie50677a007.

[21] F. Gesmundo and F. Viani. “Transition from Internal to External Oxidation for Binary Alloys in the Presence of an Outer Scale”. In: *Oxidation of Metals* 25 (1986), pp. 269–282.

[22] R. I. L. Guthrie, H. Abuluwefa, and F. Ajersch. “The Effect of Oxygen Concentration on the Oxidation of Low-Carbon Steel in the Temperature Range 1000 to 1250 °C”. In: *Oxidation of Metals* 46 (1996).

[23] Ruud Hendrikx and Soroush Aghaeian. *XRD identification of an oxide layer*. Feb. 2021.

[24] Ruud Hendrikx and Soroush Aghaeian. *XRD identification of Fe,Mn oxide layers*. Nov. 2020.

[25] Ruud Hendrikx and Anjana Suresh. *2D HT XRD measurement of oxidation of austenite phase in iron*. Mar. 2021.

[26] ASTM International. *Standard Test Methods for Determining Average Grain Size*. Vol. E112-13. 2023. DOI: https://doi-org.tudelft.idm.oclc.org/10.1520/E0112-13.

[27] P. R. S. Jackson and G. R. Wallwork. “The Oxidation of Binary Iron-Manganese Alloys”. In: *Oxidation of Metals* 20 (1983).

[28] V. A. Lashgari. “Internal and External Oxidation of Manganese in Advanced High Strength Steels”. PhD thesis. TU Delft, 2014.

[29] V. A. Lashgari et al. “Kinetics of Internal Oxidation of Mn-Steel Alloys”. In: *Oxidation of Metals* 82 (2014), pp. 249–269.

[30] Chun-Ming Li, Ferdinand Sommer, and Eric J. Mittemeijer. “Characteristics of the $\gamma \rightarrow \alpha$ transformation in Fe–Mn alloys”. English. In: *Materials Science & Engineering A* 325.1-2 (2002), pp. 307–319. DOI: 10.1016/S0921-5093(01)01459-9.

[31] V. D. F. C. Lins, M. A. Freitas, and E. M. D. P. Silva. “Oxidation kinetics of an Fe-31.8Mn-6.09Al-1.60Si-0.40C alloy at temperatures from 600 to 900 °C”. In: *Corrosion Science* 46 (2004).

[32] P. Mayer and W. W. Smeltzer. “Kinetics of Manganeseo-Wustite Scale Formation on Iron-Manganese Alloys”. In: *Journal of The Electrochemical Society* 119.5 (1972), pp. 626–631.

[33] NMC Media. “Hot and Cold Rolled Steel”. In: 6 (Sept. 2018), p. 2020. URL: http://www.nationalmaterial.com/hot-and-cold-rolled-steel/.

[34] W. M. Melfo and R. J. Dippenaar. “In situ observations of early oxide formation in steel under hot-rolling conditions”. In: *Journal of Microscopy* 225 (2007), pp. 147–155. URL: https://doi-org.tudelft.idm.oclc.org/10.1111/j.1365-2818.2007.01726.x.

[35] *Partial Pressure Measurement in Vacuum Technology*. URL: http://www.uhv.es/sites/marte/includes/doc/vzba01e1.pdf.

[36] P. Pedeferri. *Corrosion Science and Engineering. Chapter 26: High Temperature Corrosion*. 2018, pp. 589–610. DOI: https://doi-org.tudelft.idm.oclc.org/10.1007/978-3-319-97625-9_26.

[37] F. Pettit, R. Yinger, and J. B. Wagner. “The mechanism of oxidation of iron in carbon monoxide-carbon dioxide mixtures”. In: *Acta Metallurgica* 8 (1960), pp. 617–623. URL: https://doi.org/10.1016/0001-6160(60)90016-X.

[38] F. S. Pettit and J. B. Wagner. “Transition from the Linear to the Parabolic Rate Law during the Oxidation of Iron to Wustite in $CO - CO_2$ Mixtures”. In: *Acta Metallurgica 12* (1964), pp. 35–40.

[39] N. B. Pilling and R. E. Bedworth. “The oxidation of metals at high temperatures”. In: *JOURNAL OF THE INSTITUTE OF METALS* 29 (1923), pp. 529–582.

[40] David R. Poirier and G. Geiger. *Transport Phenomena in Materials Processing. Chapter 12: Fick’s Law and Diffusivity of Materials*. 2016, pp. 419–461. DOI: https://doi.org/10.1007/978-3-319-48090-9.

[41] David R. Poirier and G. Geiger. *Transport Phenomena in Materials Processing. Chapter 1: Viscous Properties of Fluids*. 2016, pp. 7–15. DOI: https://doi.org/10.1007/978-3-319-48090-9.

[42] RRUFF. *Hematite R110013*. 2021. URL: https://rruff.info/repository/sample_child_record_powder/by_minerals/Hematite__R110013-9__Powder__DIF_File__10622.txt.

[43] S. Samal and S. Mitra. “Influence of Grain Shape, Size, and Grain Boundary Diffusion on High-Temperature Oxidation of Pure Metal Fe, Cu, and Zn”. In: *Metallurgical and Materials Transactions A* 46 (2015).

[44] Hans-Joachim Selenz and Franz Oeters. “A contribution to the scaling of steel in technical flue gases”. In: *Archiv für das Eisenhüttenwesen* 55 (5 1984), pp. 201–208. DOI: https://doi-org.tudelft.idm.oclc.org/10.1002/srin.198405437.

[45] C. Wagner. “The distribution of cations in metal oxide and metal sulphide solid solutions formed during the oxidation of alloys”. In: *Corrosion Science* 2.9 (1969), pp. 91–109.

[46] J. B. Wagner and J. F. S. Pettit. “Transition from the linear to the parabolic rate law during the oxidation of iron to wustite in $CO - CO_2$ mixtures”. In: *Acta Metallurgica* 12 (1963).

[47] D. J. Young. “Chapter 1: The Nature of High Temperature Oxidation”. In: *High Temperature Oxidation and Corrosion of Metals, Sydney, Science*. 2016, pp. 1–30.

[48] D. J. Young. “Chapter 2: Enabling Theory”. In: *High Temperature Oxidation and Corrosion of Metals, Sydney, Science*. 2016, pp. 31–84.

[49] W. Y. D. Yuen and R. Y. Chen. “Review of the High-Temperature Oxidation of Iron and Carbon Steels in Air or Oxygen”. In: *Oxidation of Metals* 59 (2003).

[50] W. Y. D. Yuen and R. Y. Chen. “Short-time Oxidation Behavior of Low-carbon, Low-silicon Steel in Air at 850-1,180 degrees C, part I: Oxidation Kinetics”. In: *Oxidation of Metals* (2008), pp. 39–68.